HIGHER-ORDER MULTIPOLE AMPLITUDES IN RADIATIVE TRANSITIONS OF CHARMONIA

A Dissertation

Presented to the Faculty of the Graduate School

of Cornell University

in Partial Fulfillment of the Requirements for the Degree of

Doctor of Philosophy

by

James Robert Ledoux

February 2010

HIGHER-ORDER MULTIPOLE AMPLITUDES IN RADIATIVE TRANSITIONS OF CHARMONIA

James Robert Ledoux, Ph.D.

Cornell University 2010

Using 24 million ψ' decays in CLEO-c, we have searched for higher multipole admixtures in electric-dipole-dominated radiative transitions in charmonia. Let b_2 and a_2 denote the normalized magnetic quadrupole (M2) amplitudes in the transitions $\psi' \to \gamma\chi_{(c1,c2)}$ and $\chi_{(c1,c2)} \to \gamma J/\psi$, respectively. Previous measurements found ratios $a_2^{J=1}/a_2^{J=2}$ and $a_2^{J=1}/b_2^{J=1}$ in significant disagreement with theoretical predictions, where the J in the superscript refers to the angular momentum of the χ_{cJ}. By performing unbinned maximum likelihood fits to the full five-parameter angular distributions, we found the following values of M2 admixtures for $J_\chi = 1$:

$$\begin{aligned} a_2^{J=1} &= (-6.26 \pm 0.63 \pm 0.24) \times 10^{-2} \text{ and} \\ b_2^{J=1} &= (2.76 \pm 0.73 \pm 0.23) \times 10^{-2} \ , \end{aligned}$$

which agree well with theoretical expectations for a vanishing anomalous magnetic moment of the charm quark. For $J_\chi = 2$, if we fix the electric octupole (E3) amplitudes to zero as theory predicts for transitions between S and P states of charmonium, we find:

$$\begin{aligned} a_2^{J=2} &= (-9.3 \pm 1.6 \pm 0.3) \times 10^{-2} \ , \text{and} \\ b_2^{J=2} &= (1.0 \pm 1.3 \pm 0.3) \times 10^{-2} \ . \end{aligned}$$

If we allow for E3 amplitudes we find, with a four-parameter fit,

$$
\begin{aligned}
a_2^{J=2} &= (-7.9 \pm 1.9 \pm 0.3) \times 10^{-2} \ , \\
b_2^{J=2} &= (0.2 \pm 1.4 \pm 0.4) \times 10^{-2} \ , \\
a_3^{J=2} &= (1.7 \pm 1.4 \pm 0.3) \times 10^{-2} \ , \text{and} \\
b_3^{J=2} &= (-0.8 \pm 1.2 \pm 0.2) \times 10^{-2} \ .
\end{aligned}
$$

BIOGRAPHICAL SKETCH

James Robert Ledoux was born on Father's Day in 1981 with both parents living in a small town called Litchfield in southern New Hampshire. His parents had named their first born son "Michael" the most frequently used male name in America, and named their second and only other son "James" purportedly after Jimmy Carter, though it may have been due to James being the second most frequent American male name. James' middle name takes after his father, Robert, an engineer who died at age 43 of a myocardial infarction while the family was vacationing at Disney World. As a young child, Jim Bob was always interested in science and astronomy in particular and wanted to be an astronaut when he grew up, primarily as a result of his mother who was interested in pursuing a science career herself until sexist professors discouraged her in college. His choice of choosing a science major in college was highly influenced by his excellent public high school chemistry teacher.

In 1999, James graduated from Alvirne High School in Hudson, NH and enrolled in the University of New Hampshire (UNH). In 2003, James graduated with a B.S. in Physics with a 4.0 GPA, honors-in-major, with a minor in applied mathematics. While at UNH, James worked with the UNH Astrophysics Group starting in his sophomore year, until he left for Cornell in August 2003. At Cornell, James first worked in the chemistry department doing research to develop materials for better electrocatalysts for fuel cells, and then worked in the astronomy department doing observational infrared astronomy. Beginning in 2006, James began taking high energy physics courses, which resulted in James switching back to physics where he joined the CLEO collaboration in 2007 to do high energy experimental physics under his adviser, Prof. Richard Galik. After graduate school, James is switching into medical physics where he will do a postdoc at Weill Cornell with a cardiovascular MRI group.

This document is dedicated to Rich Galik,
whose kind patience, brilliance, attention to detail,
and guidance as a mentor made this research possible.

ACKNOWLEDGEMENTS

I would like to start by again thanking Rich Galik for continuing to keep me as a graduate student even after his rediagnosis of chordoma and for all his wonderful guidance.

I am grateful for my special committee and my CLEO paper committee for their extra support due to unfortunate circumstances surrounding my advisor's health. Specifically, Jon Rosner and David Cassel went above and beyond to ensure that everything went smoothly with the paper and thesis writing process. They repeatedly gave invaluable detailed comments on both the paper drafts and thesis drafts in an extremely prompt fashion. I would also like to thank Hajime Muramatsu, the charmonium PTA chair, for detailed comments on my analysis through the entire process. Additionally, Brian Heltsley was particularly helpful in quickly resolving an issue involving the crystal calorimeter efficiency near the transition regions among other contributions. Richard Ehrlich and Jim Napolitano also provided detailed comments on my analysis.

I also need to thank the entire CLEO collaboration that designed an excellent precision detector and analysis tools that made analysis of this type possible. CESR's hard work in providing excellent luminosity for the collisions that CLEO could study must also be acknowledged. My many graduate student colleagues made working more enjoyable, Steve Stroiney, Laura Fields, Peter Onyisi, and in particular my former office-mates Jim Hunt and Richard Gray. I'd like to thank Jim primarily for helping convince me to avoid using ROOT and instead switch to a fully pythonic analysis routine, in addition to many fruitful conversations about our respective analyses. I'd like to thank Richard Gray for helping spark my interest in medical physics (after seeing him go through the job search process). I very likely would not have chosen to take a medical physics course here, if it wasn't for

him and that led directly to my post-doctoral position in medical physics (with the professor of the said course). I would also like to thank Istvan, Laura, Werner, Eric, Peter, and Steve for their participation in CLEO 101, initiating me to the various CLEO analysis techniques.

Funding for this work came from directly from a National Science Foundation grant to the Laboratory of Elementary Particle Physics, and from the Cornell physics department while I was a teaching assistant.

I would also like to thank my mother, step-father, brother, and many friends for their continued encouragement and support.

TABLE OF CONTENTS

LIST OF TABLES

LIST OF FIGURES

CHAPTER 1

INTRODUCTION

1.1 Quarks and Quarkonia

The quark is a type of elementary particle that is classified into six flavors: down (d), up (u), strange (s), charm (c), bottom (b), and top (t) depending on the mass and charge of the quark. There are three generations of quarks, with each generation possessing one up-type quark (u, c, t) with a charge of $+2/3$ (in units of the charge of a proton) and one down-type quark (d, s, b) with a charge of $-1/3$. Each quark (q) has an anti-quark (denoted $\bar{q}$) with the same mass and spin, but with opposite-signed charge, parity, and flavor quantum numbers.

Hadrons are composite particles comprised of quarks bound together by the strong force. The properties of a hadron are determined by the quantum numbers of its valence quarks, even though the hadron exists in a quark sea. The hadrons are broken into two families, baryons and mesons, depending on the number and type of valence quarks. A baryon consists of three valence quarks (or three antiquarks for an antibaryon) bound together; protons (uud) and neutrons (udd) are the most common examples of baryons. A meson is comprised of a quark and an anti-quark bound together; pions (π) and etas (η) are typical examples of mesons.

Quarkonium is a specific type of flavorless meson that consists of a heavy-flavored quark and its anti-quark. Charmonia and bottomonia are two types of quarkonia formed by charm (c) and bottom (b) quarks, respectively. Due to the top quark's large mass, the top quark (t) quickly decays via electroweak interactions before a bound state of toponium can be formed. While the lighter quarks (u,

d, s) can form flavorless mesons as well, they are not typically called quarkonia. The lighter quarks have very similar masses and as such can undergo mixing, so the pure flavor eigenstates ($u\bar{u}$, $d\bar{d}$, and $s\bar{s}$) do not exist. Instead, the particles we observe are quantum mechanical mixtures of the states, *e.g.*, the neutral pion π^0 has the quark content $u\bar{u} - d\bar{d}$ and the η' has quark content $u\bar{u} + d\bar{d} + s\bar{s}$.

Quarkonium, which is bound by the strong force and consists of a quark and its anti-particle, is analogous to positronium, a bound state consisting of an electron and a positron (the anti-particle of an electron). Positronium which is bound together by electromagnetism has been extensively studied. Since positronium is analogous to a hydrogen atom with the proton nucleus replaced by a positron, it provides many tests of our models of atomic theory.

1.2 Multipole Radiation

The electromagnetic radiation that is released between transitions of different states is commonly studied in atomic and nuclear physics. This electromagnetic radiation takes the form of photons (the quanta of light), and is frequently analyzed in terms of its multipole radiation pattern. The electromagnetic radiation pattern can be broken into a sum of multipole contributions, though typically one or two multipoles will dominate the pattern. An electric (magnetic) multipole radiation pattern arises when an oscillating charge (current) distribution is broken down into its multipole moments. A multipole of order J_γ radiates J_γ units of angular momentum and is called a 2^{J_γ}-pole (*e.g.*, $J_\gamma = 1$ is dipole, $J_\gamma = 2$ is called quadrupole, $J_\gamma = 3$ is called octupole). The angular distribution of the multipole radiation is related to the square of the spherical harmonics of the same order [17].

1.3 Multipole Radiation in Charmonia

The radiative transitions of charmonia through the spin-triplet χ_{cJ} state are known to be dominated by electric dipole (E1) transitions, though higher-order multipole transitions, magnetic dipole (M2) and electric octupole (E3) are allowed to also occur for some of these transitions. These higher-order multipole transitions give information about the magnetic moment of the charm quark. To search for these transitions, we studied the two radiative decay sequences:

$$\begin{aligned} e^+e^- &\to \gamma^* \to \psi' \\ \psi' &\to \gamma' \chi_{(c1,c2)} \\ \chi_{(c1,c2)} &\to \gamma J/\psi \\ J/\psi &\to e^+e^- \text{ or } \mu^+\mu^- \end{aligned}$$

using the helicity formalism developed by Karl, Meshkov, Rosner, Brown and Cahn [19, 20, 34, 11]. As shown in the energy level diagram (Figure 1.1), the particles ψ', $\chi_{(c1,c2)}$, and J/ψ are respectively the $2\,^3S_1$, $1\,^3P_{(1,2)}$, and $1\,^3S_1$ charmonia states in the term symbol notation $n\,^{2S+1}L_J$. For the $J_\chi = 1$ decay sequence (where J_χ refers to the total angular momentum of the χ_{cJ} state), we search for two multipole amplitudes, $b_2^{J=1}$ and $a_2^{J=1}$, which are respectively the M2 amplitudes for the $\psi' \to \gamma'\chi_{c1}$ (b for $b$efore the χ_c) and $\chi_{c1} \to \gamma J/\psi$ decay (a for $a$fter the χ_c). Similarly, for the $J_\chi = 2$ decay sequence, we search for two M2 amplitudes ($b_2^{J=2}$, $a_2^{J=2}$) and two E3 amplitudes ($b_3^{J=2}$, $a_3^{J=2}$), where again b amplitudes refer to $\psi' \to \gamma'\chi_{c2}$ multipole amplitudes and a amplitudes refer to $\chi_{c2} \to \gamma J/\psi$. To distinguish between the two photons that have different energies, we denote the photon that decayed from the ψ' with a prime (γ').

The multipole amplitudes are calculated from a maximum likelihood fit of the

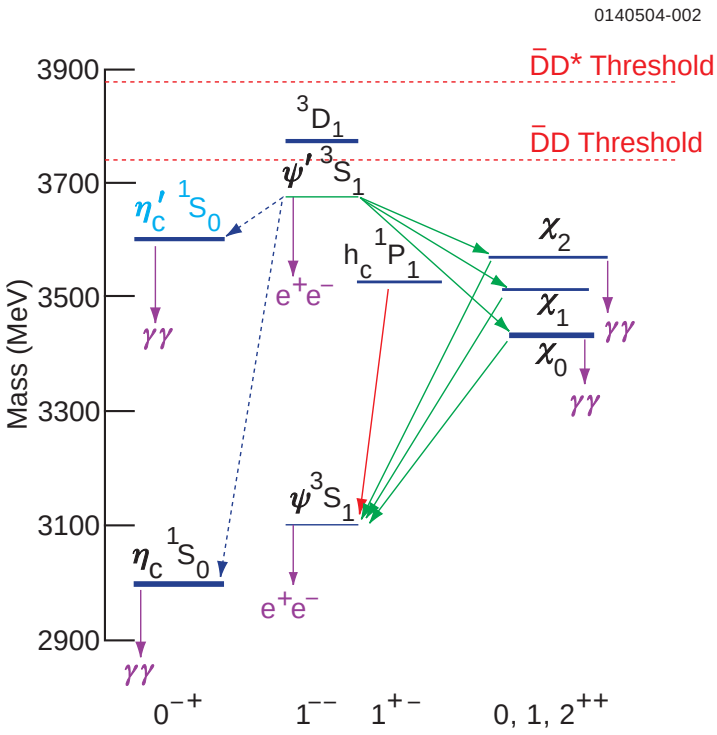

Figure 1.1: Energy level diagram for charmonia.

joint angular distribution of the two photons γ' and γ, which are described by a set of five angles for each event. The angles measure the directions of the photons relative to the directions of the e^+e^- forming the ψ' (in the ψ' frame), to the direction between the two photons (in the χ_c frame), and to the direction of the photons relative to the two leptons[1] $\ell^+\ell^-$ that decay from the J/ψ (in the J/ψ frame).

Previous experimental studies looking at $\chi_{cJ} \to \gamma J/\psi$ found the magnetic quadrupole amplitude via χ_{c1} decay sequences to be consistent with zero, while the magnetic quadrupole amplitude found via χ_{c2} decay sequences was found to be

[1]By leptons, we are referring to a decay into two muons $\mu^+\mu^-$, or two electrons e^+e^-. The lepton family of particles also includes one more charged lepton, the tauon, except that two tauons are more massive than the J/ψ which prevents the J/ψ from decaying into two tauons. There are also neutral (charge-zero) leptons called neutrinos; however, neutrinos are not used in this analysis.

several standard deviations from zero. This clashes with theoretical predictions, which predict that the ratio of the magnetic quadrupole amplitudes should be of order unity.

CHAPTER 2

THEORETICAL BACKDROP

2.1 Allowed Radiative Transitions

Radiative transitions among quarkonia are often classified into their electric (EJ_γ) and magnetic (MJ_γ) multipole amplitudes, where J_γ is the amount of angular momentum carried off by the emitted photon.

When more than one multipole transition is allowed, the multipole transition of lowest order J_γ tends to be the most probable transition. For a generic radiative transition $X_i \to \gamma X_f$ between two states X_i and X_f with angular momentum and parity of $|J_i, P_i\rangle$ and $|J_f, P_f\rangle$ respectively, the allowed values of J_γ are

$$|J_f - J_i| \;\leq\; J_\gamma \;\leq\; J_f + J_i \tag{2.1}$$

from quantum mechanical addition of angular momenta. Since the photon is a spin-one particle, there is an additional constraint for these transitions that $J_\gamma \geq 1$. Parity must be conserved in electromagnetic transitions; for an electric multipole transition of order J_γ, the parity between particle X_i and X_f is $P(\mathrm{E}J_\gamma) = P_i P_f = (-1)^{J_\gamma}$, and for a magnetic multipole transition of order J_γ, the parity between X_i and X_f is $P(\mathrm{M}J_\gamma) = P_i P_f = (-1)^{J_\gamma+1}$. Therefore, for radiative transitions between particles of opposite parity (*e.g.*, our signal decays $\psi' \to \gamma'\chi_{cJ}$ and $\chi_{cJ} \to \gamma J/\psi$ both have $P_i P_f = -1$) only $\mathrm{E}J_\gamma^{\mathrm{odd}}$ and $\mathrm{M}J_\gamma^{\mathrm{even}}$ transitions can occur. Using Eq. (2.1), we find that the allowed radiative transitions between the ψ states (the S states ψ' and J/ψ) and a χ_{c2} are $J_\gamma \in (1, 2, 3)$ corresponding to E1 (electric dipole), M2 (magnetic quadrupole), and E3 (electric octupole). Similarly, for transitions between a ψ state and a χ_{c1} only E1 and M2 transitions are allowed, and for

transitions between a ψ state and a χ_{c0} only E1 transitions are allowed.

2.2 Single Quark Radiation Hypothesis

The single quark radiation (SQR) hypothesis posits that in radiative transitions of hadrons, only one of the quarks in the hadron participates in the radiative transition while the other quark(s) act as a spectator(s) [27]. Looking at parity-changing transitions between mesons of charmonia of the type $\psi' \to \gamma'\chi_{c2}$ and $\chi_{c2} \to \gamma J/\psi$ in this framework, we must assign all of the orbital angular momentum $L = 1$ of the χ_{c2} to the "active" quark. The "spectator" quark is left with only the angular momentum due to its intrinsic spin, so its total angular momentum is $J^{\rm sp} = S_q = 1/2$. The spectator quark does not change in the radiative transitions, so we do not need to assign a subscript associating it with the ψ or χ state.

The active quark in the χ_{c2} has angular momentum $J^{\rm ac}_\chi = 3/2$, since $J^{\rm ac}_\chi = S_q \oplus L_\chi = 1/2 \oplus 1$ allows both $J^{\rm ac}_\chi \in (1/2, 3/2)$ while $J_\chi = 2 = J^{\rm ac}_\chi + J^{\rm sp}_\chi$ constrains the active quark to have $J^{\rm ac}_\chi = 3/2$. To summarize, the "active" quark must have $J^{\rm ac}_\chi = 3/2$ in the χ_{c2} and $J^{\rm ac}_\psi = 1/2$ in the ψ state (ψ' or J/ψ) and the "spectator" quark must have $J^{\rm sp} = 1/2$ in both the χ_{c2} and ψ states. Despite the meson transition being a transition between a $J = 1$ and $J = 2$ state (where E3 transitions are allowed), under the SQR hypothesis E3 transitions are forbidden as it is now a parity-changing transition between a $J = 3/2$ quark and a $J = 1/2$ quark, where only E1 and M2 transitions are allowed.

A more general argument can be made by noting that the parity-changing transitions between an S ($L = 0$) and P ($L = 1$) state will have $|\Delta L| = 1$ and that under the single quark radiation hypothesis $|\Delta S| \leq 1$ (as a quark is a spin

1/2 particle). Therefore, we can have radiative transition of $|J_\gamma| \leq 2$, preventing electric octupole transitions.

The SQR hypothesis forbids transitions between an S and a P state from having a non-zero electric octupole amplitude. However, if the S state has a small D ($L = 2$) component or the P state has a small F ($L = 3$) component, then under the SQR hypothesis E3 amplitudes are allowed from the D or F part of the admixture.[9] There is significant evidence that the ψ' state is actually the following admixture of the $2\,^3S_1$ and $1\,^3D_1$ states

$$|\psi'\rangle = \cos\varphi \left|2\,^3S_1\right\rangle - \sin\varphi \left|1\,^3D_1\right\rangle .$$

where the mixing coefficient $\varphi = (12 \pm 2)^\circ$ is known from the leptonic widths of the ψ' and ψ'', coupled-channel estimates, and the ratio of the partial widths to $\pi\pi J/\psi$ [32, 33]. Since the ψ' state has a $\sin^2\varphi \approx 4\%$ admixture of the $1D$ state, a small E3 octupole amplitude, $b_3^{J=2}$,is allowed in the transition $\psi' \to \gamma'\chi_{c2}$. However, as there is no evidence for either $P-F$ mixing of the χ_{c2} state or of S-D mixing with the J/ψ state, the E3 amplitude for $\chi_{c2} \to \gamma J/\psi$, $a_3^{J=2}$ should be zero.

2.3 Joint Angular Distribution

The formalism of Karl, Meshkov and Rosner developed in [19, 20] is used to construct the joint angular distribution of the decay sequence. The decay sequences

$$\psi'(\lambda') \to \gamma'(\mu') + \chi(\nu')$$
$$\chi(\nu) \to \gamma(\mu) + J/\psi(\lambda)$$

have the helicities assigned in parentheses, with the notation that the helicities associated with the ψ' decay are primed. Helicity is simply the projection of the

spin of a particle onto its direction of its momentum. To differentiate between the two photons in the two decay sequences, we also assign a prime to the photon that is from the ψ' decay. From conservation of angular momentum, the helicities are related by

$$\lambda' = \mu' - \nu' \tag{2.2}$$

$$\nu = \mu - \lambda \tag{2.3}$$

and we label the helicity amplitudes for the two decays $B_{\nu'\mu'}$ (B for Before the χ_c) and $A_{\nu\mu}$ (A for After the χ_c) for the two decay sequences. Applying the parity operator to the decay $\psi' \to \gamma'\chi_{cJ}$ described by the helicity amplitude $B_{\nu'\mu'}$ (and similarly with $\chi_{cJ} \to \gamma J/\psi$ described by $A_{\nu\mu}$), we can relate the helicity amplitudes [31, Eq. 6.12]:

$$\begin{aligned} B_{\nu',\mu'} &= P_{\psi'} P_\chi P_\gamma (-1)^{J_\chi + J_\gamma - J_{\psi'}} B_{-\nu',-\mu'} \\ &= (-1)^{J_\chi} B_{-\nu',-\mu'} \\ A_{\nu,\mu} &= (-1)^{J_\chi} A_{-\nu,-\mu} \end{aligned}$$

Therefore, defining

$$\begin{aligned} B_\nu \equiv B_{\nu,1} &= (-1)^{J_\chi} B_{-\nu,-1} \\ A_\nu \equiv A_{\nu,1} &= (-1)^{J_\chi} A_{-\nu,-1} \end{aligned}$$

we find that for $J_\chi = 1$ ($J_\chi = 2$) the decay $\psi' \to \gamma'\chi_{cJ}$ is described by two (three) independent helicity amplitudes B_1, B_0 (B_2, B_1, B_0) and similarly the decay $\chi_c \to \gamma J/\psi$ is described by A_1, A_0 (A_2, A_1, A_0) [1].

To form the joint angular distribution the ψ' and J/ψ density matrices must be constructed from the directions of the two electrons forming the ψ' and the

[1] By our conventions, the indices on the helicity amplitudes B_ν and A_ν only go for $\nu \geq 0$ due to conservation of angular momentum. For example, $A_{-1} \equiv A_{-1,1}$ has $\nu = -1$ and $\mu = 1$, so from Eqs. (2.2-2.3) the helicity of the J/ψ should be $\lambda = \mu - \nu = 2$ which isn't allowed (allowed helicities for the J/ψ are $\lambda \in \{1, 0, -1\}$).

two leptons that decay from the J/ψ. For the reaction $e^+e^- \to \gamma^* \to \psi'$, the polarization of the ψ' along the beam axis is ± 1, since the electrons are at high energies relative to their mass so the positron and electron can only couple if they have opposite helicities. Therefore, the density matrix giving the polarizations in the direction of the beam axis (the z-axis) is given by $\rho^{(\lambda'\tilde{\lambda}')} = \epsilon_1^{*(\lambda')}\epsilon_1^{(\tilde{\lambda}')} + \epsilon_2^{*(\lambda')}\epsilon_2^{(\tilde{\lambda}')}$ representing an incoherent sum of both ψ' polarizations, where $\epsilon^{(\lambda)}$ is the polarization vector (with helicity λ) defined with components $\epsilon^{(1)} = 1/\sqrt{2}(-1, -i, 0)$, $\epsilon^{(0)} = (0, 0, 1)$ and $\epsilon^{(-1)} = -\epsilon^{(1)*} = 1/\sqrt{2}(1, -i, 0)$. Generalizing to an arbitrary direction $\hat{n}$ we find the the density matrix ρ for ψ' is:

$$\rho^{(\lambda',\tilde{\lambda}')}(\theta', \phi') = \sum_{i,j} \epsilon_i^{*(\lambda')}\epsilon_j^{(\tilde{\lambda}')} L^{ij}(\theta', \phi') \tag{2.4}$$

$$L^{ij}(\theta', \phi') \equiv \delta^{ij} - n^i n^j$$

$$\hat{n} \equiv (\sin\theta'\cos\phi', \sin\theta'\sin\phi', \cos\theta').$$

Similarly for the J/ψ, the density matrix is constructed as:

$$\rho^{(\lambda,\tilde{\lambda})}(\theta, \phi) = \sum_{i,j} \epsilon_i^{*(\lambda)}\epsilon_j^{(\tilde{\lambda})} L^{ij}(\theta, \phi) \tag{2.5}$$

$$L^{ij}(\theta, \phi) \equiv \delta^{ij} - m^i m^j$$

$$\hat{m} \equiv (\sin\theta\cos\phi, \sin\theta\sin\phi, \cos\theta).$$

The J/ψ density matrix is therefore:

$$\begin{pmatrix} \rho^{(1,1)} & \rho^{(1,0)} & \rho^{(1,-1)} \\ \rho^{(0,1)} & \rho^{(0,0)} & \rho^{(0,-1)} \\ \rho^{(-1,1)} & \rho^{(-1,0)} & \rho^{(-1,-1)} \end{pmatrix} = \begin{pmatrix} \frac{1+\cos^2\theta}{2} & \frac{\sin\theta\cos\theta}{\sqrt{2}}e^{-i\phi} & \frac{\sin^2\theta}{2}e^{-2i\phi} \\ \frac{\sin\theta\cos\theta}{\sqrt{2}}e^{i\phi} & \sin^2\theta & -\frac{\sin\theta\cos\theta}{\sqrt{2}}e^{-i\phi} \\ \frac{\sin^2\theta}{2}e^{2i\phi} & -\frac{\sin\theta\cos\theta}{\sqrt{2}}e^{i\phi} & \frac{1+\cos^2\theta}{2} \end{pmatrix}$$

while the ψ' density matrix is identical after substituting θ' and ϕ' for θ and ϕ.

The angles θ', ϕ' contain information on the polarization of the ψ' as these are respectively the polar and azimuthal angle of the incident e^+ direction measured

relative to the γ' (defining the z-axis) and γ directions (lying in the x-z plane with *positive* x-component) in the ψ' reference frame. Similarly, the angles θ, ϕ contain information on the polarization of the J/ψ as these are the polar and azimuthal angles of the positive decay lepton (ℓ^+) measured relative to the γ (defining the z-axis) and γ' (lying in the x-z plane with a *negative* x-component) directions in the J/ψ reference frame. The angle $\theta_{\gamma\gamma'}$ defined by the angle between the two photons in the χ_c rest frame is also used to give information on the necessary rotation between the two reference frames. The reference frames for construction of these five angles are shown in Figure 2.1.

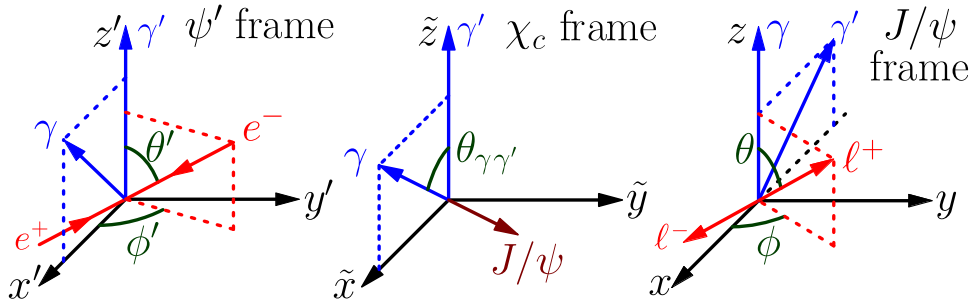

Figure 2.1: Definition of the five angles in the appropriate reference frames as used in the helicity formalism of this analysis. In the ψ' frame, the angles θ', ϕ' are respectively the polar and azimuthal angles of the beam pipe (specifically the positron's direction) relative to γ' defining the z-axis, and γ lying in the x-z plane (with a *positive* x-component). In the χ_c frame, the angle $\theta_{\gamma\gamma'}$ is the angle between the two photons. In the J/ψ frame, the angles θ, ϕ are respectively the polar and azimuthal angles of the two leptons (specifically the positive lepton's direction) relative to γ defining the z-axis, and γ' lying in the x-z plane (with a *negative* x-component).

The joint angular distribution is therefore

$$
\begin{aligned}
&W(\cos\theta', \phi', \cos\theta_{\gamma\gamma'}, \cos\theta, \phi) \propto \\
&\quad \sum \ \rho^{(\mu'-\nu', \mu'-\tilde{\nu}')}(\theta', \phi') B_{|\nu'|} B_{|\tilde{\nu}'|} d^{J_\chi}_{-\nu'\nu}(\theta_{\gamma\gamma'}) d^{J_\chi}_{-\tilde{\nu}'\tilde{\nu}}(\theta_{\gamma\gamma'}) A_{|\nu|} A_{|\tilde{\nu}|} \rho^{*(\nu-\mu, \tilde{\nu}-\mu)}(\theta, \phi) \\
&\nu'\tilde{\nu}'; \mu' = \pm 1 \\
&\nu\tilde{\nu}; \mu = \pm 1
\end{aligned}
\tag{2.6}
$$

where $d^{J_\chi}_{\nu'\nu}$ are the standard Wigner d-functions [3],

$$
\left[d^1_{\nu'\nu}\right] \equiv \begin{pmatrix} d^{J=1}_{1,1} & d^{J=1}_{0,1} & d^{J=1}_{-1,1} \\ d^{J=1}_{1,0} & d^{J=1}_{0,0} & d^{J=1}_{-1,0} \\ d^{J=1}_{1,-1} & d^{J=1}_{0,-1} & d^{J=1}_{-1,-1} \end{pmatrix} = \begin{pmatrix} \frac{1+\cos\theta}{2} & \frac{\sin\theta}{\sqrt{2}} & \frac{1-\cos\theta}{2} \\ -\frac{\sin\theta}{\sqrt{2}} & \cos\theta & \frac{\sin\theta}{\sqrt{2}} \\ \frac{1-\cos\theta}{2} & -\frac{\sin\theta}{\sqrt{2}} & \frac{1+\cos\theta}{2} \end{pmatrix},
$$

$$
\begin{aligned}
\left[d^2_{\nu'\nu}\right] &\equiv \begin{pmatrix} d^{J=2}_{2,2} & d^{J=2}_{1,2} & d^{J=2}_{0,2} & d^{J=2}_{-1,2} & d^{J=2}_{-2,2} \\ d^{J=2}_{2,1} & d^{J=2}_{1,1} & d^{J=2}_{0,1} & d^{J=2}_{-1,1} & d^{J=2}_{-2,1} \\ d^{J=2}_{2,0} & d^{J=2}_{1,0} & d^{J=2}_{0,0} & d^{J=2}_{-1,0} & d^{J=2}_{-2,0} \\ d^{J=2}_{2,-1} & d^{J=2}_{1,-1} & d^{J=2}_{0,-1} & d^{J=2}_{-1,-1} & d^{J=2}_{-2,-1} \\ d^{J=2}_{2,-2} & d^{J=2}_{1,-2} & d^{J=2}_{0,-2} & d^{J=2}_{-1,-2} & d^{J=2}_{-2,-2} \end{pmatrix} \\
&= \begin{pmatrix} \left(\frac{1+\cos\theta}{2}\right)^2 & -d^{J=2}_{2,1} & d^{J=2}_{2,0} & -d^{J=2}_{2,-1} & d^{J=2}_{2,-2} \\ -\frac{\sin\theta(1+\cos\theta)}{2} & \frac{(1+\cos\theta)(2\cos\theta-1)}{2} & -d^{J=2}_{1,0} & d^{J=2}_{1,-1} & -d^{J=2}_{2,-1} \\ \frac{\sqrt{6}}{4}\sin^2\theta & -\frac{\sqrt{6}}{2}\sin\theta\cos\theta & \frac{3\cos^2\theta-1}{2} & -d^{J=2}_{1,0} & d^{J=2}_{2,0} \\ -\frac{\sin\theta(1-\cos\theta)}{2} & \frac{(1-\cos\theta)(2\cos\theta+1)}{2} & d^{J=2}_{1,0} & d^{J=2}_{1,1} & -d^{J=2}_{2,1} \\ \left(\frac{1-\cos\theta}{2}\right)^2 & d^{J=2}_{2,-1} & d^{J=2}_{2,0} & d^{J=2}_{2,1} & d^{J=2}_{2,2} \end{pmatrix},
\end{aligned}
$$

ρ and ρ^* are the density matrices defined by Eqs. (2.4) and (2.5), A_ν, B_ν are the helicity amplitudes in the fit, and the angles $\theta', \phi', \theta_{\gamma\gamma'}, \theta, \phi$ are defined in Figure 2.1.

The helicity amplitudes A_ν, B_ν are related to the multipole amplitudes a_{J_γ}, b_{J_γ}

by the Clebsch-Gordan coefficients (in the form $\langle j_1, m_1; j_2, m_2 | J, M \rangle$):

$$A^{J_\chi}_{|\nu|} = \sum_{J_\gamma} \sqrt{\frac{2J_\gamma + 1}{2J_\chi + 1}} a^{J_\chi}_{J_\gamma} \langle J_\gamma, 1; 1, |\nu| - 1 | J_\chi, |\nu| \rangle \tag{2.7}$$

which lead to the following relationships for the $J_\chi = 1$ and $J_\chi = 2$ cases respectively:

$$\begin{pmatrix} A^{J=1}_0 \\ A^{J=1}_1 \end{pmatrix} = \begin{pmatrix} \sqrt{\frac{1}{2}} & \sqrt{\frac{1}{2}} \\ \sqrt{\frac{1}{2}} & -\sqrt{\frac{1}{2}} \end{pmatrix} \begin{pmatrix} a^{J=1}_1 \\ a^{J=1}_2 \end{pmatrix} \tag{2.8}$$

$$\begin{pmatrix} A^{J=2}_0 \\ A^{J=2}_1 \\ A^{J=2}_2 \end{pmatrix} = \begin{pmatrix} \sqrt{\frac{1}{10}} & \sqrt{\frac{1}{2}} & \sqrt{\frac{2}{5}} \\ \sqrt{\frac{3}{10}} & \sqrt{\frac{1}{6}} & -\sqrt{\frac{8}{15}} \\ \sqrt{\frac{3}{5}} & -\sqrt{\frac{1}{3}} & \sqrt{\frac{1}{15}} \end{pmatrix} \begin{pmatrix} a^{J=2}_1 \\ a^{J=2}_2 \\ a^{J=2}_3 \end{pmatrix}. \tag{2.9}$$

The relationships between $B_{\nu'}$ and $b_{J_{\gamma'}}$ are identical; merely swap all A_ν and a_{J_γ} with $B_{\nu'}$ and $b_{J_{\gamma'}}$ in Eqs. (2.7-2.9). It is worth noting that these matrices relating the helicity amplitudes to the multipole amplitude are orthogonal, so the inverse is simply the transpose of the matrix.

2.4 Parity Transformations

The PDF given by Eq. (2.6) is symmetric under four distinct parity transformations that can be used to fold four of the five angles into the positive domain without altering the value of $W(\Omega; \mathbb{A})$. This technique was used in Refs. [28, 29] to improve the statistics of their binned likelihood fits. We use these transformations to improve the statistics when we compare binned histograms of projections of a pure E1 and fitted multipole distribution.

If in the decay $J/\psi \to \ell^+\ell^-$, the right hand side undergoes a parity operation,

the three vectors for the leptons will transform as

$$\mathbf{p}_{\ell^+} \rightarrow -\mathbf{p}_{\ell^+} \qquad (J/\psi \text{ frame})$$

$$\mathbf{p}_{\ell^-} \rightarrow -\mathbf{p}_{\ell^-} \qquad (J/\psi \text{ frame})$$

with the effect on the measured angles is

$$\begin{aligned} \cos\theta &\rightarrow -\cos\theta \\ \phi &\rightarrow \pi + \phi. \end{aligned} \tag{2.10}$$

Similarly, using parity conservation on $e^+e^- \rightarrow \psi' \rightarrow \gamma'\chi_c$ we find

$$\mathbf{p}_{e^+} \rightarrow -\mathbf{p}_{e^+} \qquad (\psi' \text{ frame})$$

$$\mathbf{p}_{e^-} \rightarrow -\mathbf{p}_{e^-} \qquad (\psi' \text{ frame})$$

leads to changing the angles

$$\begin{aligned} \cos\theta' &\rightarrow -\cos\theta' \\ \phi' &\rightarrow \pi + \phi'. \end{aligned} \tag{2.11}$$

Applying a parity operation to the left hand side of $\chi_c \rightarrow \gamma J/\psi$, we see the four-vectors change as

$$\mathbf{p}_{\gamma} \rightarrow -\mathbf{p}_{\gamma} \qquad (\chi_c \text{ frame})$$

$$\mathbf{p}_{\ell^+} \rightarrow -\mathbf{p}_{\ell^+} \qquad (J/\psi \text{ frame})$$

$$\mathbf{p}_{\ell^-} \rightarrow -\mathbf{p}_{\ell^-} \qquad (J/\psi \text{ frame})$$

with the following effects on our angles

$$\begin{aligned} \phi' &\rightarrow \pi + \phi' \\ \cos\theta_{\gamma\gamma'} &\rightarrow -\cos\theta_{\gamma\gamma'} \\ \phi &\rightarrow \pi - \phi. \end{aligned} \tag{2.12}$$

Finally applying a parity operation to the right hand side of $\psi' \to \gamma'\chi_c$, the four-vectors will change as

$$\begin{aligned}
\mathbf{p}_{\gamma'} &\to -\mathbf{p}_{\gamma'} \qquad (\psi' \text{ frame}) \\
\mathbf{p}_{\gamma} &\to -\mathbf{p}_{\gamma} \qquad (\chi_c \text{ frame}) \\
\mathbf{p}_{\ell^+} &\to -\mathbf{p}_{\ell^+} \qquad (J/\psi \text{ frame}) \\
\mathbf{p}_{\ell^-} &\to -\mathbf{p}_{\ell^-} \qquad (J/\psi \text{ frame})
\end{aligned}$$

causing the angles to change as

$$\begin{aligned}
\cos\theta' &\to -\cos\theta' \\
\phi' &\to \pi - \phi' \\
\phi &\to -\phi.
\end{aligned} \tag{2.13}$$

Note that the combined effect of performing the parity transformation of Eq. (2.11) followed by the transformation of Eq. (2.13) leads to the combined effect of

$$\begin{aligned}
\phi' &\to -\phi' \\
\phi &\to -\phi
\end{aligned} \tag{2.14}$$

In the fitting section, we perform this set of transformations to enhance the binned comparisons of data to Monte Carlo projections of phase space data selected with a given value of $\mathbb{A}$ via the rejection method. When we perform the transformations to fold the data into the positive domain, we first check if $\cos\theta < 0$ and apply Eq. (2.10) when it is. Next, we check if $\cos\theta' < 0$ and apply Eq. (2.11) when necessary, and similarly we apply Eq. (2.12) if $\cos\theta_{\gamma\gamma'} < 0$, and finally we apply Eq. (2.14) if $\phi_p < 0$ (after already applying all the previous parity transformations that were necessary). It is noteworthy that while for the angles $\cos\theta', \cos\theta_{\gamma\gamma'}, \cos\theta$ this set of transformations is equivalent to histogramming $|\cos\theta'|, |\cos\theta_{\gamma\gamma'}|, |\cos\theta|$, the

phase angles ϕ' and ϕ do not have a simple relationship to the original histogram. For example, the effect of these transformations for several different values of phase angles $\Omega \equiv (\cos\theta', \phi', \cos\theta_{\gamma\gamma'}, \cos\theta, \phi)$ is

$$\Omega_1 = (-1/3, \pi/3, 1/3, 1/3, \pi/3) \rightarrow \Omega_1' = (1/3, 2\pi/3, 1/3, 1/3, -\pi/3)$$

$$\Omega_2 = (1/3, -\pi/3, 1/3, 1/3, \pi/3) \rightarrow \Omega_2' = (1/3, \pi/3, 1/3, 1/3, -\pi/3)$$

$$\Omega_3 = (1/3, \pi/3, -1/3, 1/3, \pi/3) \rightarrow \Omega_3' = (1/3, 2\pi/3, 1/3, 1/3, 2\pi/3)$$

$$\Omega_4 = (1/3, \pi/3, 1/3, -1/3, \pi/3) \rightarrow \Omega_4' = (1/3, \pi/3, 1/3, 1/3, -2\pi/3)$$

$$\Omega_5 = (1/3, \pi/3, 1/3, 1/3, -\pi/3) \rightarrow \Omega_5' = (1/3, \pi/3, 1/3, 1/3, -\pi/3) \ .$$

2.5 Quark Magnetic Moments

The magnetic quadrupole amplitudes are related to the anomalous magnetic moment of the charm quark κ_c as

$$a_2^{J=1} \equiv \frac{M2}{\sqrt{E1^2 + M2^2}} = -\frac{E_\gamma}{4m_c}(1+\kappa_c) \approx -0.065(1+\kappa_c) \tag{2.15}$$

$$a_2^{J=2} \equiv \frac{M2}{\sqrt{E1^2 + M2^2 + E3^2}} = -\frac{3}{\sqrt{5}}\frac{E_\gamma}{4m_c}(1+\kappa_c) \approx -0.096(1+\kappa_c) \tag{2.16}$$

$$b_2^{J=1} \equiv \frac{M2}{\sqrt{E1^2 + M2^2}} = \frac{E_{\gamma'}}{4m_c}(1+\kappa_c) \approx 0.029(1+\kappa_c) \tag{2.17}$$

$$b_2^{J=2} \equiv \frac{M2}{\sqrt{E1^2 + M2^2 + E3^2}} = \frac{3}{\sqrt{5}}\frac{E_{\gamma'}}{4m_c}(1+\kappa_c) \approx 0.029(1+\kappa_c) \tag{2.18}$$

to first order in E_γ/m_c assuming that the ψ' and J/ψ are pure S states (no mixing with D states) and that the χ_c states are pure P states (no mixing with F states)[34, 35][2]. In the above equations, E1, M2, E3 refer to the amplitudes corresponding to the multipole transitions. Results incorporating S-D mixing going to to higher order in E_γ/m_c need to use a potential model for charmonium [35]. The

[2]Note the misprint in [35] for their equation (41) describing $a_2^{J=2}$ to first order. This misprint was previously noted in footnote 1 of [2].

numerical results in Eq. (2.15 - 2.18) were obtained using $m_c = 1.5\,\mathrm{GeV}$ and the following photon energies: $E_{\gamma'}^{J=1} = 171.255(77)\,\mathrm{MeV}$, $E_{\gamma}^{J=1} = 389.363(63)\,\mathrm{MeV}$, $E_{\gamma'} = 127.601(95)\,\mathrm{MeV}$, and $E_{\gamma} = 429.625(80)\,\mathrm{MeV}$ [3], and the numerical results from Eqs. (2.17) and (2.18) are identical to two significant digits since $E_{\gamma'}^{J=1}/E_{\gamma'}^{J=2} \approx 1.34 \approx 3/\sqrt{5}$.

These first-order relationships are derived from the non-relativistic interaction Hamiltonian for photon emission from a +2/3 charged quark:

$$\begin{aligned} H_I = \; & -\frac{e_c}{2m_c}(\mathbf{A}^* \cdot \mathbf{p} + \mathbf{p} \cdot \mathbf{A}^*) - \mu\sigma \cdot \mathbf{H}^* \\ & -\frac{1}{2m_c}\left(\mu - \frac{e_c}{4m_c}\right)(\sigma \cdot [\overrightarrow{E}^* \times \mathbf{p}] - \sigma \cdot [\mathbf{p} \times \mathbf{E}^*]) \end{aligned} \tag{2.19}$$

where $e_c = \frac{2}{3}|e|$ is the charge of the charm quark, $\mu = (e_c/2m_c)(1 + \kappa_c)$ is the magnetic moment of the charm quark, and $\mathbf{A}^*$, $\mathbf{E}^* \equiv -\partial\mathbf{A}^*/\partial t$, and $\mathbf{H}^* \equiv \nabla \times \mathbf{A}^*$ are respectively the vector potential, electric and magnetic field of the outgoing photon (all are complex conjugated as they are outgoing) [20]. The first term in Eq. (2.19) arises from the replacing $\mathbf{p}$ with the gauge covariant derivative $\mathbf{p} - e_c\mathbf{A}^*$ in the kinetic energy term of the Hamiltonian and contributes to the dominant E1 term. The second term results from the interaction of the spin with the magnetic field and is the only term in H_I that contributes to M2 to first order. The second and third terms together both arise from the Foldy-Wouthuysen reduction of the Dirac Hamiltonian and both contribute to a small correction term to E1 that is proportional to κ_c [20, 24].

The ratios of the predicted multipole amplitudes given by Eqs. (2.15-2.18) are

$$\left(\frac{a_2^{J=1}}{a_2^{J=2}}\right)_{\rm th} = \frac{E_\gamma^{J=1}}{E_\gamma^{J=2}}\frac{\sqrt{5}}{3} = 0.6755 \pm 0.0002 \tag{2.20}$$

$$\left(\frac{a_2^{J=1}}{b_2^{J=1}}\right)_{\rm th} = -\frac{E_\gamma^{J=1}}{E_{\gamma'}^{J=1}} = -2.274 \pm 0.001 \tag{2.21}$$

$$\left(\frac{b_2^{J=1}}{b_2^{J=2}}\right)_{\rm th} = \frac{E_{\gamma'}^{J=1}}{E_{\gamma'}^{J=2}}\frac{\sqrt{5}}{3} = 1.0004 \pm 0.0008 \tag{2.22}$$

$$\left(\frac{a_2^{J=2}}{b_2^{J=2}}\right)_{\rm th} = -\frac{E_\gamma^{J=2}}{E_{\gamma'}^{J=2}} = -3.367 \pm 0.003. \tag{2.23}$$

As these ratios are independent of both κ_c and m_c, they are more reliable predictions than predictions of multipole amplitudes. As the multipole amplitudes given in Eqs. (2.15-2.18) have corrections of order $(E_\gamma/m_c)^2$, if we assign a fractional uncertainty equal to $(E_\gamma/m_c)^2$ to the multipole amplitude[3] we find the ratios are:

$$\left(\frac{a_2^{J=1}}{a_2^{J=2}}\right)_{\rm th} = \frac{-0.0649 \pm 0.0043}{-0.0960 \pm 0.0078} = 0.676 \pm 0.071 \tag{2.24}$$

$$\left(\frac{a_2^{J=1}}{b_2^{J=1}}\right)_{\rm th} = \frac{-0.0649 \pm 0.0043}{0.0285 \pm 0.0004} = -2.27 \pm 0.16 \tag{2.25}$$

$$\left(\frac{b_2^{J=1}}{b_2^{J=2}}\right)_{\rm th} = \frac{0.0285 \pm 0.0004}{0.0285 \pm 0.0002} = 1.000 \pm 0.015 \tag{2.26}$$

$$\left(\frac{a_2^{J=2}}{b_2^{J=2}}\right)_{\rm th} = \frac{-0.0960 \pm 0.0078}{0.0285 \pm 0.0002} = -3.37 \pm 0.28\ . \tag{2.27}$$

2.6 Lattice QCD Predictions

Dudek *et al.* [14, 15] performed lattice QCD calculations for the charmonium radiative transitions $\chi_{(c1,c2)} \to \gamma J/\psi$. They ran lattice simulations at various values of Q^2 (the square of the four-vector of the photon, which is 0 for real photons) and extrapolated to $Q^2 \to 0$ by fitting the data points to the form $E_1(Q^2) = E_1(0)(1 + \lambda Q^2)e^{-Q^2/(16\beta^2)}$.

[3]We use $\kappa_c = 0$, $m_c = 1.5\,\mathrm{GeV}$ when assigning fractional uncertainty, though the ratio is ultimately independent of both variables.

For the transition $\chi_{c1} \to \gamma J/\psi$, they found when extrapolating the amplitudes for E1 and M2 to $Q^2 \to 0$ individually that

$$\frac{\mathrm{M2}(Q^2 \to 0)}{\mathrm{E1}(Q^2 \to 0)} = \frac{-0.020 \pm 0.017}{0.23 \pm 0.03} = -0.09 \pm 0.07 \; . \tag{2.28}$$

From their fit they also found $\beta_{\mathrm{E1}} = 440 \pm 40\,\mathrm{MeV}$, $\lambda_{\mathrm{E1}} = 0.71 \pm 0.30\,\mathrm{GeV}^{-2}$, $\beta_{\mathrm{M2}} = 450 \pm 50\,\mathrm{MeV}$, $\lambda_{\mathrm{M2}} = 5 \pm 6\,\mathrm{GeV}^{-2}$, which corresponds to a partial decay width of $\Gamma(\chi_{c1} \to J/\psi\gamma) = 270 \pm 70\,\mathrm{keV}$ similar to the PDG average of $\Gamma_{\mathrm{PDG}} = 320 \pm 25\,\mathrm{keV}$. They conclude that without data points at smaller Q^2 or certainty about the form factors for the Q^2 dependence they cannot make a particularly meaningful comparison to experimental values [15].

Similarly for the transition $\chi_{c2} \to \gamma J/\psi$, they find the multipole amplitudes as $Q^2 \to 0$:

$$\frac{\mathrm{M2}(0)}{\sqrt{\mathrm{E1}(0)^2 + \mathrm{M2}(0)^2 + \mathrm{E3}^2(0)}} = -0.39 \pm 0.07 \tag{2.29}$$

$$\frac{\mathrm{E3}(0)}{\sqrt{\mathrm{E1}(0)^2 + \mathrm{M2}(0)^2 + \mathrm{E3}^2(0)}} = 0.010 \pm 0.011 \tag{2.30}$$

though they only list the fit parameters for E1 where $\beta_{\mathrm{E1}} = 550 \pm 80\,\mathrm{MeV}$, $\lambda_{\mathrm{E1}} = -0.39 \pm 0.01\,\mathrm{GeV}^{-2}$. They note that while the a_2 ratio is considerably larger than the PDG average they do have the same sign [15].

2.7 Multipole Study in Bottomonia

With a dataset of a suitable size, it should be possible to perform this type of analysis to search for multipole amplitudes in radiative transitions of bottomonia,

by looking for the signal decay sequences:

$$\Upsilon(2S) \to \gamma' \chi_{(b1,b2)}$$
$$\chi_{(b1,b2)} \to \gamma \Upsilon(1S)$$
$$\Upsilon(1S) \to \ell^+ \ell^-$$

Following Eqs. (2.15-2.18), we replace the quark mass and photon energies to expect multipole amplitudes of the following size

$$\begin{aligned}
\left(a_2^{J=1}\right)_{\mathrm{b}} &= -\frac{E_\gamma^{J=1}}{4m_b}(1+\kappa_b) + O\left(\frac{E_\gamma^2}{m_b^2}\right) \approx -0.021(1+\kappa_b) \\
\left(a_2^{J=2}\right)_{\mathrm{b}} &= -\frac{3}{\sqrt{5}}\frac{E_\gamma^{J=1}}{4m_b}(1+\kappa_b) + O\left(\frac{E_\gamma^2}{m_b^2}\right) \approx -0.030(1+\kappa_b) \\
\left(b_2^{J=1}\right)_{\mathrm{b}} &= \frac{E_{\gamma'}^{J=1}}{4m_b}(1+\kappa_b) + O\left(\frac{E_\gamma^2}{m_b^2}\right) \approx 0.0065(1+\kappa_b) \\
\left(b_2^{J=2}\right)_{\mathrm{b}} &= \frac{3}{\sqrt{5}}\frac{E_{\gamma'}^{J=2}}{4m_b}(1+\kappa_b) + O\left(\frac{E_\gamma^2}{m_b^2}\right) \approx 0.0074(1+\kappa_b).
\end{aligned}$$

Using a bottom quark mass of $m_b = 5\,\mathrm{GeV}$ results in the multipole amplitudes being approximately $m_b/m_c \sim 3$ times smaller than for charmonia transitions. Furthermore, since the bottom quark has half the charge of the charm quark (in magnitude), the branching fractions for radiative decays in bottomonia are expected to be significantly smaller than those in charmonia. Using the PDG values of branching fraction measurements, we find that the branching fractions for bottomonia signal decays are approximately 3 times smaller than that of charmonia signal decays. Furthermore, the CLEO III $\Upsilon(2S)$ dataset is also approximately a factor of 3 times smaller with 9 million events. Therefore, we expect the statistical uncertainty from the fits to increase by a factor of $\sqrt{9} = 3$, to be approximately 0.02 and 0.05, for $a_2^{J=1}$ and $a_2^{J=2}$ respectively, which is roughly the expected multipole amplitude size. For this reason[4], this bottomonia analysis was not performed

[4]Additionally, there are issues with generation of CLEO III Monte Carlo events. The code to simulate the silicon vertex detector was never ported from the Solaris machines to the faster

with the CLEO III dataset. The B factories may be able to perform this type of analysis with their much larger $\Upsilon(2S)$ datasets.

Linux machines, so CLEO III Monte Carlo events would have to be generated on the few available Solaris machines. As this type of analysis requires a large phase space MC sample this becomes impractical.

CHAPTER 3

EXPERIMENTAL BACKGROUND

3.1 The CESR Accelerator

The CESR accelerator is a symmetric electron-positron collider located at Cornell University in Ithaca, NY, which consists of three separate particle accelerators: a linear accelerator (linac), a synchrotron, and a storage ring [36]. The acronym CESR stands for the Cornell Electron Storage Ring which is the name of the storage ring, though CESR is also used to refer to the entire accelerator facility. The CESR accelerator was used from October 1979 to March 3rd, 2008 for studies in experimental high energy physics doing pioneering and precision measurements for studies of bottom and charm physics. The acceleration process through the chain of accelerators is depicted in Figure 3.1. The storage ring and synchrotron are both located in the same tunnel $\approx$ 45 ft underground, with the storage ring being 768 m in circumference.

The acceleration process begins at the electron gun, which consists of a heated filament in a 150 kV potential. Electrons (e^-) from the electron gun are fed into the 30 m long linac, which can accelerate the electrons to up to 300 MeV. In the linac, the e^- are bunched into packets with 14 ns spacing and accelerated through the linac with the time-varying electric field in radio-frequency (RF) cavities. Positrons (e^+) are generated by inserting a tungsten target into the electron beam half the distance along the linear accelerator. When the e^- hit the tungsten target at an energy of $\approx$ 150 MeV, they produce electromagnetic showers in the tungsten which create many types of particles including e^+. The e^+ are then collected and accelerated to energies of up to 200 MeV through the second half of the linac.

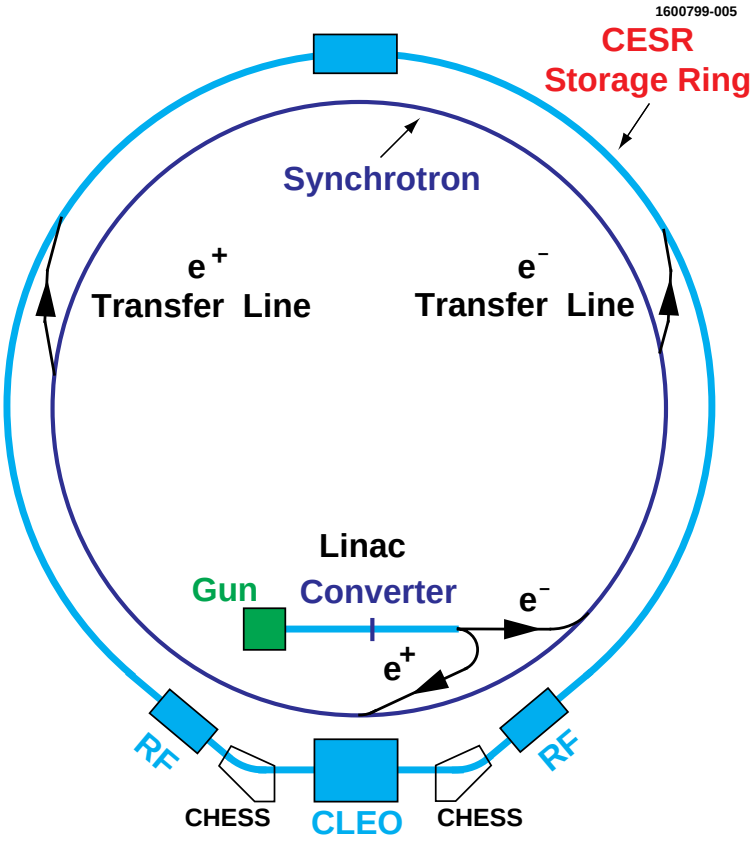

Figure 3.1: Schematic diagram of CESR.

Transfer lines from the linac to the synchrotron are curved in opposite directions, which acts to separate the electrons from the positrons and is also used to select the momentum of the particles as they enter the synchrotron.

The electrons and positrons entering the synchrotron travel in opposite directions in the circular accelerator. The synchrotron accelerates the particle bunches to their full energy through a series of four 3 m long linear accelerators. A series of dipole bending magnets are used to guide the beam along the circular trajectory. The accelerated bunches of particles are then injected into the storage ring via transfer lines at a rate of 60 Hz to accumulate beam current.

In the storage ring, 6.3 m long dipole magnets are used to bend the beam along

storage ring each with an 88 m bend radius. When operating in the low energy mode at center-of-mass energies of $E_{\rm cm} \approx 4\,{\rm GeV}$ as CESR-c (the c refers to charm energies), twelve magnetic wigglers are used in the storage ring for radiation damping of the beam to keep the beam emittance (the spread of particles in the beam in both real and momentum space) small. In the CLEO I-III mode of operation at energies of $E_{\rm cm} \approx 10\,{\rm GeV}$, natural radiation damping from the circular orbit achieved this. The wiggler is a series of 2.1 T magnets pointing in alternating directions arranged to cause the beam of charged particles to oscillate rapidly in the transverse direction. These accelerating charged particles lose energy through synchrotron radiation. As the energy lost due to synchrotron radiation is proportional to E^4, this reduces the beam emittance by reducing the momentum of the faster particles more than the slower particles. The energy lost from synchrotron radiation is then given back to the beam through superconducting RF cavities. In the CESR-c mode of operation near $E_{\rm cm} \approx 4\,{\rm GeV}$ with the radiation damping from the wiggler magnets, there is a 2.1 MeV spread in $E_{\rm cm}$.

The particles in the storage ring are grouped into bunches. Each bunch is about 40 ps (1.2 cm) in length and separated from the nearest bunch by 14 ns (4.2m). The bunches are grouped into trains, which are groups of three to five bunches. Up to nine trains are present in the storage ring and the trains are spaced ≈ 230 ns (≈ 70 m) from each other. As both the e^+ and e^- beams are stored in the same beam-pipe, "pretzel" orbits are used to avoid collisions at locations other than the interaction point (see Figure 3.2). Since there are up to 9 trains in each beam, there are 18 natural locations for interactions and only one desired interaction point where the detector is located. Therefore it is desired to eliminate 17 of the crossing points, 16 of which are eliminated by inserting four horizontal electrostatic separators which cause the bunches to oscillate in the horizontal plane. Collisions

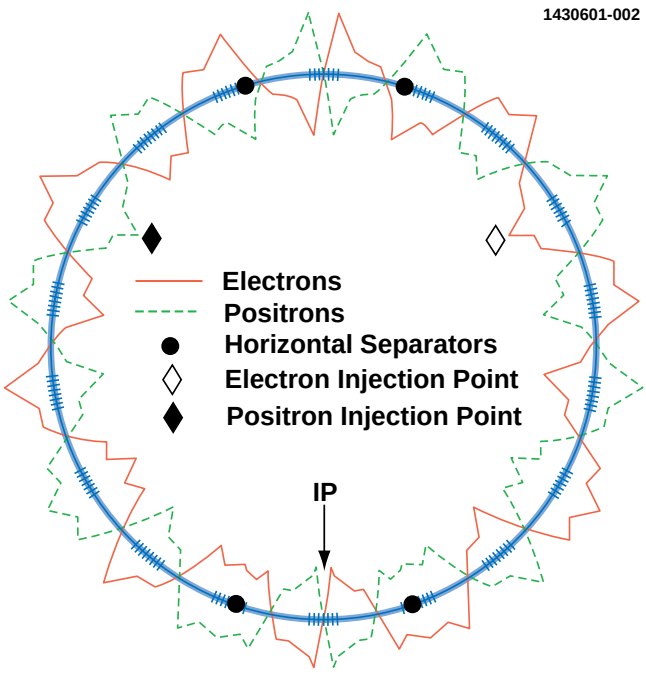

Figure 3.2: Diagram of Pretzel Orbits. Horizontal separation is greatly exaggerated; in the 768 m circumference storage ring the horizontal deviation from a circular orbit is ±20 mm.

are prevented at the north interaction region (directly opposite the interaction point) by additional vertical electrostatic separators.

At the interaction region, where the trains do intersect, a small crossing angle of $\sim \pm 2.5$ mrad is introduced in the horizontal plane. The crossing angle ensures that the bunches in the train only interact with each other at the specific interaction point at the center of the CLEO detector.

Besides its use as a electron positron collider for high energy physics, CESR was also designed to be used as a high intensity x-ray light source, as the Cornell High-Energy Synchrotron Source (CHESS) and continues to be used for this purpose even though the CLEO experiment has ended. The synchrotron radiation for

CHESS is generated when the electrons are accelerated by combinations of magnets designed to create intense x-ray beams that can be used for high-resolution materials research at the sub-nanometer scale.

3.2 The CLEO-c Detector

The CLEO detector was designed to detect tracks from charged particles and measure their momentum and velocity for particle identification, and measure energy from electromagnetic showers that can originate from photons or charged particles [21, 30]. CLEO-c is the fifth and final upgrade to the CLEO line of high energy physics detectors operating at CESR. The main goal of the CLEO-c upgrade to the CLEO III detector is to optimize performance while running CESR at charm energies ($E_{\rm cm} \approx 4\,\text{GeV}$) instead of near bottom energies ($E_{\rm cm} \approx 10\,\text{GeV}$).

CLEO-c is depicted in Figures 3.3 and 3.4. Tracks of charged particles are measured with the two cylindrical drift chambers which detect the path of a charged particle traveling through the chamber. The momentum of the charged particles is determined by the curvature of the track, as the two drift chambers sit in a 1.0 T magnetic field that is directed parallel to the beam axis. Enveloping the two drift chambers is a set of 7784 cesium iodide crystals, which act as an electromagnetic calorimeter absorbing all of the energy of photons and electrons that pass through the crystals.

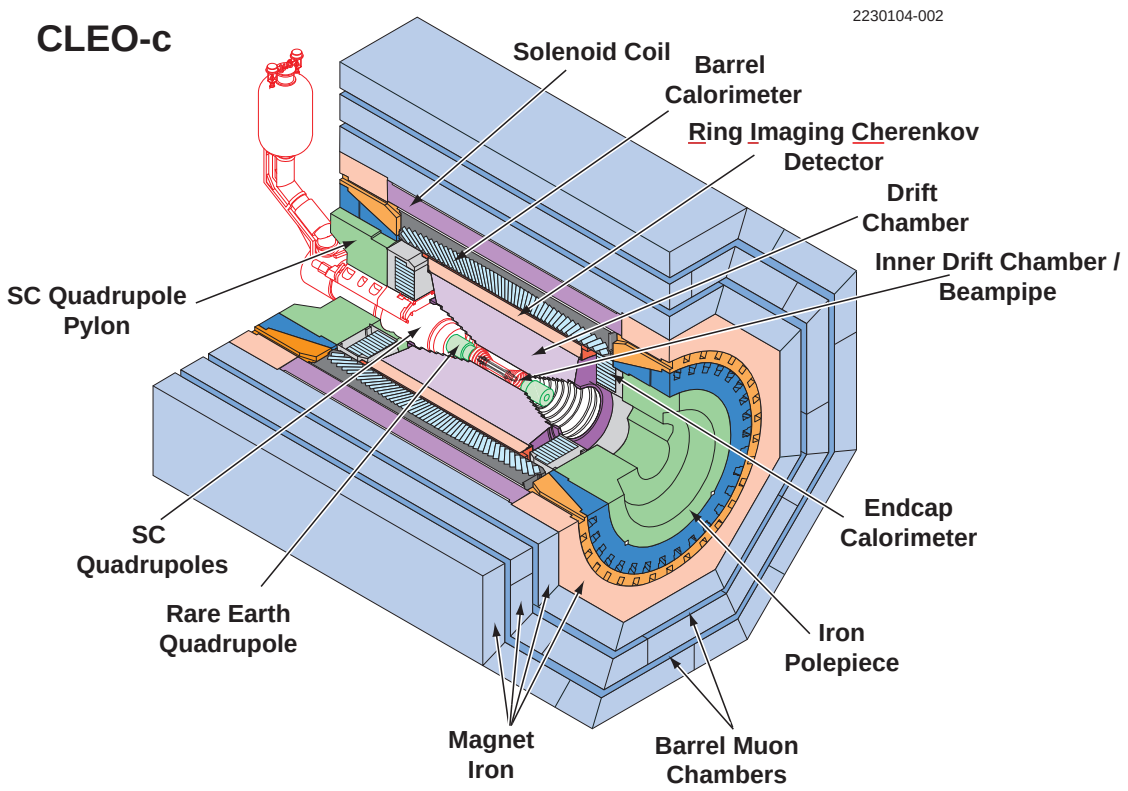

Figure 3.3: The CLEO-c detector

3.2.1 Drift Chambers

CLEO-c has two concentric drift chambers named the DR and ZD that are cylindrically symmetric about the CESR beam-pipe and centered about the interaction point. The DR is the larger outer drift chamber that is primarily used to determine the location of the charged particles; however, it has poor resolution in the z-direction (the direction parallel to the beam pipe). The smaller inner drift chamber, the ZD, was designed to have improved resolution in the z-direction to compensate for this problem.

Each drift chamber consists of many drift "cells" in a chamber filled with a 60% helium (He), 40% propane (C_3H_8) gas mixture. In the DR (ZD), each drift cell is

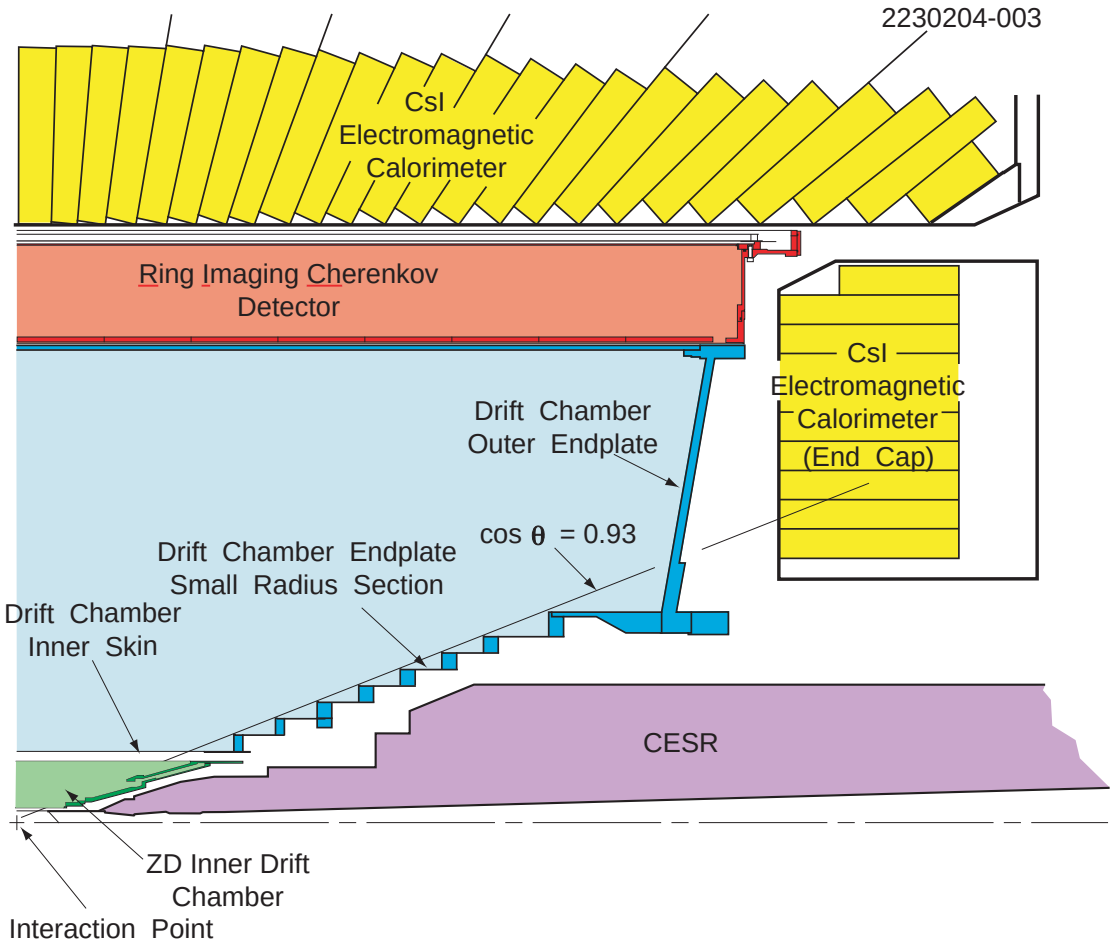

Figure 3.4: Diagram of cut-through of one quadrant of the CLEO-c detector

a set of nine parallel wires arranged in square array with the cell having a length of 1.4 cm (1.0 cm) across. The wire on the inside of the cell is a 20 μm-diameter sense wire consisting of gold-plated tungsten, and is surrounded by eight 110 μm-diameter gold-plated aluminum field wires. The sense wire is held at a potential +2100 V above the field wires, so electrons are attracted towards the sense wire. When a charged particle travels through the drift chamber it ionizes the $\mathrm{He}-\mathrm{C_3H_8}$ gas mixture creating several electron-ion pairs along the primary charged particle's path. The secondary electrons from these electron ion pairs then will drift towards the sense wire due to the large electric field. When these secondary electrons

approach the sense wire, they gain energy which they use to further ionize the helium-propane gas mixture through an avalanche process resulting in a signal with $\approx 10^7$ amplification. The majority of the drifting process occurs at a near-constant electron drift speed of 28 μm/ns, so the position measurement can be further improved by measuring the drift time to deduce the distance of closest approach. A Kalman filter is then used to apply the known physics models of energy loss to clean up the noisy data and perform a fit to deduce the trajectory of the particle.

For our angular analysis, we are concerned with the angular resolution of the drift chambers. The outer drift chamber achieved a momentum resolution of $\approx 0.6\%$ at $p = 1\,\mathrm{GeV}/c$ and an azimuthal and polar angular resolution of $\sigma_\phi \approx 1$ mrad and $\sigma_\theta \approx 4$ mrad [21].

The DR consists of 9976 drift cells that are arranged into 16 layers of axial drift cells that run parallel to the beam-pipe and 31 layers of stereo drift cells that alternate in a small angle to gain some information about the z-coordinate of the tracks. The ZD consists of 300 drift cells arranged in six layers with the three innermost layers and outermost layers having a large opposite stereo angle. When a sense wire individually receives an amplified signal from an avalanche, we only know that the avalanched signal hit the wire at some location along it, but do not know where along the direction parallel to the wire. Using the stereo drift cells, oriented at an angle relative to the other wires, we can reconstruct the z-coordinate of the track as the signal will be measured on multiple sense wires oriented at an angle relative to each other. The stereo wires in the DR are oriented at very small angles ($1.2^\circ - 1.7^\circ$), while the wires in the ZD have a large stereo angles of $12^\circ - 15^\circ$ allowing superior resolution in the z-direction.

Due to Lorentz forces, a charged particle will curve in a magnetic field with a radius of curvature (in the direction perpendicular to their magnetic field) that is proportional to its momentum (R/qB, where R is the radius of curvature, p is the momentum of the particle, q is the particle's charge, and B is the magnetic field). The sign of the charge of the particle can also be determined in this manner, since positive and negative particles curve in opposite directions. While CLEO III operated in a magnetic field of 1.5 T, the CLEO-c detector operated in a 1.0 T magnetic field due to the lower momentum range. The CLEO-c tracking system had a momentum resolution of approximately $\sigma_p/p \sim 0.6\%$ for tracks with a momentum of $1\,\mathrm{GeV}/c$. Angular coverage is central to our analysis and the drift chamber provides excellent coverage of nearly $\approx 93\%$ of the 4π solid angle as shown in Figure 3.4.

The drift chambers also give information about dE/dx, the rate at which the original charged particle is losing energy as it travels through the detector. Since the drift chamber has a gain of $\approx 10^7$, by measuring the decrease in the signal size as the particle moves through the detector it is possible to measure dE/dx. As indicated by the Bethe-Bloch equation, this rate of energy loss is a function of only the particle's velocity. Since a particle's momentum is also a simple function of its mass and velocity, it is possible to determine the mass of a particle from a measurement of its momentum and velocity. Therefore, the drift chamber can be used for particle identification purposes using momentum and dE/dx information. However for this analysis with a very low background of other events, we do not need to use dE/dx (or RICH) for particle identification.

3.2.2 Electromagnetic Crystal Calorimeter

The electromagnetic calorimeter consists of 7784 crystals that are constructed of cesium iodide that is doped with thallium. As depicted in Figure 3.4, the crystals are arranged into a barrel and endcap region and provide complete coverage for all angles less than $|\cos\theta| < 0.95$. However, CLEO typically excludes the part of the detector in the region $|\cos\theta| \geq 0.93$ and the transition region between $0.82 \leq |\cos\theta| \leq 0.85$, since these regions are difficult to properly calibrate resulting in a poorer quality data from these regions.

Each CsI(Tl) crystal is shaped into a rectangular prism shape with dimensions 5 cm × 5 cm × 30 cm. The radiation length for thallium doped cesium iodide is 1.9 cm and the Molière radius (the minimum radius transverse to the propagation direction for the crystal to absorb 90% of the electromagnetic energy of a high energy electron or photon) is 3.8 cm. Thus, the crystals should be able to easily absorb nearly all the energy of a photon or electron that passes through the crystal.

The crystals in the barrel are all oriented outward from the interaction region, so the photons and electrons that pass through the crystals will likely be completely absorbed as they must pass through ≈ 16 radiation lengths.

The electromagnetic calorimeter achieves an energy resolution of about $\sigma_E/E \sim 5\%$ at 100 MeV. The angular resolution of the detector for a 100 MeV photon is $\sigma_\phi \approx 11$ mrad (19 mrad) and $\sigma_\theta \approx 0.8\sigma_\phi \sin\theta$ (10 mrad) in the barrel (endcap) region of the crystal calorimeter.

In our analysis, we use the crystal calorimeter for particle identification in determining whether a set of particles into which the J/ψ decayed are two muons or two electrons. Since the lighter electrons will deposit most of their energy in

the calorimeter, while heavier muons will only deposit a small fraction of their energy, we can use the crystal calorimeter and drift chamber together for particle identification purposes. If we look at the ratio (E/p) of the energy deposited in the crystal calorimeter divided by the momentum of the track the shower is associated with, we can easily differentiate between $J/\psi \to \mu^+\mu^-$ and $J/\psi \to e^+e^-$ in our signal events.

3.2.3 Ring Imaging Cherenkov System

CLEO-c also has a Ring Imaging CHerenkov (RICH) system, which can be used to determine the velocity of the particle for particle identification [5]. The RICH is located between the DR and the crystal calorimeter barrel and covers angles with $|\cos\theta| \leq 0.80$. When a charged particle moves through a material with a speed faster than the speed of light in that material, it will emit Cherenkov radiation in a cone that has an angle that varies as $\cos\theta = 1/(n\beta)$ where n is the index of refraction and β is the particle's velocity divided by c. CLEO's RICH consists of a 1 cm thick lithium fluoride crystal radiator with an index of refraction of $n \approx 1.5$ (for 150 nm light), so it can only detect particles with velocities of $v > 2c/3$. When a high energy charged particle passes through the RICH, it first creates a cone of light that travels through a 16 cm N_2 expansion gap until it is projected as a ring on the other side of the gap. The light then passes through calcium fluoride windows, into a region of a methane-triethylamine mixture which excites photo-electrons that are amplified by a multi-wire proportional chamber. The methane-triethylamine gas mixture only allows the transmission of ultraviolet light with wavelength of 135-165 nm.

In this analysis, we do not use the RICH for particle identification purposes,

but it still could affect our analysis. The RICH has a significant amount of material between the beam pipe and the crystal calorimeter (13% of a radiation length).

3.3 Prior Experimental Results

Previous experimental results disagreed with theory which predicted ratios given in Eqs. (2.20-2.23). The ratios of the averages of previous experimental values compared with theory values are[1]:

$$\left(\frac{a_2^{J=1}}{a_2^{J=2}}\right)_{\rm exp} = \frac{-0.002 \pm 0.020}{-0.13 \pm 0.05} = 0.02^{+0.17}_{-0.16} \stackrel{?}{=} \left(\frac{a_2^{J=1}}{a_2^{J=2}}\right)_{\rm th} = 0.676 \quad (3.1)$$

$$\left(\frac{a_2^{J=1}}{b_2^{J=1}}\right)_{\rm exp} = \frac{-0.002 \pm 0.020}{0.077 \pm 0.050} = -0.02^{+0.30}_{-0.32} \stackrel{?}{=} \left(\frac{a_2^{J=1}}{b_2^{J=1}}\right)_{\rm th} = -2.27 \quad (3.2)$$

$$\left(\frac{b_2^{J=1}}{b_2^{J=2}}\right)_{\rm exp} = \frac{0.077 \pm 0.050}{0.132 \pm 0.075} = 0.54^{+0.75}_{-0.40} \stackrel{?}{=} \left(\frac{b_2^{J=1}}{b_2^{J=2}}\right)_{\rm th} = 1.000 \quad (3.3)$$

$$\left(\frac{a_2^{J=2}}{b_2^{J=2}}\right)_{\rm exp} = \frac{-0.13 \pm 0.05}{0.132 \pm 0.075} = -0.92^{+0.47}_{-1.08} \stackrel{?}{=} \left(\frac{a_2^{J=2}}{b_2^{J=2}}\right)_{\rm th} = -3.37. \quad (3.4)$$

[1]Errors were propagated by a toy Monte Carlo simulation using 10^7 values. The previously measured experimental averages were assumed to be Gaussian distributed and uncorrelated. The distribution that arises from the division of the two multipole amplitudes has long tails that do not fall off rapidly, due to the denominator having a significant probability of events occurring near 0. The long tail of the distribution makes the standard deviation computed by $\sigma = \sqrt{\langle X^2 \rangle - \langle X \rangle^2}$ poorly defined (*i.e.*, fluctuates rapidly between multiple experiments with 10^7 events). However, using the median and quantiles (corresponding to the standard deviations) we can describe the distribution of effects in a well defined manner, instead of quoting the mean and standard deviations. We base the quoted uncertainties to be the cutoffs, so we contain $\mathrm{erf}(1/\sqrt{2}) \cong 68\%$ of the events centered about the median. Using 2σ and 3σ (to contain $\sim 95.4\%$ and $\sim 99.7\%$ of the events centered around the median respectively), would make the values:

$$\left(\frac{a_2^{J=1}}{a_2^{J=2}}\right)_{\rm exp} = 0.02^{+0.49}_{-0.45}\big|_{2\sigma} = 0.02^{+3.4}_{-3.2}\big|_{3\sigma}$$

$$\left(\frac{a_2^{J=1}}{b_2^{J=1}}\right)_{\rm exp} = -0.02^{+1.7}_{-1.8}\big|_{2\sigma} = -0.02^{+29}_{-30}\big|_{3\sigma}$$

$$\left(\frac{b_2^{J=1}}{b_2^{J=2}}\right)_{\rm exp} = 0.54^{+4.5}_{-3.0}\big|_{2\sigma} = 0.54^{+67}_{-66}\big|_{3\sigma}$$

$$\left(\frac{a_2^{J=2}}{b_2^{J=2}}\right)_{\rm exp} = -0.92^{+5.3}_{-7.1}\big|_{2\sigma} = -0.92^{+110}_{-110}\big|_{3\sigma}$$

Only one ratio ($b_2^{J=1}/b_2^{J=2}$) is consistent with the theoretical predictions, while the other ratios significantly disagree. As the ratios are independent of m_c, κ_c and any specific quarkonia potential model to first order in $E_\gamma/(4m_c)$, we expect good agreement between theory and experiment. Tables 3.1 and 3.2 summarize the results from previous experiments for $J_\chi = 1$ and $J_\chi = 2$ respectively. Figure 3.5 compares the previous experimental values to the first-order theoretical predictions with $\kappa_c = 0$.

Table 3.1: Previous experimental values vs theoretical predictions for the normalized M2 amplitudes for the $J_\chi = 1$ decays. The Crystal Ball experiment at SPEAR was an $e^+e^- \to \psi'$ experiment similar to CLEO and studied the same decay sequence. The E835 experiment at Fermilab is a $p\bar{p} \to \chi_{c1}$ experiment, so was only sensitive to a amplitudes. The CLEO-c data have $\simeq$40000 $J_\chi = 1$ signal events after applying selection criteria.

Experiment	$a_2^{J=1}$	$b_2^{J=1}$	Signal events
Crystal Ball [29]	$-0.002^{+0.008}_{-0.020}$	$0.077^{+0.050}_{-0.045}$	921
E835 [2]	$0.002 \pm 0.032 \pm 0.004$		2090
Theory ($m_c = 1.5\,\mathrm{GeV}$)	$-0.065(1+\kappa_c)$	$0.029(1+\kappa_c)$	

Table 3.2: Previous experimental values vs theoretical predictions for the normalized M2 amplitudes for the $J_\chi = 2$ decays. The Crystal Ball experiment at SPEAR was an $e^+e^- \to \psi'$ experiment similar to CLEO and studied the same decay sequence. The E760 and E835 experiments at Fermilabs were $p\bar{p} \to \chi_{c2}$ experiments, so were only sensitive to a amplitudes. The BESII experiment looked for $\psi' \to \gamma\chi_{c2} \to \gamma(K^+K^-)$ or $\gamma(\pi^+\pi^-)$ and also found $b_3^{J=2} = -0.027^{+0.043}_{-0.029}$. The CLEO-c data have $\simeq$20000 $J_\chi = 2$ signal events after applying selection criteria.

Experiment	$a_2^{J=2}$	$b_2^{J=2}$	Signal events
Crystal Ball [29]	$-0.333^{+0.116}_{-0.292}$	$0.132^{+0.098}_{-0.075}$	441
E760 [4]	-0.14 ± 0.06		1904
E835 [2]	$-0.093^{+0.039}_{-0.041} \pm 0.006$		5908
BESII [1]		$-0.051^{+0.054}_{-0.036}$	731
Theory ($m_c = 1.5\,\mathrm{GeV}$)	$-0.096(1+\kappa_c)$	$0.029(1+\kappa_c)$	

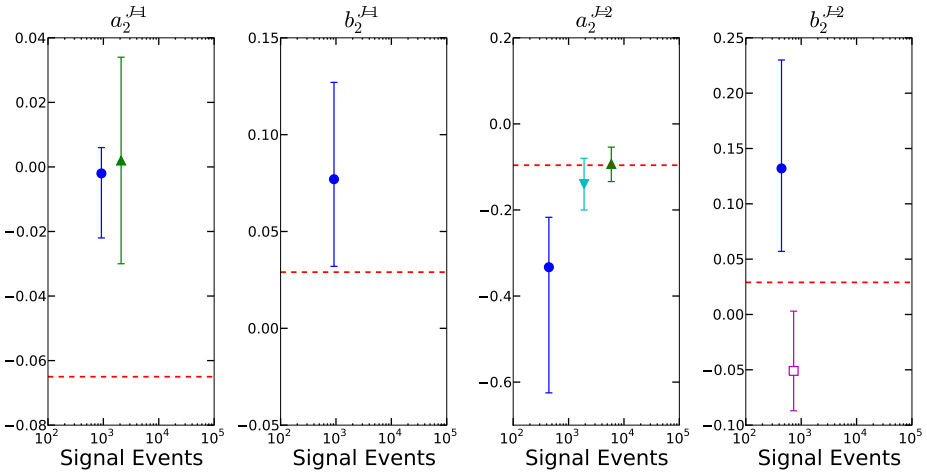

Figure 3.5: Magnetic quadrupole amplitudes from previous analyses compared with theoretical expectations. Crystal Ball results are blue circles (●) [29], the E760 result is a cyan inverted triangle (▼) [4], the E835 results are green triangles (▲) [2], the BESII result is a purple open square (□) [1], and the theoretical expectation given by Eqs. (2.15-2.18) with $m_c = 1.5\,\text{GeV}$ and $\kappa_c = 0$ is a dashed red line (- - -).

3.3.1 Crystal Ball Experiment

The Crystal Ball collaboration performed a similar analysis searching for the magnetic quadrupole amplitudes in the same decay sequences with the e^+e^- collider at SPEAR [29, 28]. They used a binned maximum likelihood fit where the 921 selected $J_\chi = 1$ and 441 selected $J_\chi = 2$ signal events were divided into $3^4 \cdot 6 = 486$ bins over the five variables $(\cos\theta', \phi', \cos\theta_{\gamma\gamma'}, \cos\theta, \phi)$. Since the PDF $W(\Omega; \mathbb{A})$ is symmetric under several parity transformations given by Eqs. (2.10 - 2.14), it is possible to fold four of the five angles into the positive domain. This significantly increases the statistical precision in a binned likelihood fit, though has no effect on our unbinned likelihood method. Each folded angle was split into three equally sized bins, with the exception of ϕ which was split into six bins as it ran

from $[-\pi, \pi]$. To perform the binned likelihood fit, they compared $\langle n_i(\mathbb{A})\rangle$, the expected number of events in the i-th bin for the given value of the multipole parameters, with n_i, the number of events observed in each bin.

They compared the two histograms with the likelihood derived from the Poisson distribution (which was simplified by fixing the total number of expected events to the number of observed events) as

$$L(\mathbb{A}) = \prod_{i=1}^{486} \frac{\langle n_i(\mathbb{A})\rangle^{n_i}}{n_i!}.$$

According to [28], "each spin-multipole hypothesis $\tilde{p}$ [$\tilde{p} \equiv J_\chi, a_2, b_2$ in our notation] required a binned Monte Carlo simulation which was acceptance corrected and constrained to have a total number of events equal to that in the experimental data sample". The number of phase space Monte Carlo events created selected via the rejection method is not given and neither is the number of spin-multipole hypotheses considered. They found starkly different results from the expected theoretical values and their experimental values are quite different from the results of this analysis shown in later sections.

3.3.2 Fermilab $p\bar{p}$ Experiments

The E760 [4] and follow-up E835 [2] experiments at Fermilab searched for multipole amplitudes in radiative charmonium transitions starting with a χ_{cJ} state created at a $p\bar{p}$ collider. Due to charge conjugation invariance (as well as parity and angular momentum conservation), the helicity of the χ_c is ± 1 when formed via $p\bar{p} \to \chi_{c1}$. Technically, according to [23], [10], and [7], the helicity 0 production amplitude for χ_{c1}, B_0, is only suppressed to $O(1/Q^2)$, where Q is the momentum transfer scale. Only E835 published a result for χ_{c1} and they found $a_2^{J=1} = 0.002 \pm 0.032 \pm 0.004$

with 2090 events after the cuts with a $\chi^2/N_{dof} = 87.3/96$. For χ_{c2}, E835 found with 5908 events after cuts, that $a_2^{J=2} = -0.093^{+0.039}_{-0.041} \pm 0.006$ when they constrained $a_3 \equiv 0$ with a $\chi^2/N_{dof} = 99.4/94$. Allowing for an E3 amplitude, E835 found $a_2^{J=2} = -0.076^{+0.054}_{-0.050} \pm 0.009$ and $a_3^{J=2} = 0.020^{+0.055}_{-0.044} \pm 0.009$ with $\chi^2/N_{dof} = 98.9/93$.

E760 had less sensitive results as they had only 1904 events after selection criteria. They found for $a_2^{J=2} = -0.14 \pm 0.06$ holding $a_3 \equiv 0$, and allowing for E3 amplitudes they found $a_2^{J=2} = -0.14^{+0.08}_{-0.07}$ and $a_3^{J=2} = 0.00^{+0.06}_{-0.05}$.

3.3.3 BESII Polarization Experiments

An alternative method to measure the multipole amplitudes for the transition $e^+e^- \to \psi' \to \gamma\chi_{c2}$ is to measure the helicity of the χ_{c2} by observing the decays $\chi_{c2} \to K^+K^-$ and $\chi_{c2} \to \pi^+\pi^-$. One of the benefits of this method is that there is no background from $\chi_{c1} \to (\pi^+\pi^-, K^+K^-)$ as the χ_{c1} decays are forbidden by parity conservation. BESII used their 14.0 ± 0.6 million ψ' dataset to find 418 $\chi_{c2} \to \pi^+\pi^-$ events and 303 $\chi_{c2} \to K^+K^-$ events. Performing a χ^2 likelihood fit, they found $b_2^{J=2} = -0.051^{+0.054}_{-0.036}$ and $b_3^{J=2} = -0.027^{+0.043}_{-0.029}$.

CLEO-c has studied the same decay sequences to establish branching fractions for the decay rates [6]. However, no attempt at extracting the multipole amplitudes was performed.

3.4 Datasets and Monte Carlo Samples Used

3.4.1 CLEO-c Datasets

There are two CLEO-c datasets taken at the ψ' resonance: `data42` with $(24.45 \pm 0.49) \times 10^6$ ψ' events and `data32` with $(1.44 \pm 0.03) \times 10^6$ ψ' events [26, 25]. `Data42` was taken August 22, 2006 to September 18, 2006 and consists of 747 good runs, contains 76,306,513 events and had a total luminosity of 48.07/pb. `Data32` was taken December 2, 2003 to January 6, 2004 and consists of 104 good runs at the ψ' resonance with 7,234,486 events and had a luminosity of 3.3/pb. As all of our generic Monte Carlo studies and phase space events have been based on the run parameters of `data42`, we elect to not include any `data32` events in our studies. Including `data32` would increase our data sample by 5.9%, which we expect would reduce the statistical uncertainty by only 2.8%. However, including events from `data32` alongside events from `data42` could introduce a larger unknown systematic uncertainty.

3.4.2 Expected Number of CLEO Events

Using the known branching fractions from the PDG [3] and the known sizes of the CLEO data samples [26, 25], we can estimate the number of signal events originally present in `data42`. As shown in Table 3.3, we expect 91900 ± 6600 $J_\chi = 1$ signal events and 48200 ± 3600 $J_\chi = 2$ signal events to be present in `data42`.

Table 3.3: The number of expected CLEO signal events with the PDG branching fractions in `data42`, which has $(24.45 \pm 0.49) \times 10^6$ ψ' events present. This calculation of number of signal events does not account for the detector efficiency from our selection criteria of about $\approx 40\%$.

J_χ	$\mathcal{B}(\psi' \to \gamma'\chi_c)$ (10^{-2})	$\mathcal{B}(\chi \to \gamma J/\psi)$ (10^{-2})	$\mathcal{B}(J/\psi \to e^+e^-) + \mathcal{B}(J/\psi \to \mu^+\mu^-)$ (10^{-2})	Signal events
0	9.4 ± 0.4	1.28 ± 0.11	$[(5.94 \pm 0.06) + (5.93 \pm 0.06)]$	3500 ± 350
1	8.8 ± 0.4	36.0 ± 1.9	$[(5.94 \pm 0.06) + (5.93 \pm 0.06)]$	91900 ± 6600
2	8.3 ± 0.4	20.0 ± 1.0	$[(5.94 \pm 0.06) + (5.93 \pm 0.06)]$	48200 ± 3600

3.4.3 Phase Space Monte Carlo Sample

For each of the decay sequences ($J_\chi = 1$ and $J_\chi = 2$), a 4.5 million event phase space Monte Carlo data sample was generated. The phase space MC was generated with EvtGen [22] using $\psi' \to \gamma'\chi_{(c1,c2)}$ (`PHSP`) followed by $\chi_{(c1,c2)} \to \gamma J/\psi$ (`PHSP`) with $J/\psi \to \ell^+\ell^-$(`VLL` with `PHOTOS` for final state radiation (FSR) [8]). The MC generated events are run through `GEANT` to simulate the interaction of the simulated events with the detector [12]. Each event was reconstructed using CLEO reconstruction software.

The purposes of the phase space Monte Carlo events are twofold. First, it is used to account for the variable angular efficiency of the detector after the cuts have been applied, when performing the maximum likelihood fit. This is done by approximating the efficiency integrals via Monte Carlo integration techniques (see Section 4.2).

Second, the phase space MC events are used to simulate "signal" MC with non-zero multipole amplitudes, a_2, b_2 (and a_3, b_3 for $J_\chi = 2$) via the rejection method. This is achieved by taking the five angles $\theta', \phi', \theta_{\gamma\gamma'}, \theta, \phi$ for each phase space event and calculating the probability of that event occurring at those angles for the PDF

$W(\Omega;\mathbb{A}_0)$ with the input values of the multipole amplitudes $\mathbb{A}_0$. The $W(\Omega;\mathbb{A}_0)$ is appropriately normalized by dividing by the maximum value $W(\Omega;\mathbb{A}_0)^{\rm Max}$, so that the $W(\Omega;\mathbb{A}_0)$ is a value between 0 and 1 for all phase space events. This probability for each event to occur is compared to a random number r uniformly distributed between 0 and 1 that is generated for each event. We keep events that are more probable than the random cutoff variable ($W(\Omega;\mathbb{A}_0) > r$) and reject the other events, so that the kept events now follow $W(\Omega;\mathbb{A}_0)$.

These "signal" events (from selecting phase space MC via the rejection method) are used for two distinct purposes. First, they are used to generate a large number of signal Monte Carlo datasets obeying a given PDF $W(\Omega;\mathbb{A}_0)$ for tests of ensembles of fits. Second, they are used to compare histograms of data to histograms of many "signal" events selected according to $W(\Omega;\mathbb{A}_0)$ with different input values of $\mathbb{A}_0$. This allows us to quantify (via a reduced χ^2) how well the data match the fitted values of $\mathbb{A}$ and the pure E1 value of $\mathbb{A}$, as shown in Figures 4.18, 4.19, etc.

3.4.4 Generic Monte Carlo Sample

A large sample of ψ' generic Monte Carlo events generated with conditions simulating `data42` with a five-fold increase in luminosity was used to simulate the backgrounds. Generic Monte Carlo events are simulated events for all the known decay sequences that can occur starting from our particular running conditions, generated by using all the previously measured branching fractions with the most appropriate physics models available for their decay sequences. The generic Monte Carlo sample is meant to simulate the actual data sample from running at the ψ' resonance, and is useful since we can then ask which non-signal events pass the selection criteria.

The five-fold generic Monte Carlo dataset was split into five datasets of ∼24 million events, so we can simulate the impure events that would be selected from five independent analyses. The generic MC dataset was slightly modified from the original `data42` generic MC dataset, to explicitly remove the decay $J/\psi \to \gamma e^+ e^-$ `(PHSP)` that was included in the `20080624_MCGEN` release[2] of `DECAY.DEC`[3]. This decay is listed in the PDG [3], but it is already accounted for in EvtGen with the $J/\psi \to e^+ e^-$ (`VLL`) when it adds in final state radiation with `PHOTOS`. Also this decay would be extremely poorly modeled by being thrown with the `PHSP` EvtGen model, which would randomly split up the energy and momentum equally among all three particles (the electron, positron, and photon).

[2]The various releases of the CLEO analysis software are listed by the date of release and the purpose of the release. In this case, it was released on June 24th, 2008 and is used primarily for MC generation.

[3]`DECAY.DEC` is a file that contains all the decay models simulated in the generic MC.

CHAPTER 4

THE DATA ANALYSIS

4.1 Selection Criteria

Selection criteria were optimized looking at a Monte Carlo dataset comprised of background events from five independent 24 million ψ' generic MC datasets with the signal events ($\psi' \to \gamma'\chi_{(c1,c2)} \to \gamma'\gamma J/\psi$) replaced with phase space MC events selected to have the desired a_2 and b_2 admixture (via the rejection method as described in Section 3.4.3). The overall goal of this tuning of the selection criteria is to eliminate the non-signal "impure" background events, while selecting the largest number of signal events. For regions where it was uncertain where to apply a selection criterion (also known as a cut), we attempted to minimize the quadrature sum of the statistical uncertainty from signal events with the systematic uncertainty from impure events. Many of the starting points for our selection criteria are taken from Heltsley and Mahlke's CLEO-c study [16, 25] of $\psi' \to h + J/\psi$ branching fractions that included our signal decays.

Plots describing the variables being used for selection criteria are given in section 4.1.6 and 4.1.7. For each variable considered for use as a selection criterion, we apply all of the selection criteria described at the beginning of 4.1.6 and 4.1.7 for events from both `data42` and from the fivefold generic Monte Carlo events for the run conditions of `data42`. In the histograms, we scale the 120M event five-fold `data42` to the total number of events in the `data42` histogram.

For the histograms that follow that compare Generic MC to data, we do not replace the generic Monte Carlo signal events with phase space selected via rejec-

tion method "signal" events. For variables that are used in the cuts, the locations of the cuts are indicated by cyan dashed lines.

4.1.1 Initial Cuts To Obtain Two Photons and Two Tracks

All tracks and showers investigated are required to pass the standard `GoodThingsProd` criteria prior to any attempts at kinematic fitting. The `GoodThingsProd` is a set of standard selection criteria to require that the tracks and showers pass a minimal set of criteria.

For tracks, this means that the fit based on a Kalman filter is performed with a reduced χ^2 of less than 50, the track's trajectory has a hit fraction of greater than 0.5, the radial distance of closest approach is less than 2 cm, the z_0 location at closest approach is less than 10 cm from the interaction point, the momentum is between 1%-120% (18.4 MeV/c - 2.21 GeV/c) of the beam momentum, $|\cos\theta|$ is less than 0.93, the uncertainty on $\cot\theta$ is less than 0.3, and the uncertainty on z_0 less than 50 cm.

The "GoodThings" requirement for showers is that the showers must not be matched to a track, must be in the GoodBarrel or GoodEndcap regions (which respectively mean that $|\cos\theta| \leq 0.79$ or $0.85 \leq |\cos\theta| \leq 0.93$), must not be from a noisy crystal, and must have an energy between 1%-120% of the beam energy (18.4 MeV - 2.21 GeV).

For the GoodBarrel requirement, we tighten the standard cut of $|\cos\theta| \leq 0.82$ to $|\cos\theta| \leq 0.79$. We had found that the detector efficiency in data was $\sim 30\%$ lower than in Monte Carlo in the region of $0.80 \leq |\cos\theta| \leq 0.82$, which corresponds to the second-to-last row of crystals in the calorimeter. This region is expected

to be poorly modeled in the Monte Carlo as the last row consists of half-crystals, which could significantly affect the calibration of the penultimate row due to edge effects. There could also be an effect from the gas piping and cabling into the RICH endplates, since the Monte Carlo calibration of the crystal calorimeter was performed before the RICH was installed.

4.1.2 Kinematic Fitting to ψ Four-vector and J/ψ Mass

All candidate events require at least two tracks and two showers to be identified. The two tracks and two showers used (if more are present) will be those with the greatest momenta and energies. Two kinematic fits are then performed to generate the four four-vectors used in the analysis. First, a 1C kinematic fit to the J/ψ mass is performed starting with the two tracks, allowing any showers identified as bremsstrahlung photons associated with a track to be added back to the four-vector of that track. If a shower from a neutral particle is within a 100 mrad cone of a track (measured from the interaction point), we call it a bremsstrahlung photon and include it in the 1C reconstruction to the J/ψ mass.

Second, a 4C kinematic fit to the ψ' four-vector is performed and the result of this fit is then backpropagated through the original 1C fit. The ψ' four-vector is calculated from the crossing angle and the beam energy of the given run with the `LabNet4Momentum` package, which calculates the four-vector from the beam energy of a particular run and the small crossing angle of 3 mrad. We slightly adjust this ψ' four-vector to make sure it corresponds to the invariant mass of the ψ'.

For both the 1C and 4C kinematic fits, we require that the reduced χ^2 for both the vertex and kinematic fit is less than 16. This cut value of 16 was found

by minimizing the quadrature sum of the impurity systematic uncertainty and statistical uncertainty,

$$\sigma_{\text{quad sum}} = \sqrt{\frac{N_0^{\text{sig}}}{N^{\text{sig}}}(\sigma_0^{\text{stat}})^2 + \left(\frac{N^{\text{imp}}\sigma_0^{\text{sys imp}}}{N_0^{\text{imp}}}\right)^2} \tag{4.1}$$

as shown in Table 4.1. We performed the minimization by recognizing that the impurity systematic uncertainty was approximately linearly proportional to the number of impure events included in the fit, and that the statistical uncertainty is inversely proportional to the square of the number of signal events.

Table 4.1: Study to find the optimal value of the cutoff for the maximum reduced χ^2 is 16. We had found that the statistical uncertainty of the fit varies approximately as $\sigma^{\text{stat}} \propto 1/\sqrt{N^{\text{sig}}}$ and that the systematic uncertainty from impure events is approximately proportional to the number of non-signal events $\sigma^{\text{sys imp}} \propto N^{\text{imp}}$. For $J_\chi = 1$, we attempted to minimize the quadrature sum of the statistical uncertainty and impurity systematic uncertainty for a_2, which is given by equation 4.1, where we used $N_0^{\text{sig}} = 41820$, $\sigma_0^{\text{stat}} = 0.0060$, $N_0^{\text{imp}} = 195$, $\sigma_0^{\text{sys imp}} = 0.0023$ as input into the equation along with counted the number of signal and impure events at different cutoffs.

χ^2_{cutoff}	N^{sig}	N^{imp}	$\sigma_{\text{quad sum}}$
1	2387	0	0.026
3	19851	15	0.0089
5	30167	24	0.0072
10	37718	49	0.0065
15	39829	84	0.00642
16	40088	93	0.00641
17	40316	101	0.00642
20	40808	117	0.0065
25	41384	153	0.0066
30	41820	197	0.0069

4.1.3 Identification of Signal Events

To identify signal events through the J_χ radiative cascade being considered, we require that the reconstructed χ_{cJ} mass is within 15 MeV of the true χ_{cJ} mass as constructed by adding the J/ψ and γ four-vectors together:

$$\begin{aligned} m_{\chi_{cJ}} &= \sqrt{|p_{J/\psi} + p_\gamma|^2} \\ &= \sqrt{|p_{\ell^+} + p_{\ell^-} + p_\gamma|^2} \end{aligned}$$

Due to the 4C kinematic fit, this is in practice equivalent to requiring that the χ_{cJ} mass be reconstructed from the ψ' and γ' four-vectors, so this redundant cut is not applied.

Signal events must also have the J/ψ decay to e^+e^- or $\mu^+\mu^-$, so we require the two tracks to be well-identified as both being electrons or muons. We achieve this by looking at the ratio E/p of the energy deposited in the calorimeter to the momentum of the track. We identify both tracks as electrons if the lower E/p ratio is greater than 0.5 and the higher E/p ratio is greater than 0.85. Similarly, we identify both tracks as muons if $E/p|_{\text{lower}} < 0.25$ and $E/p|_{\text{higher}} < 0.5$.

4.1.4 Reduction of Background Modes

To restrict the major background modes, we apply an additional set of cuts for the modes with the following branching fractions:

$$\mathcal{B}(\psi' \to \pi^0\pi^0 J/\psi) = (16.84 \pm 0.33)\%$$

$$\mathcal{B}(\psi' \to \eta J/\psi) = (3.16 \pm 0.07)\%$$

$$\mathcal{B}(\psi' \to \pi^0 J/\psi) = (1.26 \pm 0.13) \times 10^{-3}.$$

The dominant background mode $\psi' \to \pi^0\pi^0 J/\psi \to \gamma\gamma\gamma\gamma\ell^+\ell^-$ is reduced by requiring that the third most energetic shower in the event (excluding those photons identified as bremsstrahlung photons) has an energy of less than 30 MeV. To reduce the modes $\psi' \to \eta J/\psi \to \gamma\gamma J/\psi$ and $\psi' \to \pi^0 J/\psi \to \gamma\gamma J/\psi$, we note that both of these modes have a monochromatic J/ψ momentum, where $p(J/\psi)|_{\psi'\to\eta J/\psi} = 199\,\mathrm{MeV}/c$ and $p(J/\psi)|_{\psi'\to\pi^0 J/\psi} = 528\,\mathrm{MeV}/c$. Therefore, we require the J/ψ momentum to be between $240\,\mathrm{MeV}/c$ and $510\,\mathrm{MeV}/c$. Note that due to the kinematics of the signal transition, there are no signal events with a J/ψ momentum below 238 MeV/c (318 MeV/c for $J_\chi = 2$) or above 542 MeV/c.

4.1.5 Other Cuts Considered Though Not Applied

Several other selection criteria were considered, but were not included in the selection criteria we applied to select signal events as they were redundant. The formerly considered cuts are:

- the χ_c mass constructed from the ψ' and γ' four-vectors,
- the two track invariant mass, and
- the two photon recoiling mass.

The χ_c mass constructed from the ψ' and γ' four-vectors is defined as $m = \sqrt{|p_{\mathrm{lab}} - p_{\gamma'}|^2}$, and is redundant with the other χ_c mass fit, due to the 4C kinematic fit to the ψ' mass.

The two track invariant mass is defined as $m = \sqrt{|p_{\ell^+} + p^{\ell^-}|^2}$, which should be near the J/ψ mass for signal events. However, this criterion is automatically

satisfied by the nature of the 1C kinematic fit to the J/ψ mass, making this cut redundant.

Similarly, the photon recoiling mass is defined as $m = \sqrt{|p_{\rm lab} - p_{\gamma'} - p_{\gamma}|^2}$, which should also correspond to the J/ψ mass. However, the combination of the 1C and 4C fits to the J/ψ and ψ' mass ensures that this photon recoiling mass is also satisfied.

4.1.6 $\psi' \to \gamma'\chi_{c1} \to \gamma'\gamma J/\psi$ transitions

The cuts for $J_\chi = 1$ transitions that are made are summarized here:

Reduced χ^2 Require all reduced χ^2 from kinematic fits to be less than 16 (including vertex fits).

E/p Require for $J/\psi \to \mu^+\mu^-$ that $(E/p)_{\rm larger} < 0.5$ and $(E/p)_{\rm smaller} < 0.25$, and for $J/\psi \to e^+e^-$ that $(E/p)_{\rm larger} > 0.85$ and $(E/p)_{\rm smaller} > 0.5$.

χ_c mass Require that the χ_c mass constructed from $m = \sqrt{|p_{J/\psi} + p_{\gamma}|^2}$ is within $0.015\,{\rm GeV}$ of the $m_{\chi_{c1}} = 3.511\,{\rm GeV}$.

J/ψ momentum Require that the J/ψ momentum is between $0.24\,{\rm GeV}/c$ and $0.51\,{\rm GeV}/c$.

Third Most Energetic Shower Require that the maximum energy of the third most energetic shower is less than 30 MeV.

GoodThingsProd Standard "GoodThings" cuts as described in section 4.1.1.

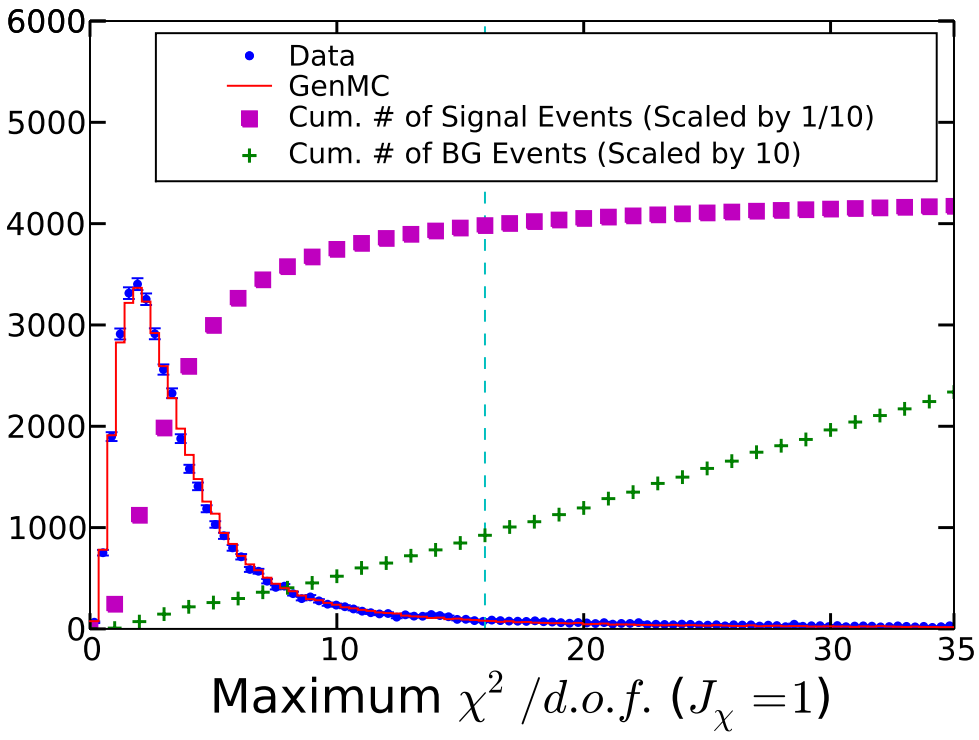

Figure 4.1: Plot of maximum reduced χ^2 in all kinematic fits (including vertex fits) in generic Monte Carlo and data. Events with a maximum reduced χ^2 below 16 (the dashed cyan line) are kept. Cumulative totals for the number of signal and impurity background events are also plotted for each potential value of a χ^2 cut.

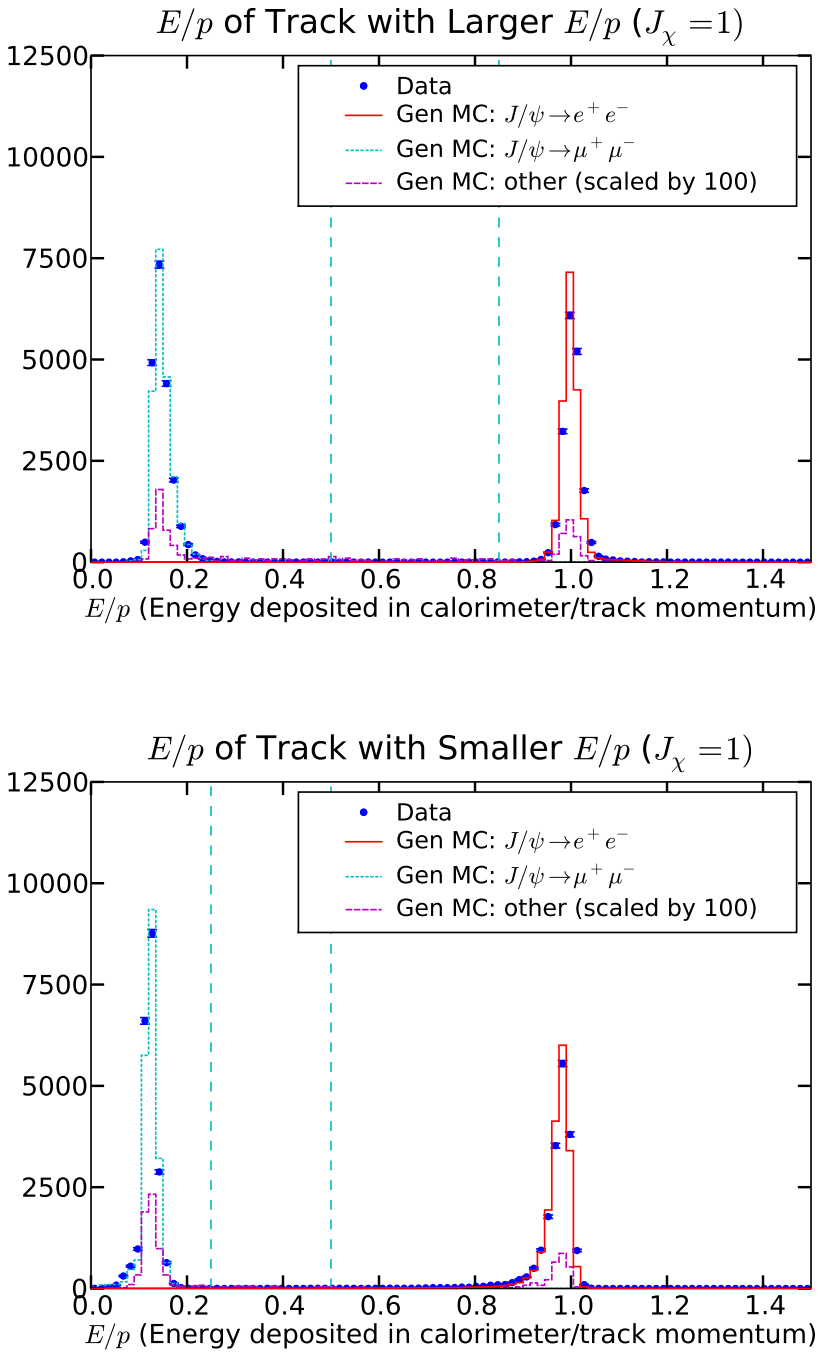

Figure 4.2: Plot of E/p, the ratio of the energy (GeV) deposited in the calorimeter to the track momentum (GeV/c) for both tracks. For each event, we histogram the E/p from the track with the larger and smaller ratio and apply different criteria. The purpose of these cuts is to separate events with $J/\psi \to \mu^+\mu^-$ and $J/\psi \to e^+e^-$, which are well differentiated with these cuts.

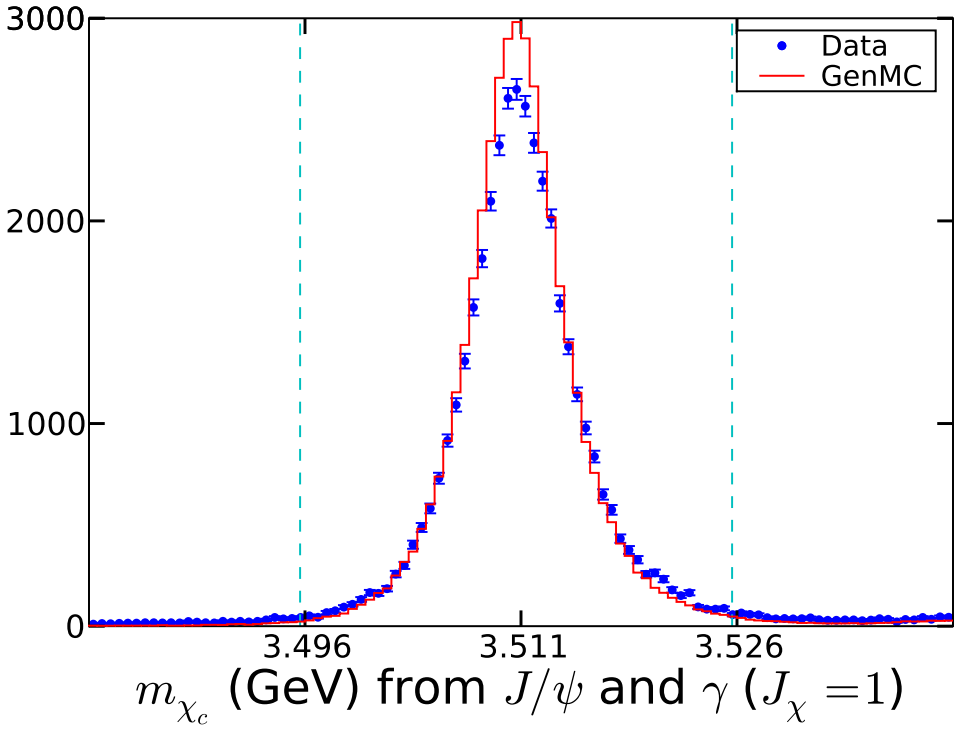

Figure 4.3: Plot of the χ_c mass constructed by the four-vectors of γ and J/ψ. The kinematic fits ensure that this cut is redundant with the cut on the χ_c mass constructed by subtracting the γ' four-vector from the ψ' four-vector.

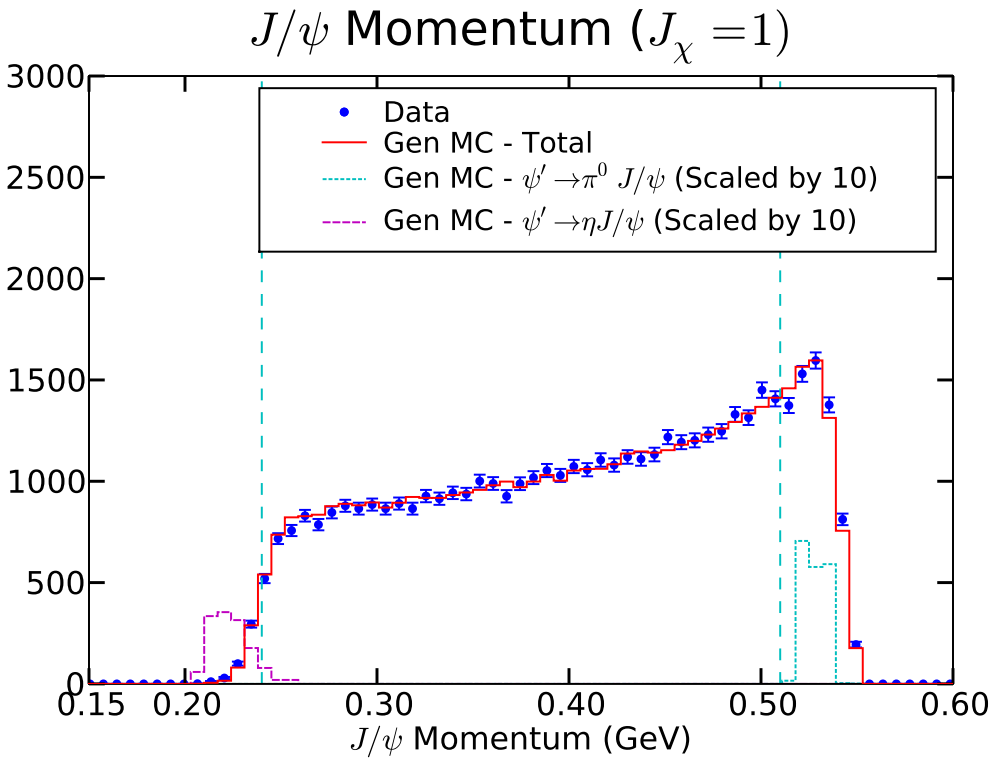

Figure 4.4: Plot of the J/ψ momentum to indicate removal of the two background modes of $\psi' \to \pi^0 J/\psi$ ($p_{J/\psi} = 528\,\mathrm{MeV}/c$) and $\psi' \to \eta J/\psi$ ($p_{J/\psi} = 199\,\mathrm{MeV}/c$). The two background modes removed with the J/ψ momentum cut are scaled up by a factor of 10, so they are visible in comparison to the signal.

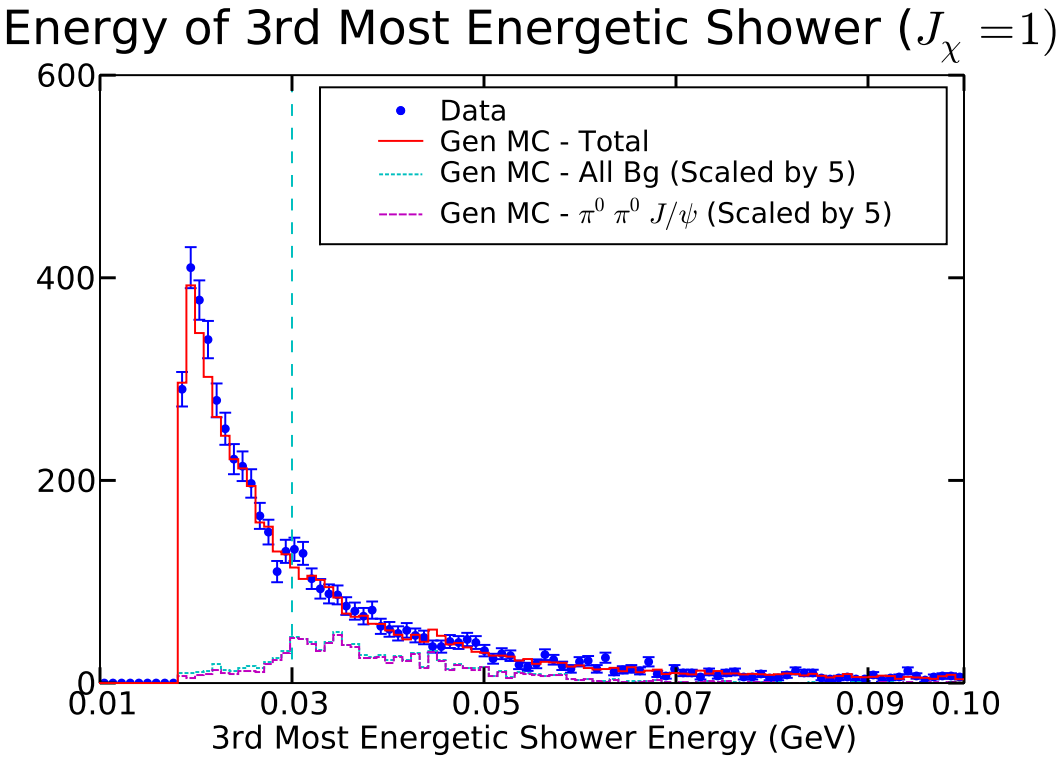

Figure 4.5: Plot of the energy of the third most energetic shower. Note the 'GoodThingsProd' enforces that a 'Good' shower has an energy of greater than 18.4 MeV (1% of the beam energy). This creates many off-scale events with a shower energy of 0. In Generic MC (Data), 87.2%=192704/221057 (87.4% = 37800/43270) of events have a third shower energy of less than 18 MeV. In the five-times `data42` generic MC dataset with 120 million ψ' events, there are a total of 1061 $\pi^0\pi^0 J/\psi$ background events of which 93 have $E_{\rm 3rdshwr} < 18\,{\rm MeV}$ and 282 have $E_{\rm 3rdshwr} < 30\,{\rm MeV}$ (the current cut value), while there were 192704 total events with $E_{\rm 3rdshwr} < 18\,{\rm MeV}$ and 208914 total events with $E_{\rm 3rdshwr} < 30\,{\rm MeV}$.

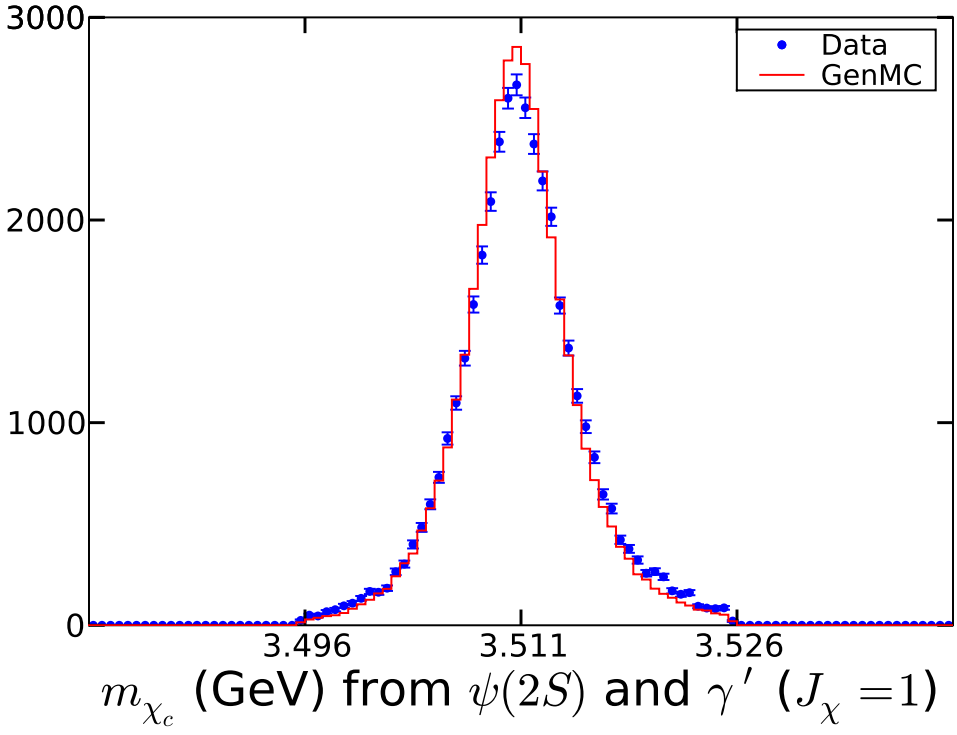

Figure 4.6: Plot of the χ_{c1} mass as calculated from subtracting the four vector of the γ' from the ψ' four-vector. This variable is not cut on, as the 1C and 4C kinematic fits ensure that this cut is identical to the χ_{c1} mass cut generated by adding the J/ψ and γ four-vectors.

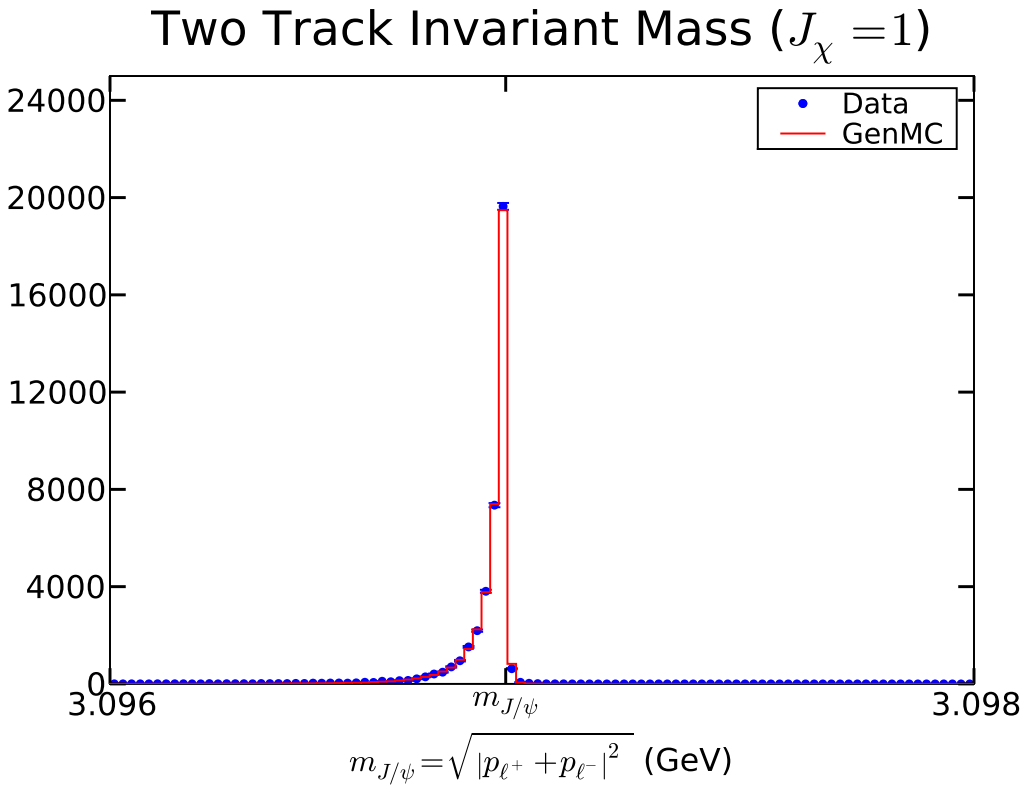

Figure 4.7: Plot of two track invariant mass, which should correspond to the J/ψ mass. There is no cut made on the two track invariant mass, as the 1C kinematic fit ensures that this is a cut on this variable would be satisfied. All the selection criteria described in the text are made on this plot.

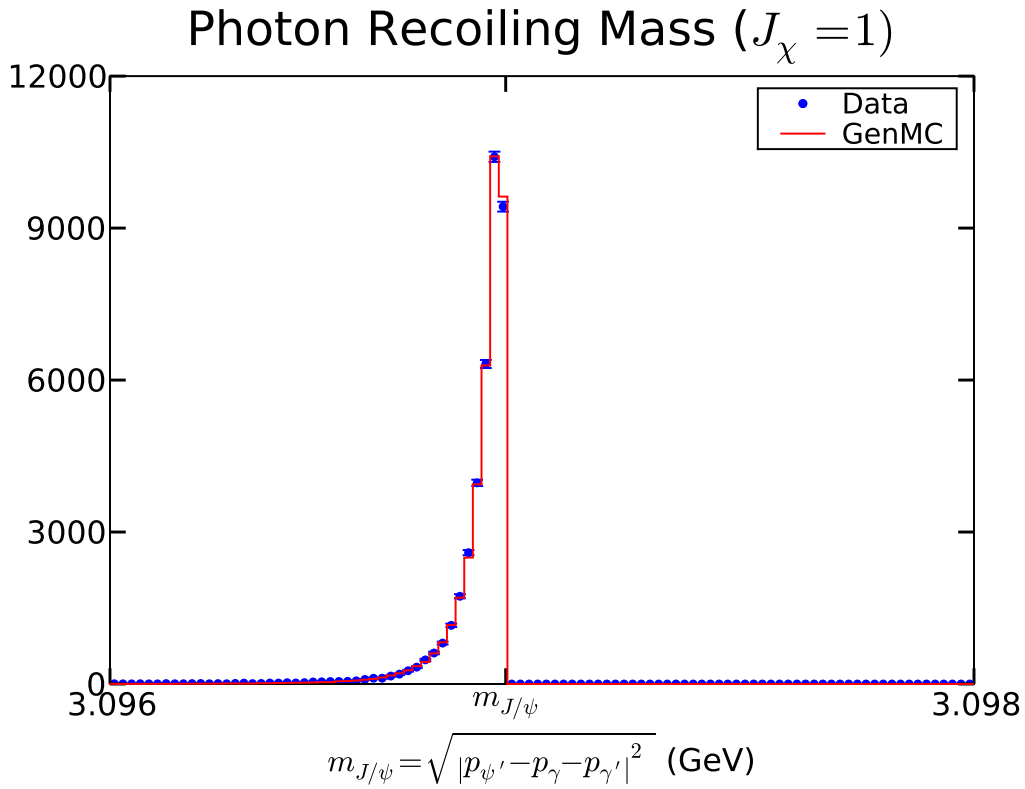

Figure 4.8: Plot of the photon recoiling mass, which should correspond to the J/ψ mass. There is no cut made on the photon recoiling mass, as the 1C and 4C kinematic fits should ensure that it is satisfied. All the other selection criteria described in the text are made.

4.1.7 $\psi' \to \gamma'\chi_{c2} \to \gamma'\gamma J/\psi$ transitions

The cuts for $J_\chi = 2$ transitions that are made are summarized here:

Reduced χ^2 Require all reduced χ^2 from kinematic fits to be less than 16 (including vertex fits).

E/p Require for $J/\psi \to \mu^+\mu^-$ that $(E/p)_{\text{larger}} < 0.5$ and $(E/p)_{\text{smaller}} < 0.25$, and for $J/\psi \to e^+e^-$ that $(E/p)_{\text{larger}} > 0.85$ and $(E/p)_{\text{smaller}} > 0.5$.

χ_c mass Require that the χ_c mass constructed from $m = \sqrt{|p_{J/\psi} + p_\gamma|^2}$ is within 0.15 GeV of the $m_{\chi_{c2}} = 3.556\,\text{GeV}$.

***J/ψ* momentum** Require that the J/ψ momentum is between $0.24\,\text{GeV}/c$ and $0.51\,\text{GeV}/c$.

Third Most Energetic Shower Require that the maximum energy of the third most energetic shower is less than 30 MeV.

GoodThingsProd Standard "GoodThings" cuts as described in section 4.1.1.

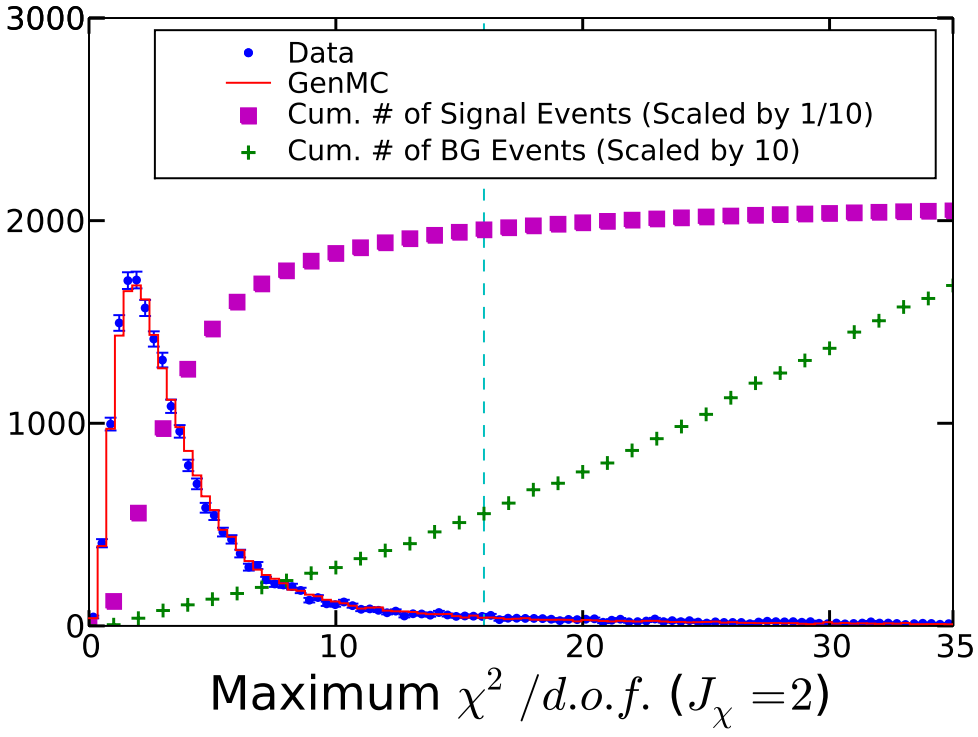

Figure 4.9: Plot of maximum reduced χ^2 in all kinematic fits (including vertex fits) in generic Monte Carlo and data. Events with a maximum reduced χ^2 below 16 (the dashed cyan line) are kept. Cumulative totals for the number of signal and impurity background events are also plotted for each potential value of a χ^2 cut.

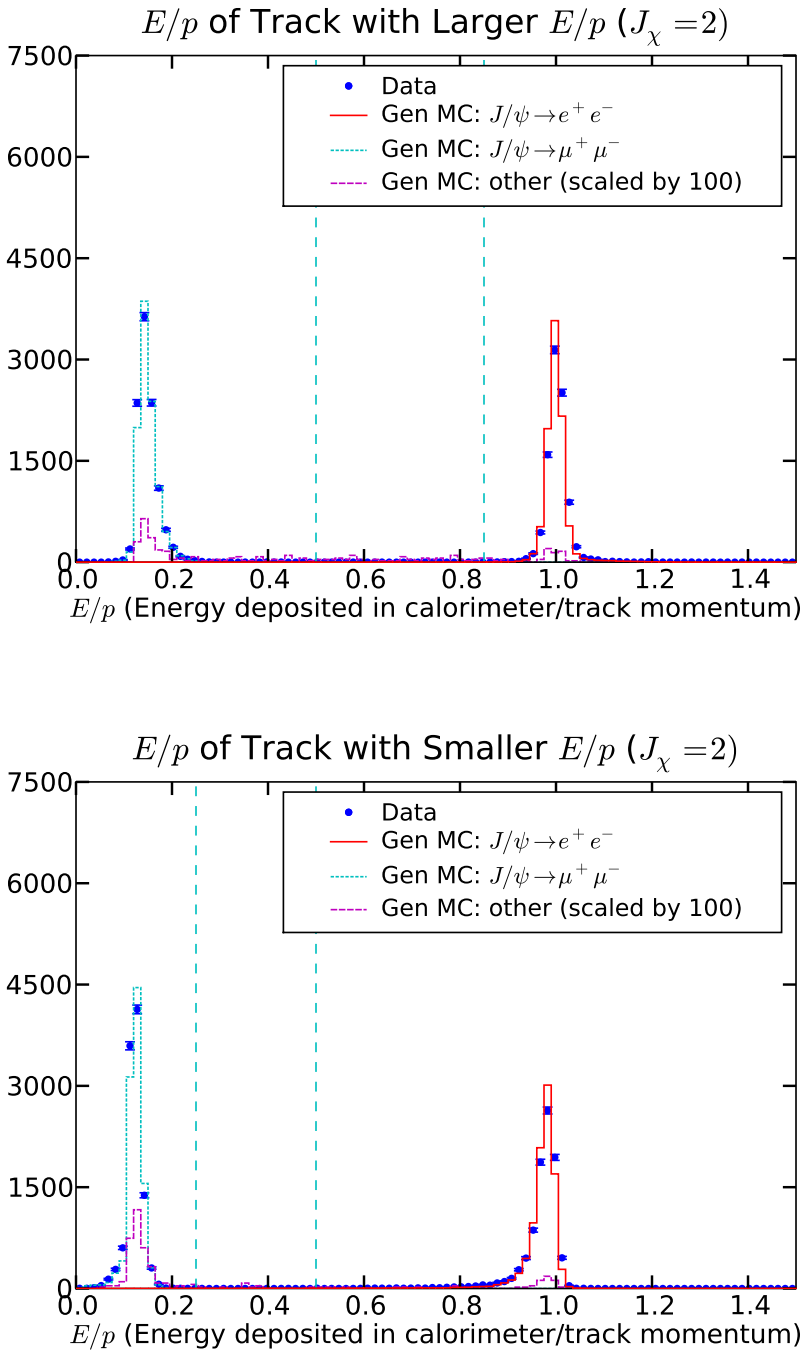

Figure 4.10: Plot of E/p, the ratio of the energy (GeV) deposited in the calorimeter to the track momentum (GeV/c) for both tracks. For each event, we histogram the E/p from the track with the larger and smaller ratio and apply different criteria. The purpose of these cuts is to separate events with $J/\psi \to \mu^+\mu^-$ and $J/\psi \to e^+e^-$, which are well differentiated with these cuts.

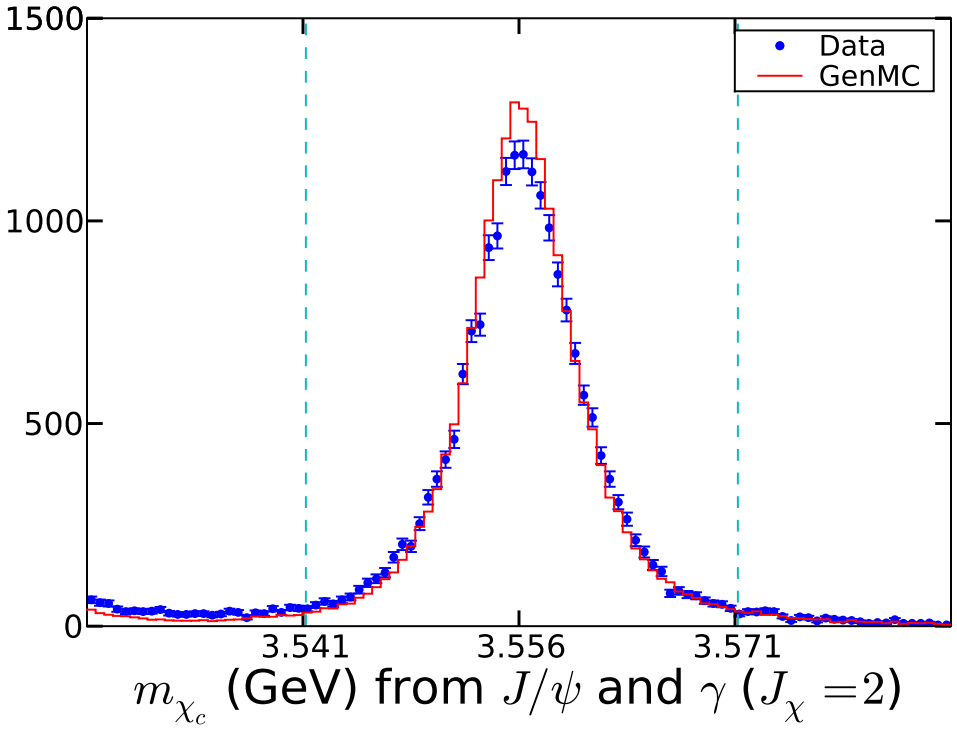

Figure 4.11: Plot of χ_c mass constructed by the four-vectors of γ and J/ψ. The kinematic fits ensure that this cut is redundant with the cut on the χ_c mass constructed by subtracting the γ' four-vector from the ψ' four-vector.

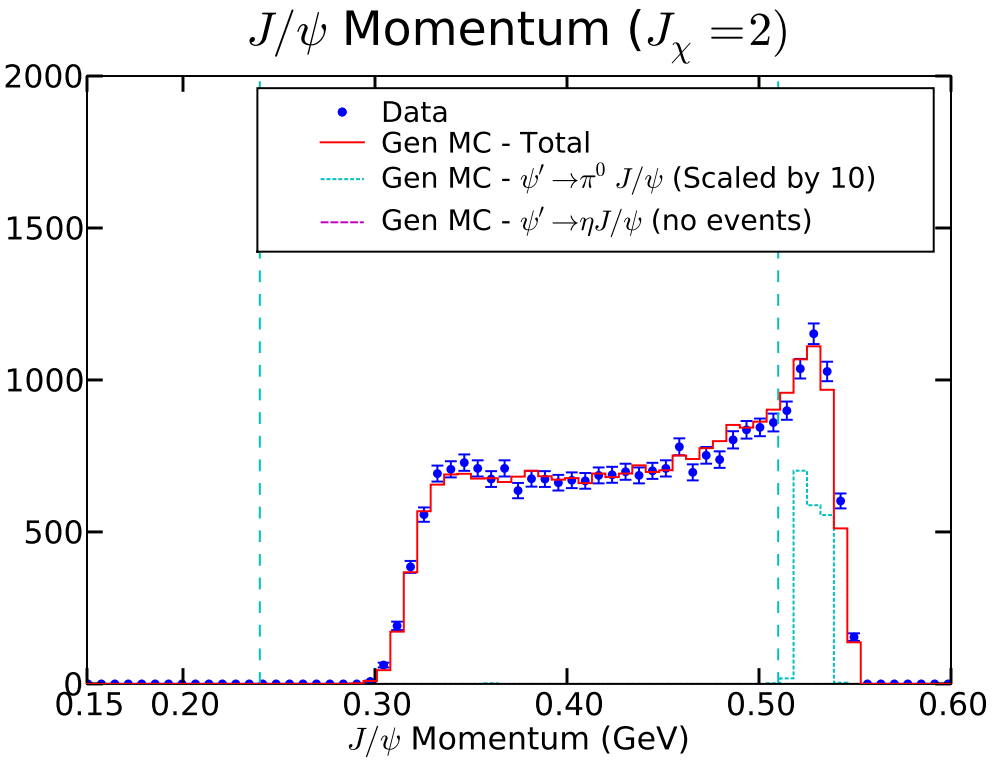

Figure 4.12: Plot of J/ψ momentum to indicate removal of the two background modes of $\psi' \to \pi^0 J/\psi$ ($p_{J/\psi} = 528\,\mathrm{MeV}/c$) and $\psi' \to \eta J/\psi$ ($p_{J/\psi} = 199\,\mathrm{MeV}/c$). The two background modes removed with the J/ψ momentum cut are scaled up by a factor of 10, so they are visible in comparison to the signal.

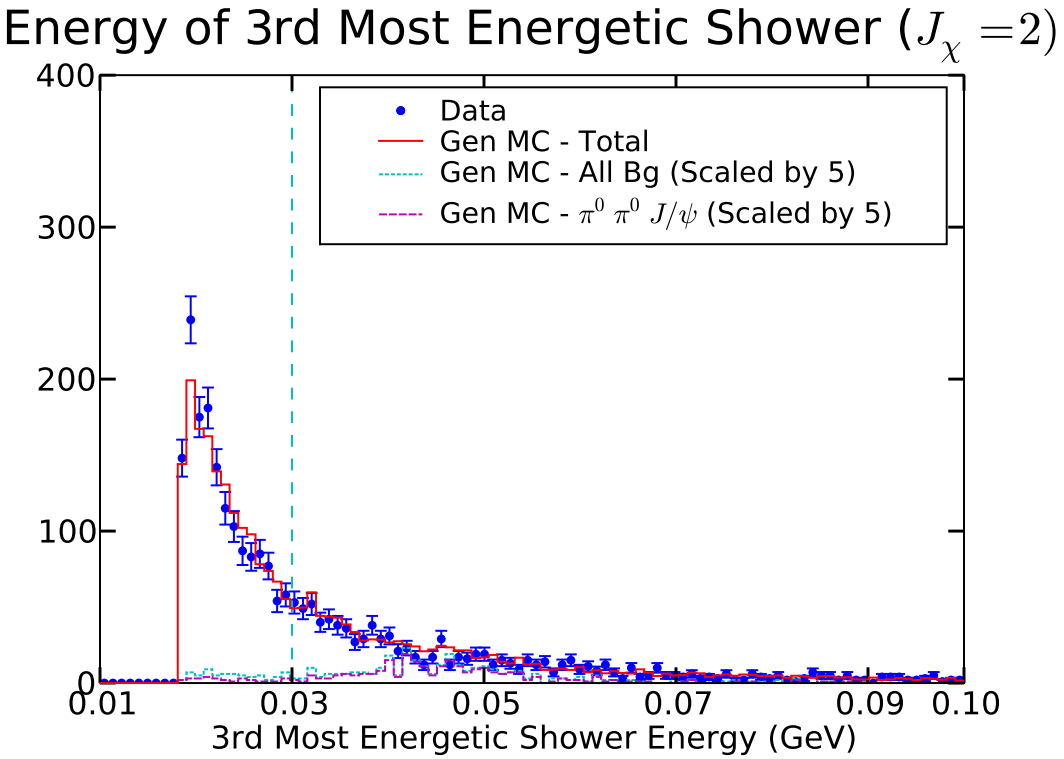

Figure 4.13: Plot of the Energy of the third most energetic shower. Note the 'GoodThingsProd' enforces that a 'Good' shower has an energy of greater than 18.4 MeV (1% of the beam energy). This creates many off-scale events with a shower energy of 0. In Generic MC (Data), 87.3%=95053/108844 (87.4% = 19165/21913) of events have a third shower energy of less than 18 MeV. In the five-times `data42` generic MC dataset with 120 million ψ' events, there are a total of 303 $\pi^0\pi^0 J/\psi$ background events of which 22 have $E_{\rm 3rdshwr} < 18\,{\rm MeV}$ and 52 have $E_{\rm 3rdshwr} < 30\,{\rm MeV}$ (the current cut value), while there were 95093 total events with $E_{\rm 3rdshwr} < 18\,{\rm MeV}$ and 103076 total events with $E_{\rm 3rdshwr} < 30\,{\rm MeV}$.

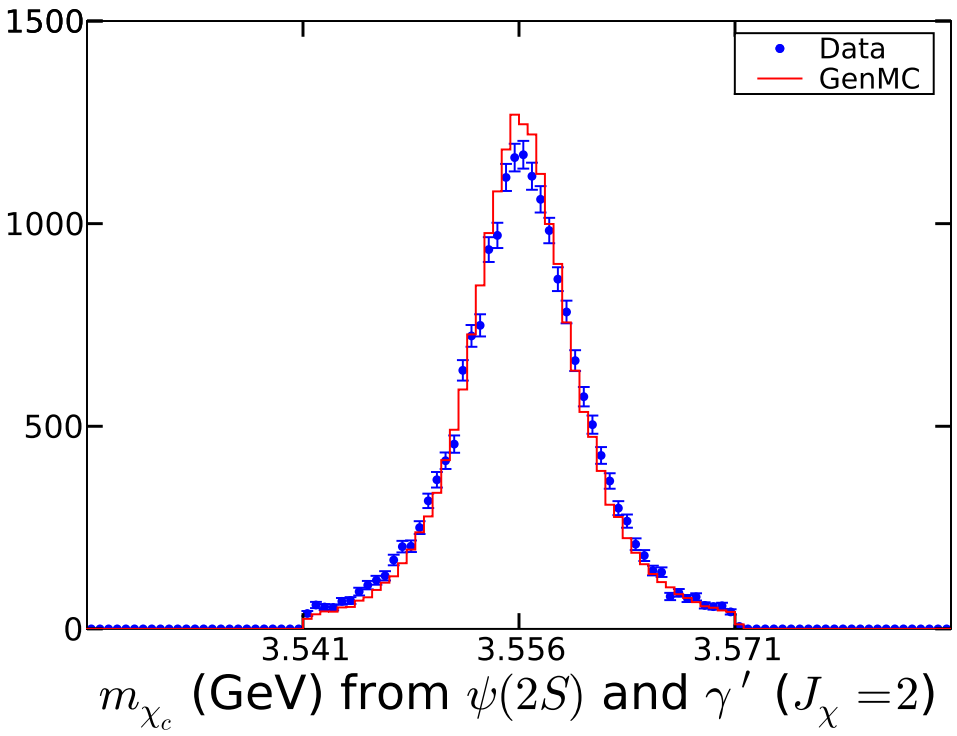

Figure 4.14: Plot of the χ_{c2} mass as calculated from subtracting the four vector of the γ' from the ψ' four-vector. This variable is not cut on as the 1C and 4C kinematic fits, ensure that this cut is identical to the χ_{c2} mass cut generated by adding the J/ψ and γ four-vectors.

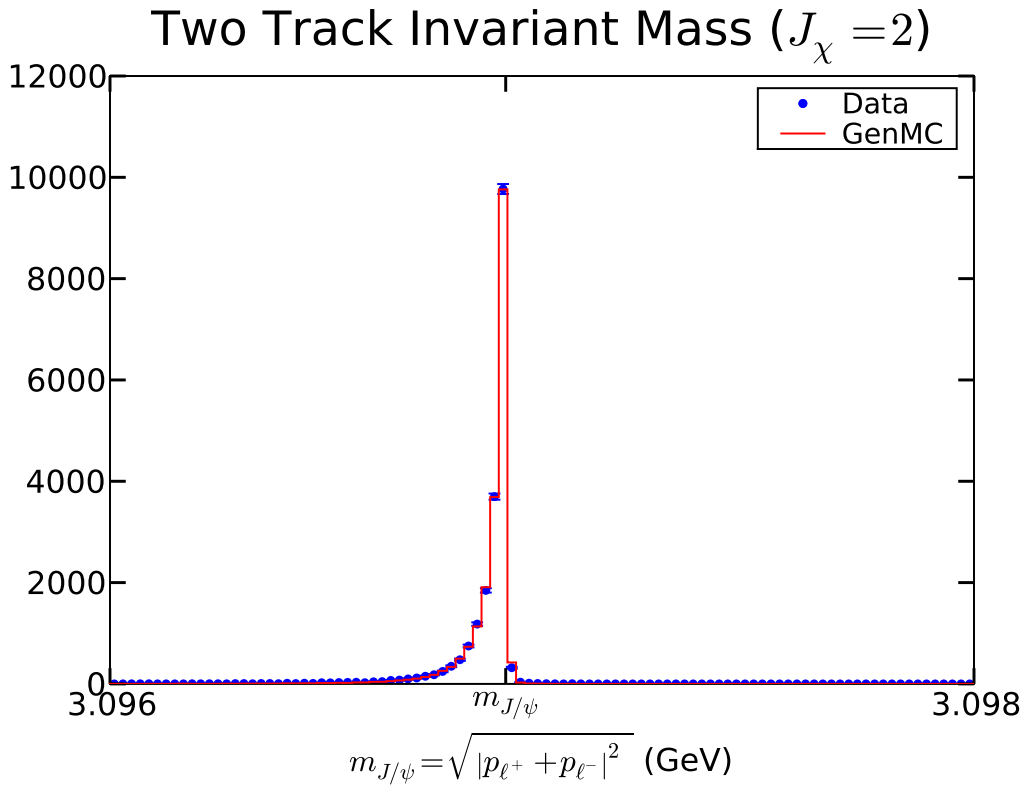

Figure 4.15: Plot of two track invariant mass, which should correspond to the J/ψ mass. There is no cut made on the two track invariant mass, as the 1C kinematic fit ensures that this is a cut on this variable would be satisfied. All the selection criteria described in the text are made on this plot.

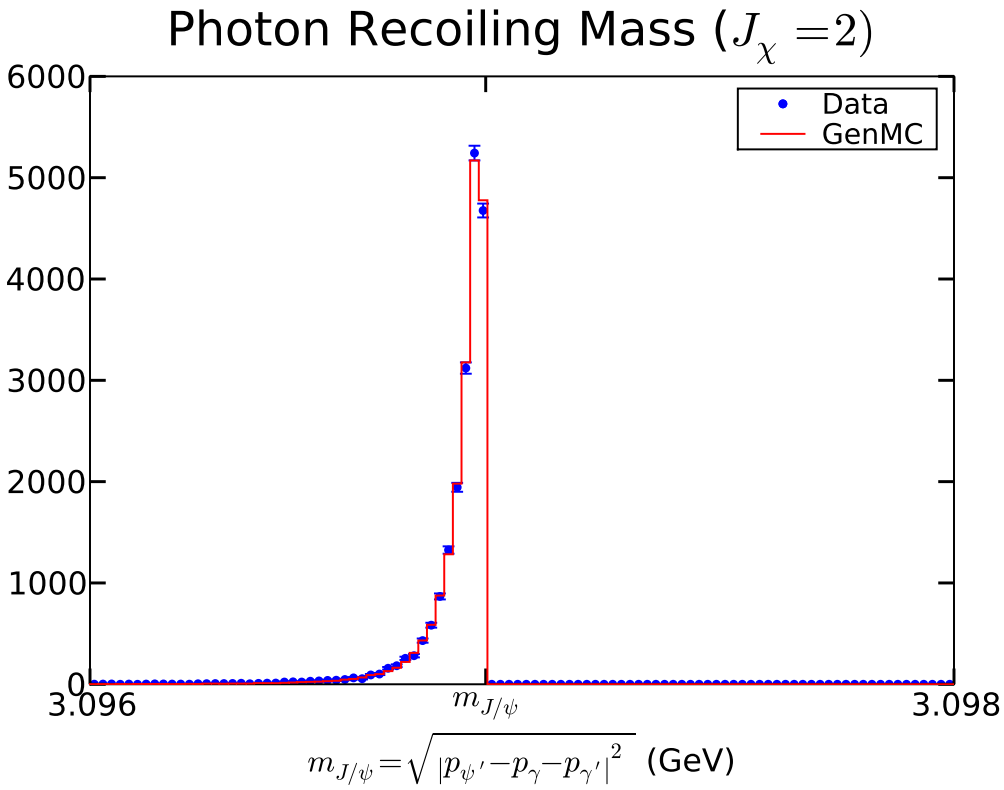

Figure 4.16: Plot of the photon recoiling mass, which should correspond to the J/ψ mass. There is no cut made on the photon recoiling mass, as the 1C and 4C kinematic fits should ensure that it is satisfied. All the other selection criteria described in the text are made.

4.2 Fitting Procedure

We find the multipole amplitudes by performing an unbinned maximum likelihood fit of the selected data events to the probability distribution function (PDF) $W(\Omega;\mathbb{A})$ given by Eq. (2.6). Events are selected according to the criteria described in section 4.1 and each event is described by a set of five angles $\Omega \equiv (\theta', \phi', \theta_{\gamma\gamma}, \theta, \phi)$ defined in Figure 2.1. The PDF $W(\Omega;\mathbb{A})$ gives the probability for an event with angles Ω to occur given a set of multipole amplitudes $\mathbb{A} \equiv (a_i, b_j)$. The PDF given in Eq. (2.6) is written in terms of helicity amplitudes, but can be written in terms of multipole amplitudes as $W(\Omega;\mathbb{A})$ using Eq. (2.8) for $J_\chi = 1$ and Eq. (2.9) for $J_\chi = 2$. The total likelihood for N_d data events to be described by $W(\Omega;\mathbb{A})$ is

$$\mathcal{L}_W(\mathbb{A}) \equiv \prod_{d=1}^{N_d} W(\Omega_d;\mathbb{A}). \tag{4.2}$$

If we had a uniform angular efficiency $\epsilon(\Omega)$ our task would simply be to find the value of the amplitudes $\mathbb{A}$ that maximizes the likelihood $\mathcal{L}_W(\mathbb{A})$. Equivalently, we could maximize the logarithm of the likelihood, $\log \mathcal{L}_W(\mathbb{A})$ as the logarithm is a monotonically increasing function. The multi-parameter optimization can be performed using a well known optimization routine, such as the variable metric algorithm incorporated in Minuit's `MIGRAD` optimizer [18]. However, the efficiency of event reconstruction is a function of the angles Ω due to both the design of the detector and selection criteria, so we must account for the angular detector efficiency.

The initially unknown angular detector efficiency $\epsilon(\Omega)$ describes the probability that an event occurring at the angles Ω will be detected by the detector and pass the selection criteria. We define a new normalized PDF to account for this detector

efficiency $\epsilon(\Omega)$

$$F(\Omega;\mathbb{A}) \equiv \frac{\epsilon(\Omega)W(\Omega;\mathbb{A})}{\int \epsilon(\Omega')W(\Omega';\mathbb{A})d\Omega'} \tag{4.3}$$

and note that the original PDF $W(\Omega;\mathbb{A})$ is of the form

$$W(\Omega;\mathbb{A}) = \sum_{ijkl} a_i a_j b_k b_l G_{ijkl}(\Omega). \tag{4.4}$$

The functions $G_{ijkl}(\Omega)$ are obtained from the expression for $W(\Omega;\mathbb{A})$, so this form allows separation of the parameters being fit for (the multipole amplitudes $\mathbb{A}$) and the data points (the angles Ω). This allows us to write the denominator of the PDF in Eq. (4.3) as

$$\begin{aligned}
\int \epsilon(\Omega')W(\Omega';\mathbb{A})d\Omega' &= \int \epsilon(\Omega') \sum_{ijkl} a_i a_j b_k b_l G_{ijkl}(\Omega')d\Omega' \\
&= \sum_{ijkl} a_i a_j b_k b_l \int \epsilon(\Omega')G_{ijkl}(\Omega')d\Omega' \\
&= \sum_{ijkl} a_i a_j b_k b_l I_{ijkl}
\end{aligned}$$

where the efficiency-dependent integrals $I_{ijkl} \equiv \int \epsilon(\Omega')G_{ijkl}(\Omega')d\Omega'$ are independent of the fitting parameters $\mathbb{A}$. The integrals I_{ijkl} can be approximated by a Monte Carlo numerical integration technique. Using a large sample of phase space Monte Carlo (section 3.4.3) that is generated uniformly in the five variables $(\cos\theta', \phi', \cos\theta_{\gamma\gamma'}, \cos\theta, \phi)$, we record whether each phase space MC event is reconstructed and passes the selection criteria. Using the known angular functions $G_{ijkl}(\Omega)$, we approximate the integral I_{ijkl} as

$$\begin{aligned}
I_{ijkl} &\equiv \int \epsilon(\Omega')G_{ijkl}(\Omega')d\Omega' \\
&\cong \frac{1}{N_{\text{phsp}}} \sum_{p=1}^{N_{\text{phsp}}} \Theta(p)G_{ijkl}(\Omega_p)
\end{aligned} \tag{4.5}$$

where $\Theta(p)$ is 1 (0) if the pth phase space event is (not) reconstructed and N_{phsp} is the total number of phase space events.

To find the most likely form of the parameters $\mathbb{A}$ given the PDF $F(\Omega;\mathbb{A})$, we find the values of the parameters $\mathbb{A}$ that maximize the logarithm of the likelihood, which is given by Eq. (4.2) with the PDF F instead of W. The logarithm of the likelihood that the parameters $\mathbb{A}$ in the PDF $F(\Omega;\mathbb{A})$ describe the N_d data events occurring at angles Ω_d is

$$\begin{aligned}\log\mathcal{L}(\mathbb{A}) &\equiv \log\prod_{d=1}^{N_d} F(\Omega_d;\mathbb{A}) = \sum_{d}^{N_d}\log F(\Omega_d;\mathbb{A}) \\ &= \sum_{d}^{N_d}\left[\log\epsilon(\Omega_d) + \log W(\Omega_d;\mathbb{A}) - \log a_i a_j b_k b_l I_{ijkl}\right]. \qquad (4.6)\end{aligned}$$

As the term $\log\epsilon(\Omega_d)$ is independent of the parameters $\mathbb{A}$, it can be removed from $\log\mathcal{L}(\mathbb{A})$ when finding the parameters that maximize $\log\mathcal{L}(\mathbb{A})$. The likelihood we maximize is

$$\log\mathcal{L}'(\mathbb{A}) = \left[\sum_{d}^{N_d}\log W(\Omega_d;\mathbb{A})\right] - N_d\log a_i a_j b_k b_l I_{ijkl}. \qquad (4.7)$$

which has a dependence on the angular detector efficiency $\epsilon(\Omega)$ only in terms of the integrals I_{ijkl}. As these integrals can be approximated using Eq. (4.5) with phase space Monte Carlo, we do not need to explicitly find the form of the angular efficiency to perform an unbinned likelihood fit. This method of performing an unbinned maximum likelihood over an angularly varying detector efficiency was first developed in Ref. [13] by a former CLEO graduate student, Bob Perchonok.

When performing a $J_\chi=1$ ($J_\chi=2$) fit, we do not fit for the four (six) multipole amplitudes $a_1, b_1, a_2, b_2(, a_3, b_3)$ as all of the amplitudes are not independent. From the normalized definition of the multipole amplitudes given by Eqs. (2.15-2.18), we know that $1 = a_1^2 + a_2^2 + a_3^2 = b_1^2 + b_2^2 + b_3^2$. We can eliminate the two dependent parameters by instead fitting for $\alpha_2 \equiv a_2/a_1$, $\beta_2 \equiv b_2/b_1$, $\alpha_3 \equiv a_3/a_1$, $\beta_3 \equiv b_3/b_1$. We divide the unnormalized PDF $W(\Omega;\mathbb{A})$ by the constant $a_1 a_1 b_1 b_1$ eliminating the two non-independent parameters. This division is effectively done by substituting

1 for both a_1 and b_1, and substituting $\alpha_2, \alpha_3, \beta_2, \beta_3$ for a_2, a_3, b_2, b_3 respectively in the expressions for $W(\Omega; \mathbb{A})$. We recover the physical values for $a_1, a_2, a_3, b_1, b_2, b_3$ by noting that for the transition $\chi_{cJ} \to \gamma J/\psi$

$$a_1 \equiv \frac{\mathrm{E1}}{\sqrt{\mathrm{E1}^2 + \mathrm{M2}^2 + \mathrm{E3}^2}} = \frac{1}{\sqrt{1 + \alpha_2^2 + \alpha_3^2}} \tag{4.8}$$

$$a_2 \equiv \frac{\mathrm{M2}}{\sqrt{\mathrm{E1}^2 + \mathrm{M2}^2 + \mathrm{E3}^2}} = \frac{\alpha_2}{\sqrt{1 + \alpha_2^2 + \alpha_3^2}} \tag{4.9}$$

$$a_3 \equiv \frac{\mathrm{E3}}{\sqrt{\mathrm{E1}^2 + \mathrm{M2}^2 + \mathrm{E3}^2}} = \frac{\alpha_3}{\sqrt{1 + \alpha_2^2 + \alpha_3^2}}. \tag{4.10}$$

with identical relationships between b_1, b_2, b_3 and β_2, β_3 for the transition $\psi' \to \gamma' \chi_{cJ}$.

The multi-dimensional optimization of $\log \mathcal{L}'(\mathbb{A})$ was achieved using a python implementation[1] of the Minuit package[2]. The `MIGRAD` fitting routine was used that is a variable-metric algorithm with an inexact line search[3].

4.3 Statistical Results of Five-Angle Fits

4.3.1 $J_\chi = 1$ Fits

The result of the two-parameter fit to the $J=1$ data are $a_2^{J=1} = -0.0611 \pm 0.0063$, $b_2^{J=1} = 0.0281 \pm 0.0073$ with 39363 events from `data42`. The efficiency integrals in the denominator were calculated by simulating 4.5 million phase space MC events through the detector and selection criteria, where 39.6% were reconstructed. The log likelihood plot is shown in Figure 4.17 with contour curves showing that the

[1] http://code.google.com/p/pyminuit/
[2] http://lcgapp.cern.ch/project/cls/work-packages/mathlibs/minuit/index.html
[3] http://seal.cern.ch/documents/minuit/mnusersguide.pdf

difference in likelihood between the fitted value and a pure E1 transition ($a_2 = b_2 = 0$) is 11.1σ.

The data in the five angles is plotted in Figures 4.18 and 4.19 with projections from a pure E1 distribution and the fitted M2/E1 admixture. The angle $\cos\theta$ (Figure 4.18) is of particular note as it is the angle that most distinguishes the data from being pure E1 to being an M2/E1 admixture. The other projections (Figure 4.19) are mostly included for completeness, though the fitted projection for $\cos\theta'$ also shows slightly better agreement with data than the pure E1 projection. Comparing the 50 bin histograms in $\cos\theta$, we see that the reduced chi square ($\chi^2/N_{\text{d.o.f.}}$) comparing the data with the projection at the fitted values is $43.6/47 = 0.93$, while data and the pure E1 projection have a $\chi^2/N_{\text{d.o.f.}}$ of $100.6/49 = 2.05$ [4].

Using the parity transformations described in Eqs. (2.10 - 2.14), we are able to fold four of the five angles into the positive domain without modifying the value of the likelihood calculated through the $W(\Omega;\mathbb{A})$. In Figures 4.20 and 4.21, we apply these parity transformations to the data to highlight how the data are well matched with the projection (specifically in $\cos\theta$) with the fitted values of $\mathbb{A}$, while the data have a significantly poorer match to the pure E1 value.

If we fix the ratio of the parameters to the theoretical ratio, given by Eq. (2.21), $a_2^{J=1}/b_2^{J=1} = -2.274$, we can perform a one-parameter fit to the five-angle $J = 1$ dataset. The result of this one-parameter fit is $a_2^{J=1} = -0.0615 \pm 0.0055$, $b_2^{J=1} = -a_2^{J=1}/2.274 = 0.0271 \pm 0.0024$ which is 11.1σ from the pure E1 value, nearly identical to the results of the two-parameter fit.

[4]The number of degrees of freedom $N_{\text{d.o.f.}} = N_{\text{bins}} - N_{\text{params}} - 1$ where N_{bins} is the number of bins in the histogram, N_{params} is the number of parameters we are fitting for. The minus one accounts for the fact that the projections are normalized to contain the same number of events as the original dataset.

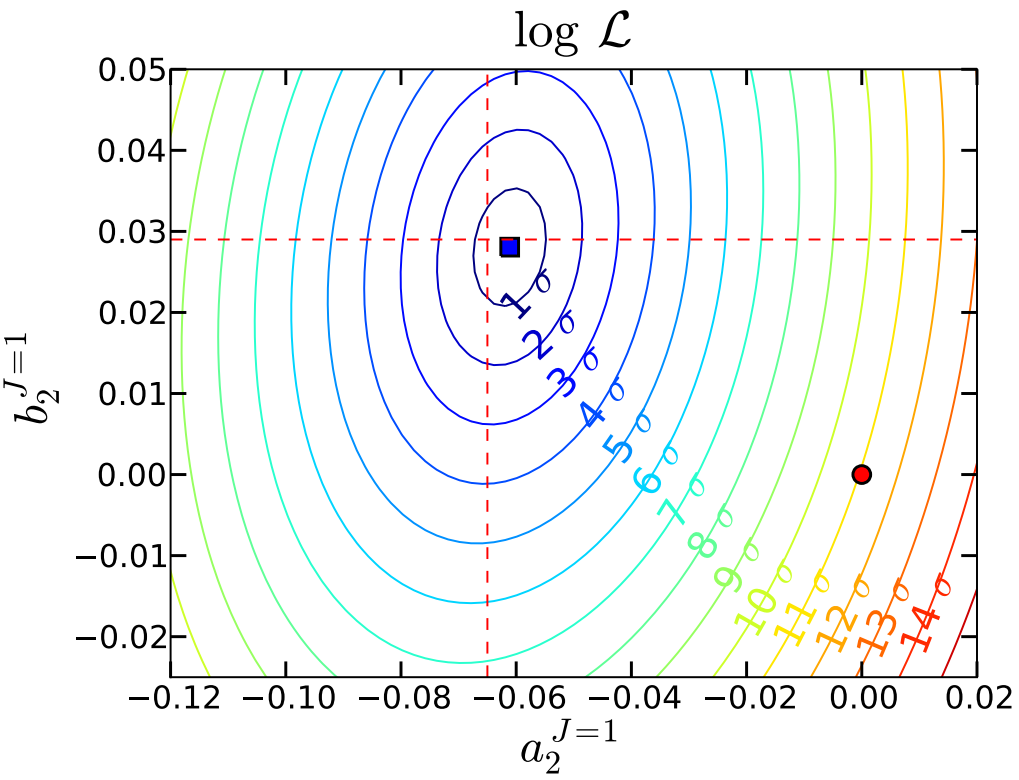

Figure 4.17: $J_\chi = 1$ log likelihood contour plot. The fitted value (■) is from the two-parameter fit with $(a_2, b_2) = (-0.0611, 0.0281)$ and is 11.1σ from pure E1 (●). The first-order theory value with $\kappa_c = 0$ is $(a_2, b_2) = (-0.065, 0.029)$ and is indicated by the red dashed line.

Table 4.2: $J = 1$ five-angle fit results. The fits were performed on the 39363 events from `data42` selected with the selection criteria described in section 4.1. The full 4.5M event phase space data sample was used for the efficiency integrals. The difference in the log likelihood between the fitted distribution and a pure E1 distribution corresponds to $\chi_{\rm E1} \equiv \sqrt{2\Delta \log \mathcal{L}} = 11.07\sigma$.

fit	$a_2^{J=2}$ 10^{-2}	σ_{a_2} 10^{-2}	$b_2^{J=2}$ 10^{-2}	σ_{b_2} 10^{-2}	$\chi_{\rm E1}$
Two-parameter (five-angle)	-6.11	0.63	2.81	0.73	11.07
One-parameter ($a_2/b_2 = -2.274$)	-6.15	0.55	2.71	0.24	11.07
Theory ($m_c = 1.5\,\text{GeV}$)	$-6.5(1+\kappa_c)$		$2.9(1+\kappa_c)$		

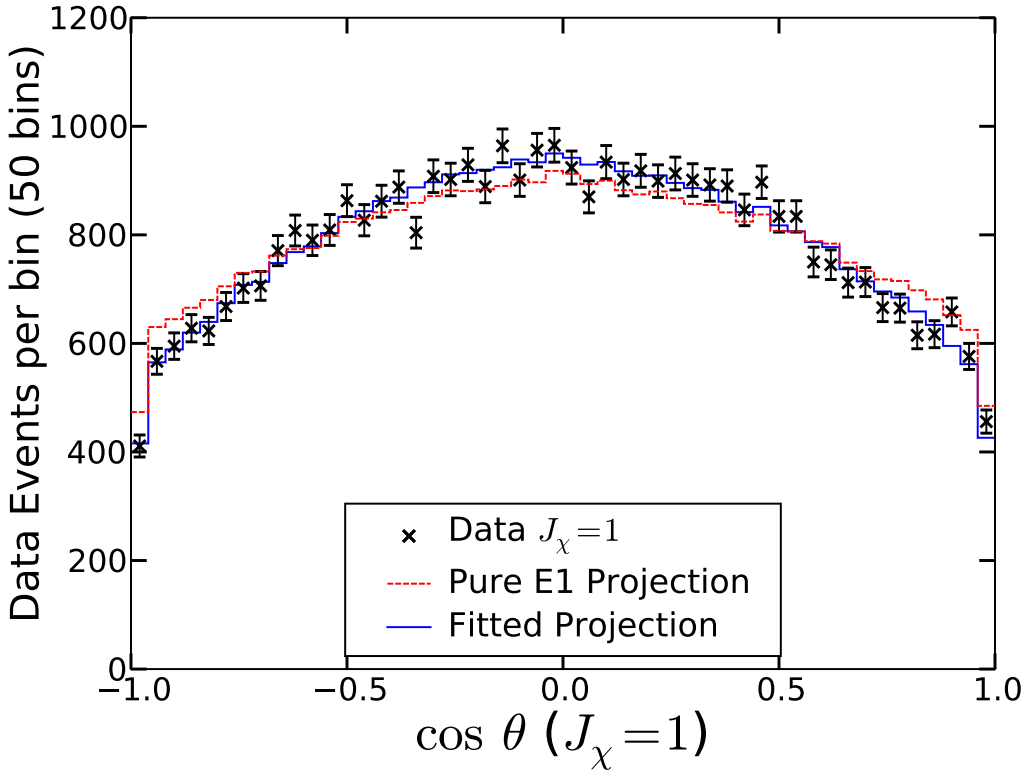

Figure 4.18: $J_\chi = 1$ projection of $\cos\theta$. The $\chi^2/N_{\text{d.o.f.}}$ for the 50 bin histogram describing the data to correspond with the fitted projection and the pure E1 projection are $42.7/47 = 0.91$ and $100.8/49 = 2.21$, respectively. The five-parameter fit finds a fitted value of $(a_2, b_2) = (-0.0611, 0.0281)$, which is 11.1σ from the pure E1 value.

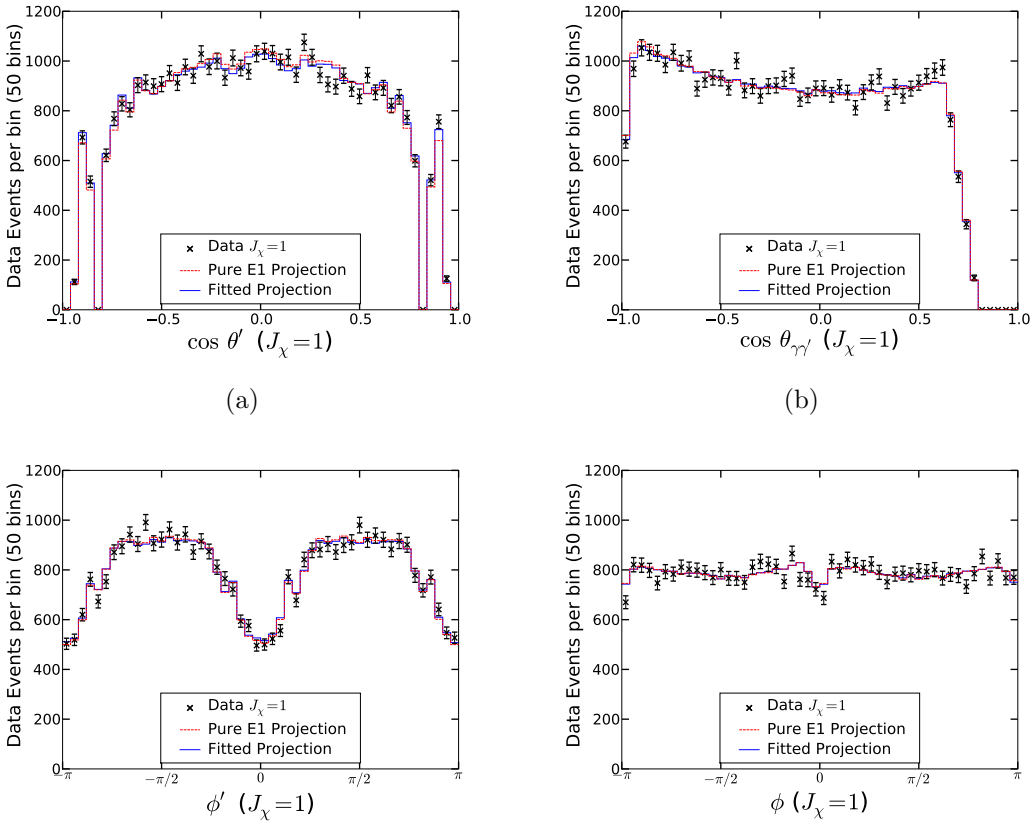

(a) (b) (c) (d)

Figure 4.19: $J_\chi = 1$ projections for $\cos\theta', \cos\theta_{\gamma\gamma'}, \phi', \phi$. The $\chi^2/N_{\text{d.o.f.}}$ comparing the 50 bin histogram of the data to the fitted projection are $58.4/47 = 1.24$, $49.1/47 = 1.05$, $54.7/47 = 1.16$, and $57.0/47 = 1.21$, while the reduced χ^2 comparing data to the pure E1 projection are $78.0/49 = 1.59$, $54.9/49 = 1.11$, $53.2/49 = 1.09$, and $58.9/49 = 1.20$ for $\cos\theta', \cos\theta_{\gamma\gamma'}, \phi'$, and ϕ, respectively. The fitted projection corresponds to the two-parameter fit with $(a_2, b_2) = (-0.0611, 0.0281)$, which is 11.1σ from the pure E1 value.

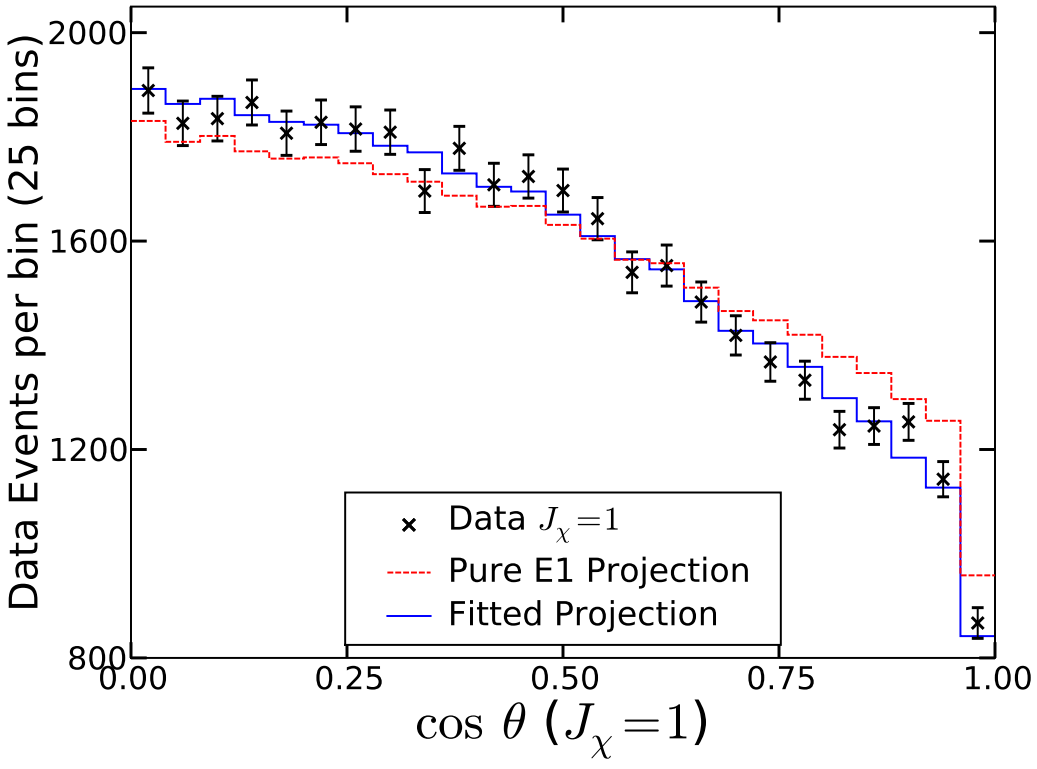

Figure 4.20: $J_\chi = 1$ projection of $\cos\theta$ after using parity transformations to fold dataset into positive $\cos\theta', \phi', \cos\theta_{\gamma\gamma'}, \cos\theta$. The $\chi^2/N_{\text{d.o.f.}}$ for the 25 bin histogram describing the data to correspond with the fitted projection and the pure E1 projection are $16.2/22 = 0.74$ and $80.3/24 = 3.35$, respectively. The fitted projection corresponds to the two-parameter fit with $(a_2, b_2) = (-0.0611, 0.0281)$, which is 11.1σ from the pure E1 value.

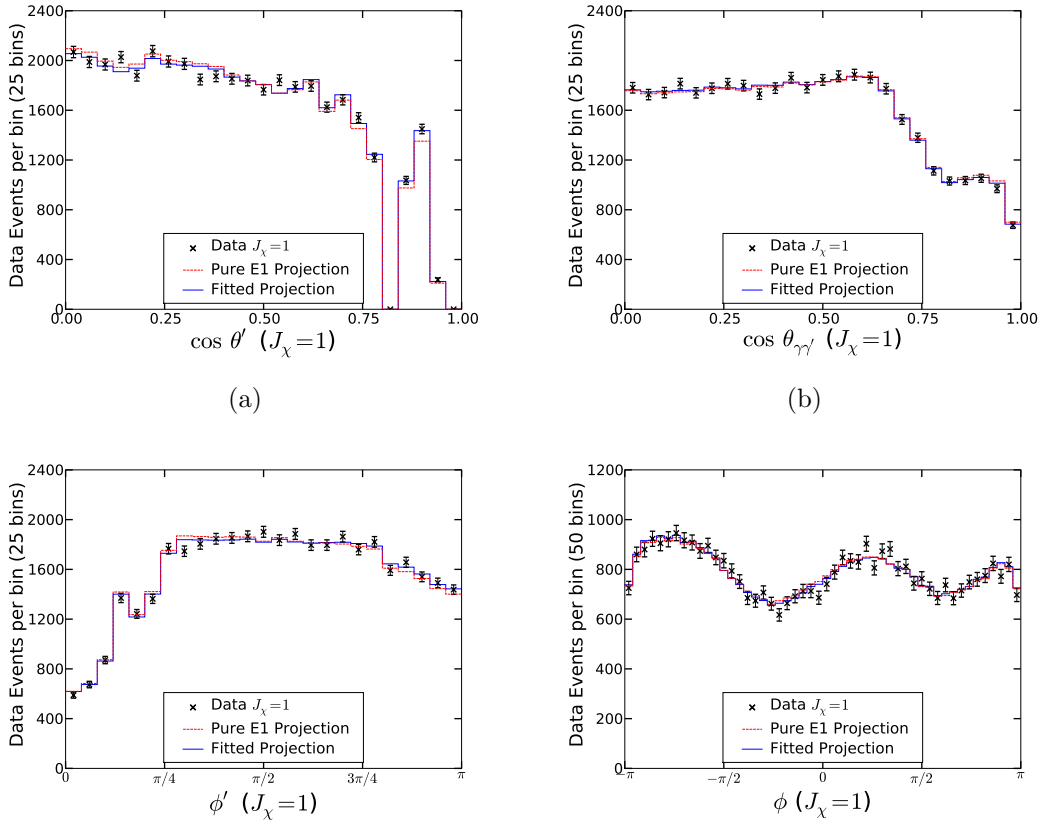

Figure 4.21: $J_\chi = 1$ projections for $\cos\theta', \cos\theta_{\gamma\gamma'}, \phi', \phi$ after using parity transformation to fold the dataset into positive $\cos\theta', \phi', \cos\theta_{\gamma\gamma'}, \cos\theta$. The reduced χ^2 comparing the 25 bin (50 bins for ϕ) histogram of the data to the fitted projection are $30.4/22 = 1.38$, $11.5/22 = 0.52$, $23.9/22 = 1.09$, and $42.5/47 = 0.90$, while the $\chi^2/N_{\text{d.o.f.}}$ comparing data to the pure E1 projection are $50.4/24 = 2.10$, $16.0/24 = 0.67$, $30.9/24 = 1.29$, and $45.0/49 = 0.92$ for $\cos\theta', \cos\theta_{\gamma\gamma'}, \phi'$, and ϕ, respectively. The fitted projection corresponds to the two-parameter fit with $(a_2, b_2) = (-0.0611, 0.0281)$, which is 11.1σ from the pure E1 value.

4.3.2 $J_\chi = 2$ Fits

As the $J_\chi = 2$ PDF is parametrized by four multipole amplitudes (a_2, b_2, a_3, b_3), there are several choices for types of fits to be performed. The simplest would be a two-parameter fit where we set $a_3 = b_3 = 0$ as the E3 amplitudes should be zero in the absence of significant S-D state mixing. For this type of fit of the 19755 events selected from `data42`, we find $a_2^{J=2} = -0.093 \pm 0.015$, $b_2^{J=2} = 0.010 \pm 0.012$ which is 6.2σ from the pure E1 fit.

Allowing for S-D mixing in the ψ' state, the $b_3^{J=2}$ amplitude may be non-zero. If we perform a three-parameter fit (setting $a_3^{J=2} = 0$), we find $a_2^{J=2} = -0.093 \pm 0.016$, $b_2^{J=2} = 0.007 \pm 0.014$, $b_3^{J=2} = -0.008 \pm 0.012$ which is 6.3σ from the pure E1 fit.

If we allow a non-zero $b_3^{J=2}$ amplitude, but fix the ratio of $a_2^{J=2}/b_2^{J=2} = -3.367$ by Eq. (2.23), we can perform a two-parameter fit that allows for S-D mixing in the ψ' state. The results of this two-parameter fit are $a_2^{J=2} = -0.092 \pm 0.016$, $b_2^{J=2} = -a_2^{J=2}/3.367 = 0.0274 \pm 0.005$, $b_3^{J=2} = -0.001 \pm 0.011$ which is 6.1σ from the pure E1 fit.

If we perform the fit for the full four parameters (a_2, b_2, a_3, b_3), we find $a_2^{J=2} = -0.079 \pm 0.019$, $b_2^{J=2} = 0.002 \pm 0.015$, $a_3^{J=2} = 0.017 \pm 0.014$, $b_3^{J=2} = -0.008 \pm 0.012$ which is 6.4σ from the pure E1 fit. This fit differs somewhat from our theoretical expectations as we expect $a_3 \approx 0$ and $b_2^{J=2} \approx 0.029$; however, due to large statistical uncertainties both of these are less than 2σ effects.

For the five-angle fit with two parameters, we plot the data with the pure E1 projection and the fitted value projections in Figures 4.22 and 4.23. The projections for the other $J_\chi = 2$ five-angle fits are similar and shown in the appendices. Figures 4.24 and 4.25 show the projections after folding four of the five variables

into the positive domain using the parity transformations given in Eqs. (2.10 - 2.14). Note that while the histograms for $\cos\theta', \cos\theta_{\gamma\gamma'}$, and $\cos\theta$ are equivalent to histogramming $|\cos\theta'|, |\cos\theta_{\gamma\gamma'}|$, and $|\cos\theta|$ from the unfolded distribution, the histograms for ϕ' and ϕ are not simply related to the histograms of the unfolded distribution. This is because some parity transformations alter the phase angles by adding or subtracting the angle from π.

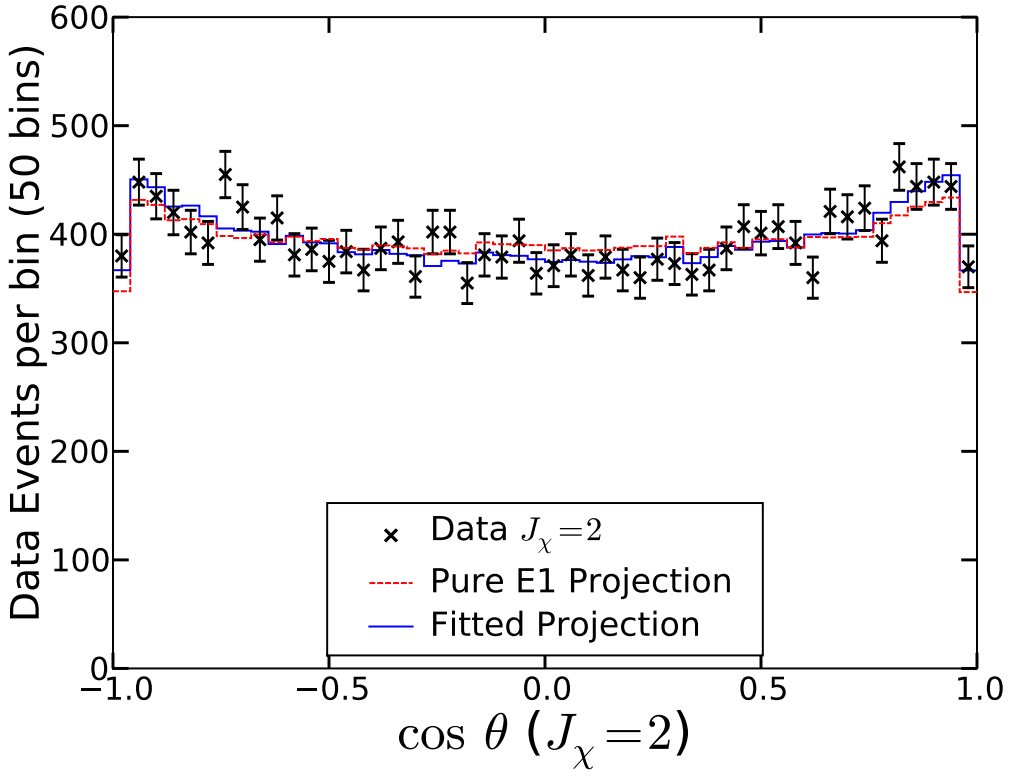

Figure 4.22: $J_\chi = 2$ data vs projections for $\cos\theta$. The reduced chi square ($\chi^2/N_{\text{d.o.f.}}$) for the 50 bin histogram of the data to come from the same distribution as the fitted projection (holding $a_3 \equiv b_3 \equiv 0$) is $37.3/47 = 0.79$, and the reduced chi square for data to come from pure E1 is $53.1/49 = 1.08$. The fitted projection corresponds to the two-parameter fit with $(a_2, b_2) = (-0.093, 0.010)$ with $a_3 \equiv b_3 \equiv 0$, which is 6.2σ from the pure E1 value.

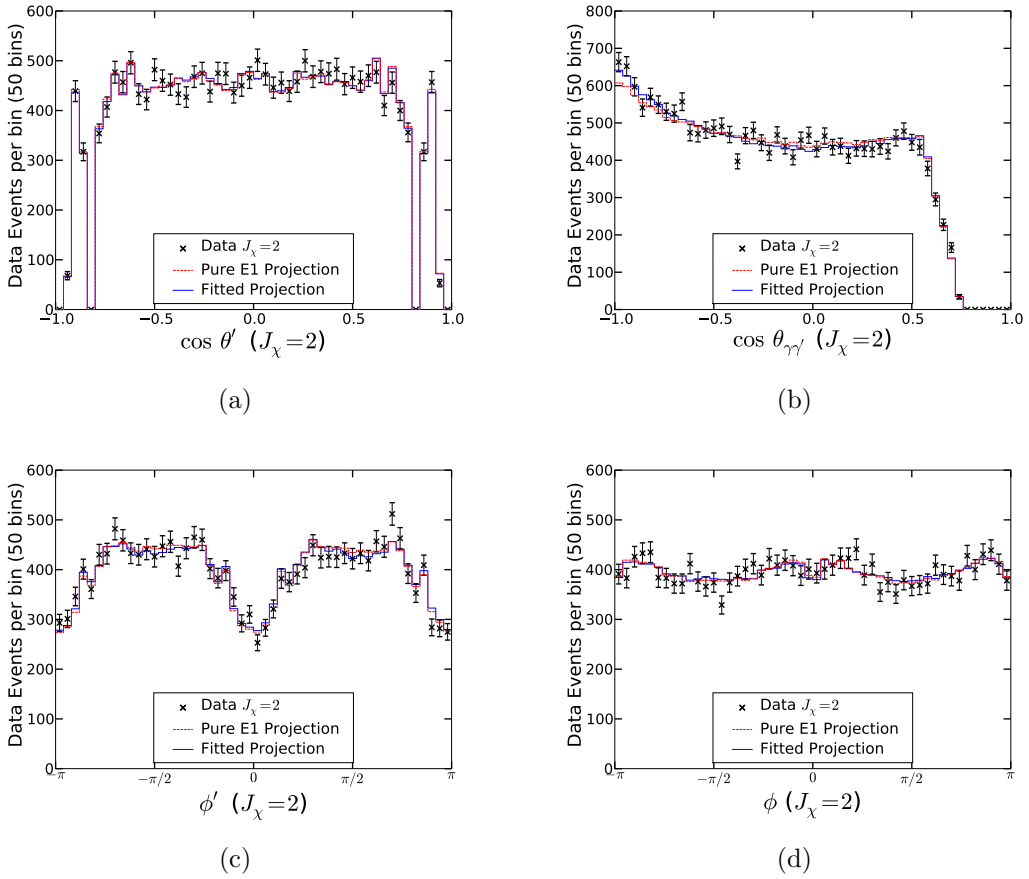

Figure 4.23: $J_\chi = 2$ data vs projections for $\cos\theta', \cos\theta_{\gamma\gamma'}, \phi', \phi$ with the two-parameter fit. The reduced χ^2 comparing the 50 bin histogram of the data to the fitted projection are $36.4/47 = 0.77$, $50.2/47 = 1.07$, $47.5/47 = 1.01$, and $45.9/47 = 0.98$, while the $\chi^2/N_{\text{d.o.f.}}$ comparing data to the pure E1 projection are $38.9/49 = 0.79$, $59.8/49 = 1.22$, $50.6/49 = 1.03$, and $45.0/49 = 0.92$ for $\cos\theta', \cos\theta_{\gamma\gamma'}, \phi'$, and ϕ, respectively. The fitted projection corresponds to the two-parameter fit with $(a_2, b_2) = (-0.093, 0.010)$ with $a_3 \equiv b_3 \equiv 0$, which is 6.2σ from the pure E1 value.

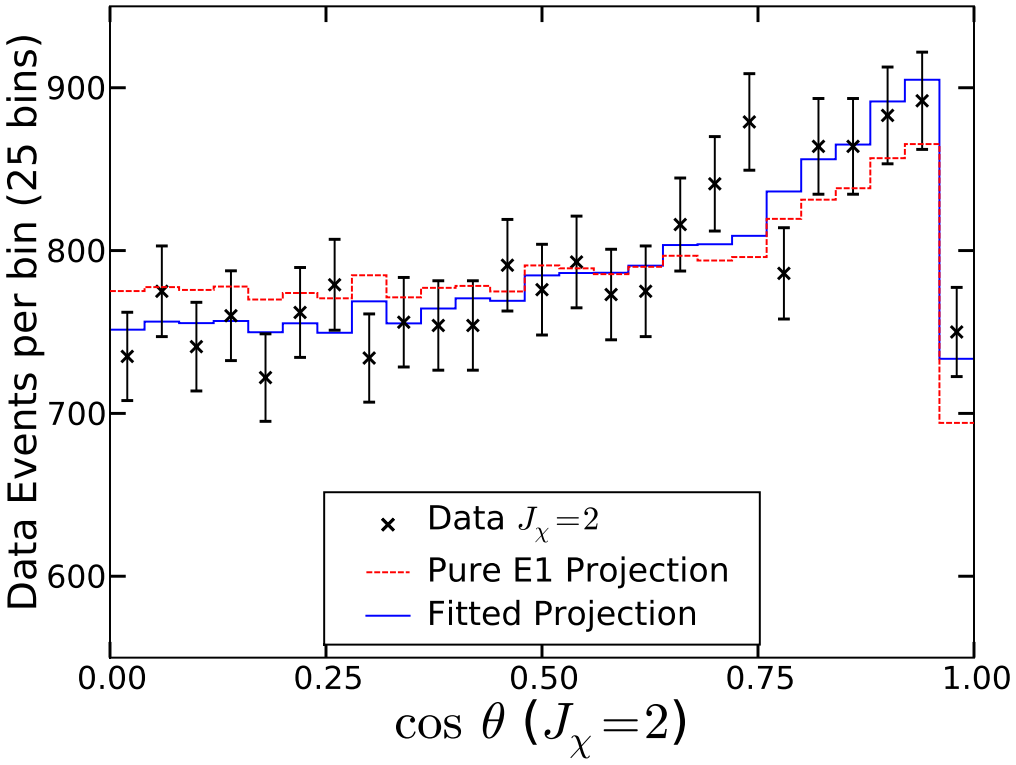

Figure 4.24: $J_\chi = 2$ projection of $\cos\theta$ after using parity transformations to fold dataset into positive $\cos\theta', \phi', \cos\theta_{\gamma\gamma'}, \cos\theta$. The $\chi^2/N_{\text{d.o.f.}}$ for the 25 bin histogram describing the data to correspond with the fitted projection and the pure E1 projection are $20.3/22 = 0.92$ and $35.5/24 = 1.48$, respectively. The fitted projection corresponds to the two-parameter fit with $(a_2, b_2) = (-0.093, 0.010)$ with $a_3 \equiv b_3 \equiv 0$, which is 6.2σ from the pure E1 value.

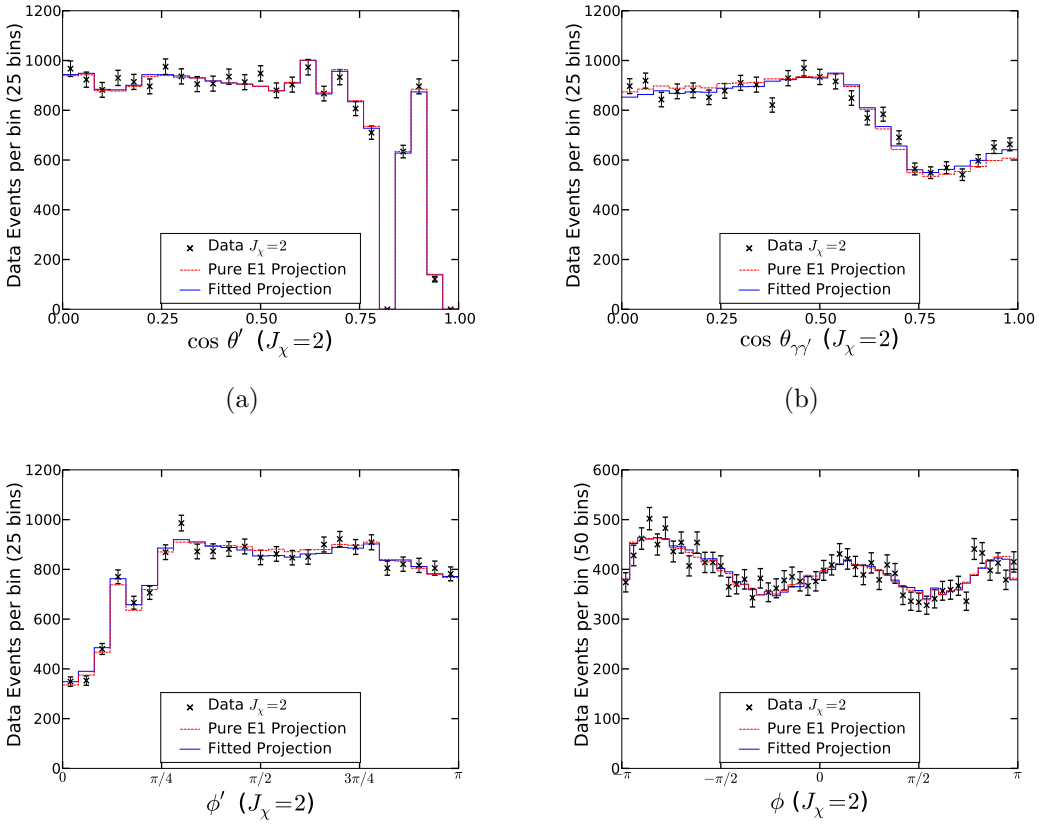

Figure 4.25: $J_\chi = 2$ projections for $\cos\theta', \cos\theta_{\gamma\gamma'}, \phi', \phi$ after using parity transformation to fold the dataset into positive $\cos\theta', \phi', \cos\theta_{\gamma\gamma'}, \cos\theta$. The $\chi^2/N_{\text{d.o.f.}}$ comparing the 25 bin (50 bins for ϕ) histogram of the data to the fitted projection are $15.8/22 = 0.72$, $33.4/22 = 1.52$, $17.8/22 = 0.81$, and $56.1/47 = 1.19$, while the $\chi^2/N_{\text{d.o.f.}}$ comparing data to the pure E1 projection are $17.7/24 = 0.74$, $43.2/24 = 1.80$, $21.3/24 = 0.89$, and $53.3/49 = 1.09$ for $\cos\theta', \cos\theta_{\gamma\gamma'}, \phi'$, and ϕ, respectively. The fitted projection corresponds to the two-parameter fit with $(a_2, b_2) = (-0.093, 0.010)$ with $a_3 \equiv b_3 \equiv 0$, which is 6.2σ from the pure E1 value.

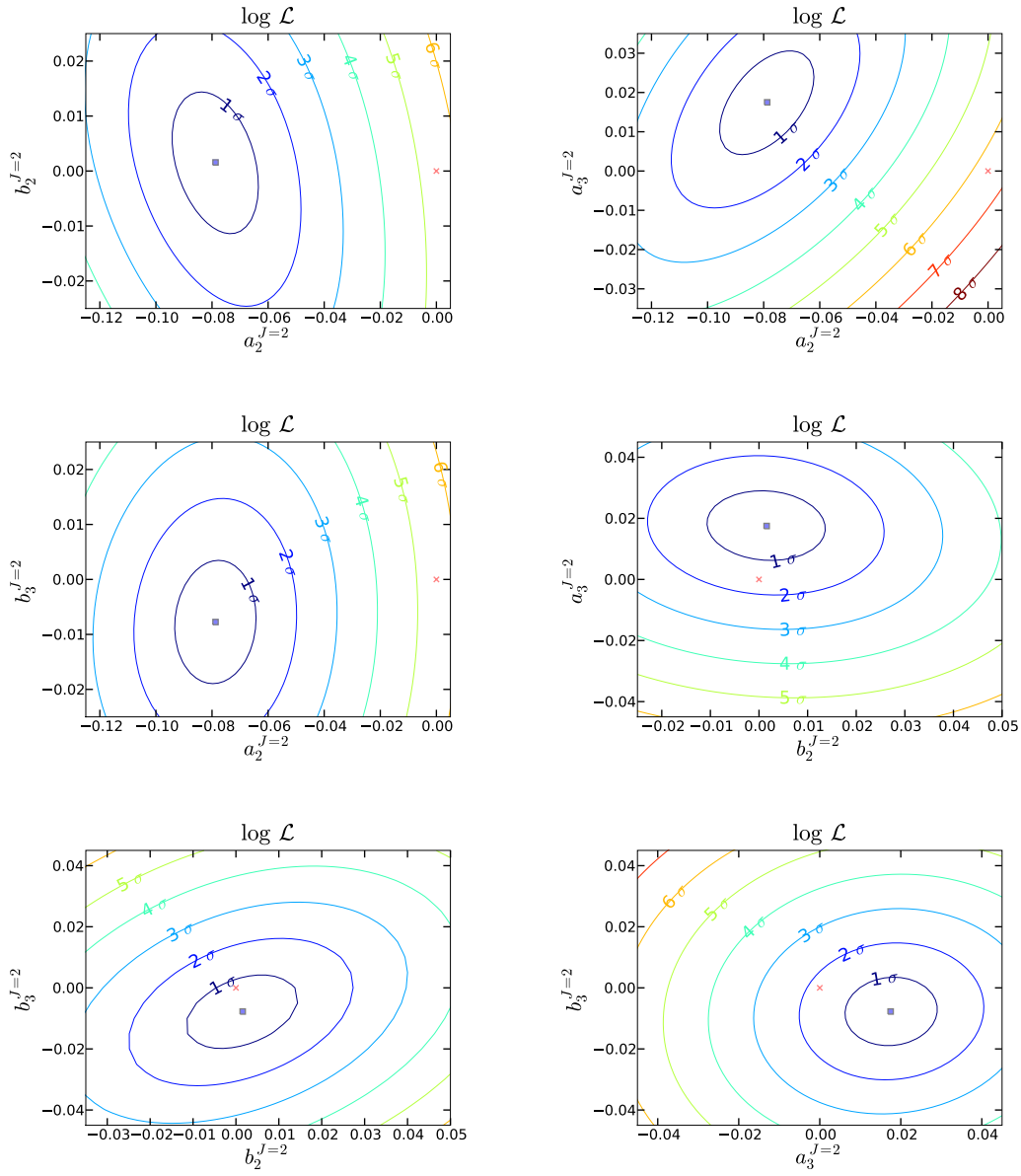

Figure 4.26: Log likelihood curves for four-parameter fits for $J_\chi = 2$. The fitted values of the parameters (■) are $a_2^{J=2} = -0.084 \pm 0.019$, $b_2^{J=2} = 0.006 \pm 0.014$, $a_3^{J=2} = 0.012 \pm 0.014$, $b_3^{J=2} = -0.010 \pm 0.012$ is compared with the pure E1 value (x) and all pairs of multipole amplitudes are plotted holding the other two amplitudes at its fitted value.

Table 4.3: $J_\chi = 2$ five-angle fit results. The fits were performed on the 19755 events selected from `data42` with the selection criteria described in section 4.1. All the amplitudes and uncertainties in the table should be multiplied by 10^{-2}. The theory predictions for $a_3^{J=2}$ is zero as we do not expect the J/ψ to have significant S-D mixing, while the theory prediction for $b_3^{J=2}$ is model dependent on ψ' S-D mixing parameters and the quarkonia potential model used. $\chi_{\mathrm{E1}} \equiv \sqrt{2\Delta \log \mathcal{L}}$ is the number of standard deviations the fitted value is from the pure E1 value.

Fit	$a_2^{J=2}$ 10^{-2}	$b_2^{J=2}$ 10^{-2}	$a_3^{J=2}$ 10^{-2}	$b_3^{J=2}$ 10^{-2}	χ_{E1}
Two-parameter (a_2, b_2)	-9.3 ± 1.6	1.0 ± 1.3	0	0	6.2
Three-parameter	-9.3 ± 1.6	0.7 ± 1.4	0	-0.8 ± 1.2	6.3
Two-param. $b_2 = \frac{-a_2}{3.367}$	-9.2 ± 1.6	2.7 ± 0.5	0	-0.1 ± 1.1	6.1
Four-parameter	-7.9 ± 1.9	0.2 ± 1.5	1.7 ± 1.4	-0.8 ± 1.2	6.4
Theory ($m_c = 1.5\,\mathrm{GeV}$)	$-9.6(1+\kappa_c)$	$2.9(1+\kappa_c)$	0	small	

4.3.3 Large Efficiency Effects on the Projections

With 100% efficiency, we would expect the one-angle projections to follow the integrated distributions given in section 4.4.2. However, there are several well understood large efficiency effects that modulate the shapes of the one-angle projections presented in Figures 4.18, 4.19, 4.22, and 4.23. Due to the finite size of CLEO and near equivalence of the laboratory and ψ' reference frames, $\cos\theta'$ has a complete loss of efficiency due to the hole for the beam pipe at $|\cos\theta'| \geq 0.93$ and a partial loss of efficiency in the region between the barrel and endcap around $|\cos\theta'|$ between about 0.81 and 0.85.

The efficiency loss due to the cut of photon angles in the lab frame of $|\cos\theta_{\rm lab}| < 0.93$ presents a modulation effect in the variable ϕ' in the regions near $\phi' \sim 0$ and $\phi' \sim \pm\pi$. This can be visualized by looking back at the Figure 2.1 that defines the angles and imagine that a small cone of inefficiency surrounds the beam pipe (e^+ and e^- in the figure). For a given angle θ' (where $|\cos\theta'| < 0.93$ so γ' is not lost down the beam-pipe), the photon γ can only be lost down the beam-pipe when the beam-pipe is near the $x' - z'$ plane, which only occurs when ϕ' is near 0 or $\pm\pi$. Therefore, when ϕ' is near 0 or $\pm\pi$ the efficiency is significantly reduced and it is maximally reduced at exactly $\phi' = 0$ and $\phi' = \pm\pi$. A loss of efficiency for $|\cos\theta_{\rm lab}| < 0.93$ should result in an inefficiency of up to $2\arccos(0.93)/\pi \approx 24\%$, however it is slightly greater in our case since there is also a region of inefficiency in the region between the barrel and endcap ($0.79 < |\cos\theta_{\rm lab}| < 0.85$). The inefficiency due to this intermediary region accounts for the kinks in the ϕ' efficiency in both the data and Monte Carlo projections near $\pm\pi/4$ and $\pm 3\pi/4$.

There is also a major efficiency effect in the variable $\cos\theta_{\gamma\gamma'}$ due to the cut on J/ψ momentum, which is made to reduce the background modes $\psi' \to \pi^0 J/\psi$ and

$\psi' \to \eta J/\psi$. Since $E_{\gamma'} \ll m_{\psi'}$, angles and photon energies in the ψ' frame and χ_c frame are nearly identical, and will be exactly identical in the non-relativistic limit. Our signal events are $\psi' \to \gamma'\gamma J/\psi$ with fixed known energies for γ' and γ [5], the J/ψ momentum is related to the angle between the two photons γ and γ' in the laboratory or χ_c frame according to

$$p^2_{J/\psi} = E^2_{\gamma'} + E^2_{\gamma} + 2E_{\gamma'}E_{\gamma}\cos\theta_{\gamma\gamma'}$$
$$\cos\theta_{\gamma\gamma'} = \frac{p^2_{J/\psi} - E^2_{\gamma'} - E^2_{\gamma}}{2E_{\gamma'}E_{\gamma}}$$

by conservation of linear momentum. Therefore, the cuts on J/ψ momentum $|p_{J/\psi}| < 0.510\,\mathrm{GeV}/c$ and $p_{J/\psi} > 0.240\,\mathrm{GeV}/c$ corresponds to the cuts on $\cos\theta_{\gamma\gamma'} < 0.594$ ($\cos\theta_{\gamma\gamma'} < 0.540$ for $J_\chi = 2$) and $\cos\theta_{\gamma\gamma'} > -0.925$ ($\cos\theta_{\gamma\gamma'} > -1.307$ for $J_\chi = 2$) in the non-relativistic limit.

4.4 Results From Less Sensitive Fitting Procedures

4.4.1 Three-Angle Fits (Integrate Over ϕ', ϕ)

If we integrate $W(\Omega; \mathbb{A})$, Eq. (2.6) over ϕ', ϕ we obtain simplified distributions. For the $J_\chi = 1$ case we find:

$$\begin{aligned}\left\langle W^{J=1}(\Omega;\mathbb{A})\right\rangle_{\phi,\phi'} \;\propto\; & |A_0B_0|^2(1+\cos^2\theta)(\cos^2\theta_{\gamma\gamma'})(1+\cos^2\theta') + \\ & |A_0B_1|^2(1+\cos^2\theta)(1-\cos^2\theta_{\gamma\gamma'})(1-\cos^2\theta') + \\ & |A_1B_0|^2(1-\cos^2\theta)(1-\cos^2\theta_{\gamma\gamma'})(1+\cos^2\theta') + \\ & |A_1B_1|^2(1-\cos^2\theta)(1+\cos^2\theta_{\gamma\gamma'})(1-\cos^2\theta') \quad (4.11)\end{aligned}$$

[5] Note γ' is fixed in the ψ' frame and γ is fixed in the χ_c frame. They have a nearly identical value in the other frame, though it will vary slightly (E_γ varies by less than $\pm 8\,\mathrm{MeV}$, $E_{\gamma'}$ varies by less than $\pm 20\,\mathrm{MeV}$) depending on the boost direction between frames.

and for the $J_\chi = 2$ case we find:

$$\begin{aligned}
\left\langle W^{J=2}(\Omega;\mathbb{A})\right\rangle_{\phi,\phi'} \propto \\
& 4|A_0B_0|^2(1+\cos^2\theta)(1-3\cos^2\theta_{\gamma\gamma'})^2(1+\cos^2\theta')+ \\
& 48|A_0B_1|^2(1+\cos^2\theta)(\cos^2\theta_{\gamma\gamma'}-\cos^4\theta_{\gamma\gamma'})(1-\cos^2\theta')+ \\
& 6|A_0B_2|^2(1+\cos^2\theta)(1-\cos^2\theta_{\gamma\gamma'})^2(1+\cos^2\theta')+ \\
& 48|A_1B_0|^2(1-\cos^2\theta)(\cos^2\theta_{\gamma\gamma'}-\cos^4\theta_{\gamma\gamma'})(1+\cos^2\theta')+ \\
& 16|A_1B_1|^2(1-\cos^2\theta)(1-3\cos^2\theta_{\gamma\gamma'}+4\cos^4\theta_{\gamma\gamma'})(1-\cos^2\theta')+ \\
& 8|A_1B_2|^2(1-\cos^2\theta)(1-\cos^4\theta_{\gamma\gamma'})(1+\cos^2\theta')+ \\
& 6|A_2B_0|^2(1+\cos^2\theta)(1-\cos^2\theta_{\gamma\gamma'})^2(1+\cos^2\theta')+ \\
& 8|A_2B_1|^2(1+\cos^2\theta)(1-\cos^4\theta_{\gamma\gamma'})(1-\cos^2\theta')+ \\
& 1|A_2B_2|^2(1+\cos^2\theta)(1+6\cos^2\theta_{\gamma\gamma'}+\cos^4\theta_{\gamma\gamma'})(1+\cos^2\theta'). \qquad (4.12)
\end{aligned}$$

These simplified forms can be quickly fit for the parameters in a fashion similar to the five-angle fits in section 4.3. The results of the three-angle fits are summarized in Tables 4.4 and 4.5. These fits are significantly less sensitive as the phase information is thrown away by assuming that the detector efficiency is uniform over these angles, an assumption that is known to be false. For example, the variable ϕ' has a large dip in detector efficiency near $\phi' = 0, \pm\pi$ due to the hole in the endcap $|\cos\theta'| < 0.93$ (see Section 4.3.3). The efficiency method by defining $F(\Omega;\mathbb{A}) = W(\Omega;\mathbb{A})/\int d\Omega' W(\Omega';\mathbb{A})$ will not account for the efficiency effects in the angles that we integrated out prior to defining W.

Table 4.4: $J=1$ three-angle fit results. The fits were performed on the 39363 events from `data42` selected with the selection criteria described in section 4.1, using the simplified distribution of Eq. (4.11) based on the three-angles $(\cos\theta', \cos\theta_{\gamma\gamma'}, \cos\theta)$.

Fit	$a_2^{J=1}$ 10^{-2}	σ_{a_2} 10^{-2}	$b_2^{J=1}$ 10^{-2}	σ_{b_2} 10^{-2}	$\chi_{\rm E1}$
Two-parameter (three-angle)	-7.40	0.65	1.12	0.79	11.81
One-parameter ($a_2/b_2 = -2.274$)	-6.67	0.57	2.9	0.25	11.56
Theory ($m_c = 1.5\,\text{GeV}$)	$-6.5(1+\kappa_c)$		$2.9(1+\kappa_c)$		

Table 4.5: $J_\chi=2$ three angle fit results. The fits were performed on the 19755 events selected from `data42` with the selection criteria described in section 4.1. All the amplitudes and uncertainties in the table were divided by 10^{-2}. The log likelihood of the data to be described by a pure E1 distribution is $\log\mathcal{L}_{\rm E1} = 84.8$, approximately 4.9 σ from the fitted values. The theory prediction for $a_3^{J=2}$ is zero as we do not expect the J/ψ to have significant S-D mixing, while the theory prediction for $b_3^{J=2}$ depends on ψ' S-D mixing parameters and the quarkonia potential model used.

Fit	$a_2^{J=2}$ 10^{-2}	$b_2^{J=2}$ 10^{-2}	$a_3^{J=2}$ 10^{-2}	$b_3^{J=2}$ 10^{-2}	$\chi_{\rm E1}$
Two-parameter (a_2, b_2)	-8.8 ± 1.9	2.3 ± 1.5	0	0	4.8
Three-parameter	-8.1 ± 2.0	1.2 ± 2.0	0	-1.7 ± 1.8	4.9
Two-param. $b_2 \equiv \frac{-a_2}{3.367}$	-8.3 ± 1.9	2.5 ± 0.6	0	-0.9 ± 1.5	4.9
Four-parameter	-6.2 ± 4.6	0.1 ± 3.2	1.4 ± 3.1	-2.3 ± 2.4	4.9
Theory ($m_c = 1.5\,\text{GeV}$)	$-9.6(1+\kappa_c)$	$2.9(1+\kappa_c)$	0	small	

4.4.2 One-Parameter Fits to One-Angle Distributions

If we further simplify the PDF by integrating over four of the five angles, Eq. (4.11) simplifies to

$$\left\langle W^{J=1}\right\rangle_{\phi',\cos\theta_{\gamma\gamma'},\cos\theta,\phi}(\cos\theta'; b_2) \propto |B_0|^2 + 2|B_1|^2 + \cos^2\theta' \left\{|B_0|^2 - 2|B_1|^2\right\}$$

$$\left\langle W^{J=1}\right\rangle_{\cos\theta',\phi',\cos\theta_{\gamma\gamma'},\phi}(\cos\theta; a_2) \propto |A_0|^2 + 2|A_1|^2 + \cos^2\theta \left\{|A_0|^2 - 2|A_1|^2\right\}$$

$$\begin{aligned}\left\langle W^{J=1}\right\rangle_{\cos\theta',\phi',\cos\theta,\phi}(\cos\theta_{\gamma\gamma'}; a_2, b_2) \propto\ & 2|A_0B_1|^2 + 2|A_1B_0|^2 + |A_1B_1|^2 + \\ & \cos^2\theta_{\gamma\gamma'} \left\{4|A_0B_0|^2 - 2|A_0B_1|^2 - \right. \\ & \left. 2|A_1B_0|^2 + |A_1B_1|^2\right\}\end{aligned}$$

Table 4.6: $J_\chi = 1$ one-angle one-parameter fit results. The fits were performed on the 39363 events from `data42` selected with the selection criteria described in section 4.1, using the simplified distributions of Section 4.4.2. These types of fits are expected to be less sensitive as information is lost. The data are not expected to precisely follow the one-angle PDFs, since these were derived assuming that the four angles that we integrated over had a uniform detector efficiency (while the detector efficiency is not uniform over these four angles).

Fit	$a_2^{J=1}$ 10^{-2}	σ_{a_2} 10^{-2}	$b_2^{J=1}$ 10^{-2}	σ_{b_2} 10^{-2}
One-angle ($\cos\theta'$) b_2 fit			-0.015	0.79
One-angle ($\cos\theta$) a_2 fit	-9.40	0.68		
Theory ($m_c = 1.5\,\mathrm{GeV}$)	$-6.5(1+\kappa_c)$		$2.9(1+\kappa_c)$	

Table 4.7: $J_\chi = 2$ one-angle fit results. The fits were performed on the 19755 events from `data42` selected with the selection criteria described in section 4.1, using the simplified distributions of Section 4.4.2. These types of fits are expected to be less sensitive as information is lost. The data are not expected to precisely follow the one-angle PDFs, since these were derived assuming that the four angles that we integrated over had a uniform detector efficiency (while the detector efficiency is not uniform over these four angles).

Fit	$a_2^{J=2}$ 10^{-2}	σ_{a_2} 10^{-2}	$b_2^{J=2}$ 10^{-2}	σ_{b_2} 10^{-2}
One-angle ($\cos\theta'$) b_2 Fit			14.8	3.2
One-angle ($\cos\theta$) a_2 Fit	-4.5	2.2		
Theory ($m_c = 1.5\,\mathrm{GeV}$)	$-9.6(1+\kappa_c)$		$2.9(1+\kappa_c)$	

and Eq. (4.12) simplifies to

$$\left\langle W^{J=2}\right\rangle_{\phi',\cos\theta_{\gamma\gamma'},\cos\theta\phi}(\cos\theta';b_2,b_3) \propto |B_0|^2 + 2|B_1|^2 + |B_2|^2 + \left(|B_0|^2 - 2|B_1|^2 + |B_2|^2\right)\cos^2\theta'$$

$$\left\langle W^{J=2}\right\rangle_{\cos\theta',\phi',\cos\theta_{\gamma\gamma'},\phi}(\cos\theta;a_2,a_3) \propto |A_0|^2 + 2|A_1|^2 + |A_2|^2 + \left(|A_0|^2 - 2|A_1|^2 + |A_2|^2\right)\cos^2\theta$$

$$\left\langle W^{J=2}\right\rangle_{\cos\theta',\phi',\cos\theta,\phi}(\cos\theta_{\gamma\gamma'};a_2,a_3,b_2,b_3) \propto 4|A_0B_0|^2+4|A_1B_1|^2+$$
$$|A_2B_2|^2+6(|A_0B_2|^2+|A_2B_0|^2)+4(|A_1B_2|^2+|A_2B_1|^2)+$$
$$6\cos^2\theta_{\gamma\gamma'}\left\{\left(|A_2|^2-2|A_0|^2\right)\left(|B_2|^2-2|B_0|^2\right)-\right.$$
$$\left.2(|A_1|^2-2|A_0|^2)\,(|B_1|^2-2|B_0|^2)\right\}+$$
$$\cos^4\theta_{\gamma\gamma'}\left\{\left(6|A_0|^2-4|A_1|^2+|A_2|^2\right)\left(6|B_0|^2-4|B_1|^2+|B_2|^2\right)\right\}$$

Again, the results of these one-angle fits shown in Tables 4.6 and 4.7 are much less sensitive than the full five-angle fits. The major reason is that these integrations assume uniform detector efficiency in the variables we integrated over, which is a very poor assumption for both $\cos\theta'$ and $\cos\theta_{\gamma\gamma'}$ which have large regions of inefficiency as described in Section 4.3.3.

CHAPTER 5

CONSIDERATION OF SYSTEMATIC UNCERTAINTIES

5.1 Consideration of Systematic Uncertainties

In this section, we present the results of systematic studies for the fits to the five angle distributions performed in the previous section. For the $J_\chi = 1$ case, we perform all systematic studies on the two-parameter fit (a_2, b_2) as the one-parameter fixed-ratio fit produces nearly identical results as the more general two-parameter fit. However, for the $J_\chi = 2$ case, there are four types of five-angle fits that can be performed:

- Two-parameter fit (a_2, b_2) with $a_3 \equiv b_3 \equiv 0$, which would be the case with no S-D mixing,
- Three-parameter fit $(a_2, b_2, b_3$ with $a_3 \equiv 0$, which would be the case if we allow for the ψ' to be have a small D state admixture,
- Fixed-ratio two-parameter fit (a_2, b_3) with $b_2 \equiv -a_2/3.367$ and $a_3 \equiv 0$, and
- Four-parameter fit (a_2, b_2, a_3, b_3).

To minimize repetition in the text for $J_\chi = 2$, for some systematic studies we only list the detailed results for the two-parameter fit (a_2, b_2) in this section. The detailed results for the other three fit types are given in the appendices.

For most systematic studies, we perform an ensemble of studies on samples of "signal" events selected from a phase space dataset via the rejection method to follow $W(\Omega; \mathbb{A}_0)$ for a given set of input multipole parameters. The results of the

ensembles of tests are listed in terms of several variables for each fitted multipole amplitude, a, where we give:

- $\langle a \rangle$, the mean of the fitted multipole amplitude over the ensemble of tests,
- σ_a^{ens}, the standard deviation corresponding to the variation of the fitted multipole amplitude over the ensemble of tests,
- σ_a^{fit}, the (mean of the) nominal uncertainty from each individual likelihood fit to multipole amplitude,
- $\Delta_{\langle a \rangle}$, the deviation of the mean from the thrown value of the amplitude when a possible systematic effect is present (in units of the expected deviation of the mean from an ensemble N_{ens} measurements $\sigma_{\langle a \rangle} = \sigma^{\text{fit}}/\sqrt{N_{\text{ens}}}$), defined as:

$$\Delta_{\langle a \rangle} = \frac{\langle a \rangle - a^{\text{Input}}}{\langle \sigma_a^{\text{fit}} \rangle / \sqrt{N_{\text{ens}}}}$$

- $\Delta_{\sigma(a)}$, the deviation of the standard deviation with a potential systematic effect present compared to the standard deviation without the effect present (in units of the expected fluctuation the best estimate of the standard deviation from an ensemble of N measurements $\sigma_\sigma = \sigma/\sqrt{2N}$ [3, Sec. 32.1.1]), defined as:

$$\Delta_{\sigma(a)} = \frac{\sigma^{\text{with syst}} - \sigma^{\text{without syst}}}{\sigma/\sqrt{2N_{\text{ens}}}} \quad \text{, and}$$

- $\chi_{\text{E1}} \equiv \sqrt{2\Delta \log \mathcal{L}}$, the square root of twice the difference in negative log likelihood between the fitted value and the pure E1 value (which nominally corresponds to the number of standard deviations that the fitted value is from pure E1).

For $\sigma^{\rm fit}$ we usually list the mean of the nominal uncertainty, since the uncertainty from every individual likelihood fit in the ensemble was essentially constant ($\sigma_{\sigma_a^{\rm fit}} \lesssim 10^{-2}$. Therefore, this mean $\langle\sigma_a^{\rm fit}\rangle$ is essentially the same as the uncertainty from any given fit $\sigma_a^{\rm fit}$ ($\sigma_{\sigma_a^{\rm fit}} \sim 10^{-2}\sigma_a^{\rm fit}$ when the fits had the same number of data events present).

We assign systematic uncertainties for these ensemble tests, when either

- (a) there's a bias from a potential systematic effect as seen when the mean of an ensemble of tests is biased significantly more than expected by chance (*i.e.*, $|\Delta_{\langle a\rangle}| > 1$), or
- (b) the estimate of the standard deviation of an ensemble of measurements with a possible systematic effect present is much wider than expected, that is $\Delta_{\sigma(a)} > 1$.

If a bias is found, we will correct for the bias and also assign the bias as a systematic uncertainty. If the estimate of the standard deviation of an ensemble of measurements is greater than expected (due to some random systematic effect that widens the distribution), we will assign a systematic uncertainty of $(\sigma^{\rm syst})^2 = (\sigma^{\rm with\ syst})^2 - (\sigma^{\rm without\ syst})^2$.

5.2 Toy MC Check of Fitting Procedure

To test the accuracy of the fitting procedure described in Section 4.2 an ensemble of toy Monte Carlo fitting trials was performed. For each toy MC trial, we generated a large number of toy Monte Carlo phase space events, where each event is described by five random numbers for each of the variables $(\cos\theta', \phi', \cos\theta_{\gamma\gamma'}, \cos\theta, \phi)$

uniformly distributed over the range of the variable. We then generated a set of toy signal Monte Carlo events by selecting events from a separate toy phase space dataset via the rejection method (described in Section 3.4.3), so the events are described by $W(\Omega; \mathbb{A}_0)$ for an input set of multipole parameters $\mathbb{A}_0$.

5.2.1 $J_\chi = 1$ Fits

To test the $J_\chi = 1$ fits, we performed an ensemble of 200 toy MC trials where each trial had $N_{\text{sig}} = 40000$ toy signal events (after cuts) and we used the exact values of the efficiency integrals calculated analytically. We set the multipole amplitudes of the toy signal Monte Carlo to be $a_2^{J=1} = -0.065$, $b_2^{J=1} = 0.029$, the expected multipole amplitudes according to first-order theory with $\kappa_c = 0$ as expected. Fits with other values of input parameters, recover the input results to similar precision. Results are summarized in Table 5.1.

No systematic bias was observed as $|\Delta_{\langle a_2 \rangle}|$ and $|\Delta_{\langle b_2 \rangle}|$ were less than one for all fits. The estimate of the standard deviation of the ensemble $\Delta_{\sigma(a_2)} = 0.87$ and $\Delta_{\sigma(b_2)} = -0.35$ are both less than 1 and are interpreted as being statistical fluctuations of the estimate of the standard deviation. The distribution of the 200 toy MC trials is given in Figure 5.1.

5.2.2 $J_\chi = 2$ Fits

To test the $J_\chi = 2$ fits, we similarly performed an ensemble of 200 toy MC trials where each trial had $N_{\text{sig}} = 20000$ toy signal events. We set the multipole amplitudes of the toy signal Monte Carlo to be $a_2^{J=2} = -0.096$, $b_2^{J=2} = 0.029$,

Table 5.1: $J_\chi = 1$ Toy MC fit results for 200 trials of five angle fits with 40000 toy signal events. The quoted fitting uncertainty (σ) varies little between each trial, and is consistent with the standard deviation of the mean of the ensemble of values. The mean of the fitted values should have a standard deviation of $\sigma/\sqrt{N_{\text{trials}}} = \sigma/\sqrt{200}$, which corresponds well with the observed bias from the input values.

Fit	$\langle a_2^{J=1}\rangle$ 10^{-2}	$\sigma_{a_2}^{\text{ens}}$ 10^{-2}	$\sigma_{a_2}^{\text{fit}}$ 10^{-2}	$\Delta_{\langle a_2\rangle}$ $\sigma_{\langle a_2^{\text{fit}}\rangle}$	$\Delta_{\sigma(a_2)}$ $\sigma_{\sigma(a_2)}$	$\langle b_2^{J=1}\rangle$ 10^{-2}	$\sigma_{b_2}^{\text{ens}}$ 10^{-2}	$\sigma_{b_2}^{\text{fit}}$ 10^{-2}	$\Delta_{\langle b_2\rangle}$ $\sigma_{\langle b_2^{\text{fit}}\rangle}$	$\Delta_{\sigma(b_2)}$ $\sigma_{\sigma(b_2)}$
2-Param.	-6.48	0.58	0.55	0.44	0.87	2.87	0.58	0.59	-0.67	-0.35
1-Par; Fix	-6.49	0.54	0.52	0.35	0.89	2.86	0.24			
Input	-6.5					2.9				

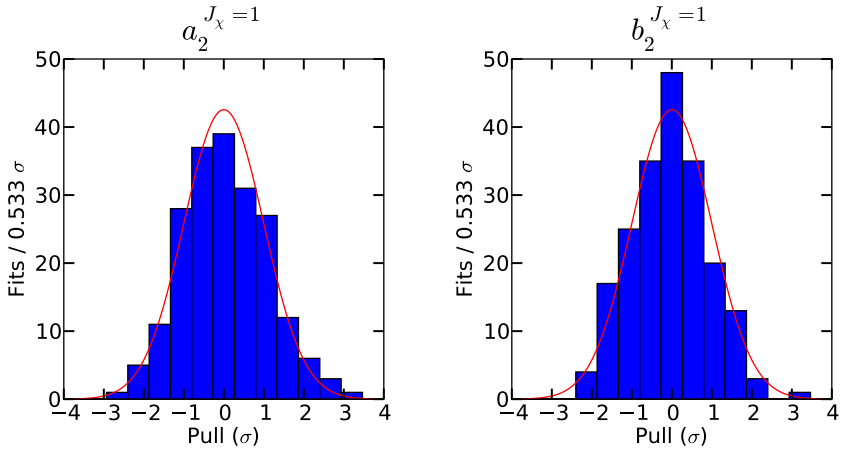

Figure 5.1: Toy Monte Carlo distribution of pulls for an ensemble of 200 fits for $J_\chi = 1$. The pull is the fitted values deviation from the thrown value in units of the standard deviation of each fit. We find that this is consistent with the expected distribution (the red Gaussian).

$b_3 = 0$, $a_3 = 0$. In Table 5.2, we show the results of the toy MC studied for the two-parameter (a_2, b_2) fit. We then compare the quoted fitting uncertainty to the ensemble uncertainty as done for $J_\chi = 1$ and find no systematic uncertainties, as $\Delta_\sigma < 1$ for all multipole amplitudes considered for all five fit types. For the two-parameter fit, we explicitly find $\Delta_{\sigma(a_2)} = 1.1$ and $\Delta_{\sigma(b_2)} = 0.67$, both of which seem consistent with expected statistical fluctuations and for all other fits we find $\Delta_\sigma < 1.3$ (and some fits have as low as $\Delta_\sigma \approx -1.1$). Figure 5.2 shows the

distribution of the 200 trials for the $J_\chi = 2$ two-parameter (a_2, b_2) fit.

Table 5.2: $J_\chi = 2$ Toy MC fit results for 200 trials of five angle fits with 20000 toy signal events. The quoted fitting uncertainty (σ) varies little between each trial, and is consistent with the standard deviation of the mean of the ensemble of values. The mean of the fitted values should have a standard deviation of $\sigma/\sqrt{N_{\text{trials}}} = \sigma/10$, which corresponds well with the observed bias from the input values.

Fit	$a_2^{J=2}$ 10^{-2}	$\sigma_{a_2}^{\text{ens}}$ 10^{-2}	$\sigma_{a_2}^{\text{fit}}$ 10^{-2}	$\Delta_{\langle a_2 \rangle}$ $\sigma_{\langle a_2^{\text{fit}} \rangle}$	$\Delta_{\sigma(a_2)}$ $\sigma_{\sigma(a_2)}$	$b_2^{J=2}$ 10^{-2}	$\sigma_{b_2}^{\text{ens}}$ 10^{-2}	$\sigma_{b_2}^{\text{fit}}$ 10^{-2}	$\Delta_{\langle b_2 \rangle}$ $\sigma_{\langle b_2^{\text{fit}} \rangle}$	$\Delta_{\sigma(b_2)}$ $\sigma_{\sigma(b_2)}$
2-Parameter	-9.5	1.4	1.4	0.8	-0.4	2.9	1.2	1.1	-0.6	0.6
3-Parameter	-9.5	1.4	1.4	0.6	-0.6	2.9	1.3	1.3	-0.3	0.3
2-Par; Fixed	-9.5	1.4	1.4	0.7	-0.6	2.8	0.4	0.4	-1.8	-0.6
4-Parameter	-9.6	1.8	1.8	-0.4	0.4	2.9	1.3	1.3	-0.2	0.7
Input Value	-9.6					2.9				

Fit	$a_3^{J=2}$ 10^{-2}	$\sigma_{a_3}^{\text{ens}}$ 10^{-2}	$\sigma_{a_3}^{\text{fit}}$ 10^{-2}	$\Delta_{\langle a_3 \rangle}$ $\sigma_{\langle a_3^{\text{fit}} \rangle}$	$\Delta_{\sigma(a_3)}$ $\sigma_{\sigma(a_3)}$	$b_3^{J=2}$ 10^{-2}	$\sigma_{b_3}^{\text{ens}}$ 10^{-2}	$\sigma_{b_3}^{\text{fit}}$ 10^{-2}	$\Delta_{\langle b_3 \rangle}$ $\sigma_{\langle b_3^{\text{fit}} \rangle}$	$\Delta_{\sigma(b_3)}$ $\sigma_{\sigma(b_3)}$
2-Parameter	0					0				
3-Parameter	0					0.1	1.1	1.2	0.8	-1.1
2-Par; Fixed	0					0.1	1.0	1.1	0.8	-1.0
4-Parameter	-0.1	1.6	1.5	-1.2	1.2	0.1	1.2	1.2	0.8	-0.9
Input Value	0					0				

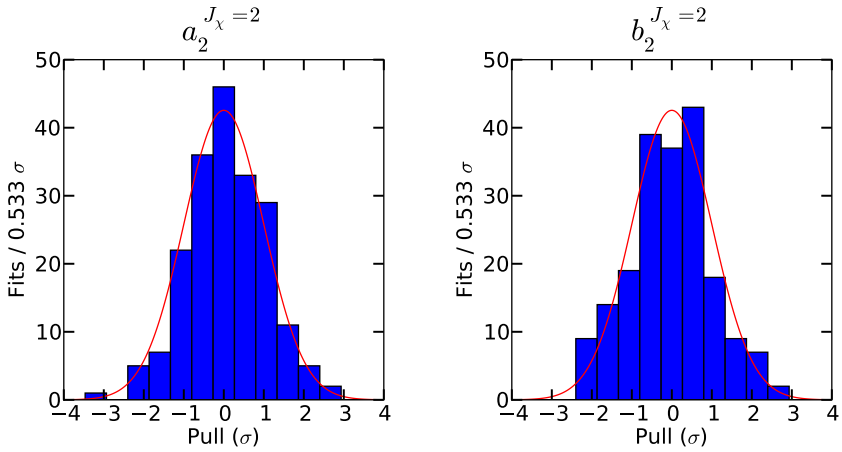

Figure 5.2: Toy Monte Carlo distribution of pulls for an ensemble of 200 fits for $J_\chi = 2$ two-parameter (a_2, b_2) fit. The pull is the fitted values deviation from the thrown value in units of the standard deviation of each fit. We find that this is consistent with the expected distribution (the red Gaussian).

5.3 Phase Space Sample Size For Efficiency Integrals

The efficiency integrals are calculated by doing a Monte Carlo integration with a large dataset of phase space Monte Carlo as shown in Eq. (4.5). Using too few phase space Monte Carlo events would give poor approximations to the efficiency integrals, introducing an overall systematic uncertainty to the results of the maximum likelihood fit.

To test for the minimum number of phase space events needed, we performed ensembles of thirty-one $J_\chi = 1$ simulations and thirty-seven $J_\chi = 2$, using different quantities of phase space Monte Carlo events when estimating the efficiency integrals. We use the 4.5 million event phase space Monte Carlo events for two distinct purposes.

The first purpose is used to select phase space MC events that obey the PDF, $W(\Omega; \mathbb{A}_0)$ given by Eq. (2.6), with the expected values of the multipole amplitudes if $\kappa_c = 0$, that is $\mathbb{A}_0 \equiv (a_2, b_2) = (-0.065, 0.029)$ for $J_\chi = 1$ and $\mathbb{A}_0 \equiv (a_2, b_2, a_3, b_3) = (-0.096, 0.029, 0, 0)$ for $J_\chi = 2$, via the rejection method as described in section 3.4.3. We calculate the probability that each phase space event would arise from the PDF $W(\Omega; \mathbb{A}_0)$ using the pre-FSR (Final State Radiation) generator level values, so that the four-vectors follow $W(\Omega; \mathbb{A}_0)$ before PHOTOS simulates the final state radiation (and not necessarily the kinematically fit four-vectors after final state radiation has been simulated). We do not include the non-signal events in the generic Monte Carlo that pass our selection criteria, as this impurity background is irrelevant to the study of the optimal number of phase space events needed to properly calculate the efficiency integrals. These "signal" events are selected randomly for each fit in the ensemble.

The second purpose is to create random samples of phase space events of different sizes to approximate the efficiency integrals, I_{ijkl} as defined in Eq. (4.5) to varying levels of precision. The phase space events used to calculate the efficiency integrals are extracted from the entire 4.5 million event phase space data set, and are selected randomly from the entire 4.5 million event phase space dataset.

To create a signal dataset from the phase space events, we look at a 24 million event generic Monte Carlo dataset and count the number of signal generic MC events present (at generator level). We then select that number of 'signal' events (selected from the phase space MC according to $W(\Omega; \mathbb{A}_0)$ via the rejection method) and apply the selection criteria to these events.

5.3.1 $J_\chi = 1$

The 4.5 million event phase space dataset allows creation of 2028924 'signal' events, which after cuts amounts to 31 independent datasets with 39650 ± 120 'signal' events in each dataset. We quote phase space sizes after all the cuts have been applied to the phase space events, so the full dataset with 4.5 million events prior to any cuts only has 1780711 events after cuts have been applied. For each independent 'signal' dataset, we select $N_{\rm phsp}$ random phase space events. When possible for each of the 31 simulations, we ensure that the phase space Monte Carlo events for each trial are independent of each other (*i.e.*, no events are used in multiple simulations), though this is only possible when using a phase space size of $N_{\rm phsp} < 100000$. For simulations where it is necessary to repeat phase space events between separate calculations of the phase space integrals, we randomly select phase space events before every simulation. For $N_{\rm phsp} = 1780711$ event trial, each phase space trial is using the full 4.5M event data set, so all of these simu-

lations have the same value of the coefficients in the efficiency integral. Table 5.3 shows the results of these 31 simulations.

We do not find a systematic bias or uncertainty for either parameter when we use more than $\approx 10^5$ phase space events for the efficiency integral. For both multipole amplitudes, we actually find that $\sigma_{\text{ens}} < \langle \sigma^{\text{fit}} \rangle$.

Therefore, since we use the full 4.5 million event phase space dataset for calculation of efficiency integrals in the main analysis, we do not assign a systematic effect.

Table 5.3: Efficiency integral phase space size table for $J_\chi = 1$. The quoted phase space data sizes is the size after applying all the selection criteria. There are no impurity events present in the data sample being fit. The 4.5 million event phase space dataset allowed creation of thirty-one 39650 ± 120 event datasets.

PHSP size (After cuts)	$\langle a_2 \rangle$ 10^{-2}	$\sigma^{\text{ens}}_{a_2}$ 10^{-2}	$\langle \sigma^{\text{fit}}_{a_2} \rangle$ 10^{-2}	$\Delta_{\langle a_2 \rangle}$ $\sigma_{\langle a_2 \rangle}$	$\Delta_{\sigma(a_2)}$ $\sigma_{\sigma(a_2)}$	$\langle b_2 \rangle$ 10^{-2}	$\sigma^{\text{ens}}_{b_2}$ 10^{-2}	$\langle \sigma^{\text{fit}}_{b_2} \rangle$ 10^{-2}	$\Delta_{\langle b_2 \rangle}$ $\sigma_{\langle b_2 \rangle}$	$\Delta_{\sigma(b_2)}$ $\sigma_{\sigma(b_2)}$
1000	-6.65	3.52	0.63	-1.34	36	3.44	4.03	0.72	4.12	36
3000	-6.94	1.76	0.63	-3.9	14	2.86	2.52	0.73	-0.34	20
10000	-6.84	1.11	0.63	-2.96	6.0	2.69	1.65	0.73	-1.59	10
30000	-6.46	0.73	0.63	0.35	1.2	3.11	1.08	0.73	1.6	4
100000	-6.54	0.71	0.63	-0.34	1.0	3.01	0.96	0.73	0.88	2.5
300000	-6.59	0.51	0.63	-0.81	-1.5	3.01	0.79	0.73	0.87	0.76
1780711	-6.54	0.50	0.63	-0.32	-1.6	2.97	0.71	0.73	0.52	-0.11
Input	-6.5					2.9				

5.3.2 $J_\chi = 2$

For the $J_\chi = 2$ case, we have 1759617 phase space events that pass the selection criteria for the efficiency integral calculation. Selecting events with $\mathbb{A} \equiv (a_2, b_2, a_3, b_3) = (-0.096, 0.029, 0, 0)$ gives us enough signal events to perform 37 independent trials with 19950 ± 70 signal events using the 4.5 million event phase space dataset. The results of our $J_\chi = 2$ efficiency integral phase space data size

are shown in Table 5.4 for the two-parameter (a_2, b_2) fit (other fits results are given in the appendix).

As in the $J_\chi = 1$ case, we find no evidence for a systematic uncertainty or bias when we use 10^5 or more phase space events to calculate our efficiency integrals.

Table 5.4: Efficiency integral phase space size table for $J_\chi = 2$ two-parameter (a_2, b_2) fit. The quoted phase space data sizes is the size after applying all the selection criteria. There are no impurity events present in the data sample being fit. The 4.5 million event phase space dataset allowed creation of thirty-seven 19950 ± 70 event datasets.

PHSP size (After cuts)	$\langle a_2 \rangle$ 10^{-2}	$\sigma^{\text{ens}}_{a_2}$ 10^{-2}	$\langle \sigma^{\text{fit}}_{a_2} \rangle$ 10^{-2}	$\Delta_{\langle a_2 \rangle}$ $\sigma_{\langle a_2 \rangle}$	$\Delta_{\sigma(a_2)}$ $\sigma_{\sigma(a_2)}$	$\langle b_2 \rangle$ 10^{-2}	$\sigma^{\text{ens}}_{b_2}$ 10^{-2}	$\langle \sigma^{\text{fit}}_{b_2} \rangle$ 10^{-2}	$\Delta_{\langle b_2 \rangle}$ $\sigma_{\langle b_2 \rangle}$	$\Delta_{\sigma(b_2)}$ $\sigma_{\sigma(b_2)}$
1000	-8.7	7.1	1.6	3.5	30	1.4	6.4	1.3	-6.9	34
3000	-9.3	4.1	1.6	1.2	13	2.0	3.1	1.3	-4.5	12
10000	-9.5	2.9	1.6	0.5	7.0	2.8	2.0	1.2	-0.4	4.6
30000	-9.6	2.0	1.6	0.2	2.1	3.0	1.6	1.2	0.3	2.9
100000	-9.7	1.6	1.6	-0.5	0.1	3.0	1.3	1.2	0.7	0.7
300000	-9.6	1.4	1.6	-0.2	-0.8	3.0	1.3	1.2	0.4	0.4
1675003	-9.8	1.4	1.6	-0.6	-0.6	3.0	1.3	1.2	0.6	0.3
Input	-9.6					2.9				

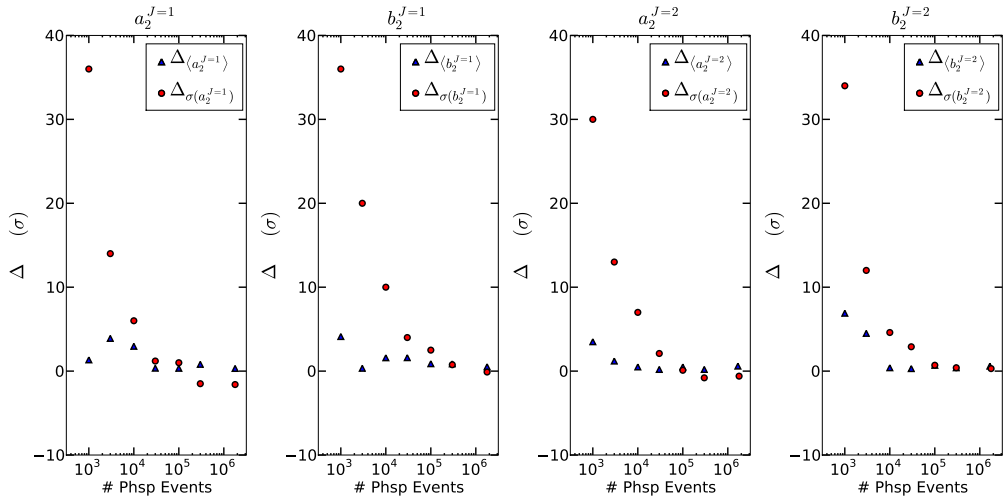

Figure 5.3: Efficiency integral phase space size for two-parameter (a_2, b_2) fits for $J_\chi = 1$ and $J_\chi = 2$. We plot the observed bias and the increase in the width of the distribution vs number of phase space events, both in units of the expected standard deviation. We find for under $\approx 10^5$ events that large statistical uncertainties and biases will arise.

5.4 Impurity Systematic Uncertainties

5.4.1 $J_\chi = 1$

For the $J_\chi = 1$ selection criteria, approximately 0.23% of the events that pass the cuts are not signal events, but a background mode that must be considered for the possibility of introducing a systematic bias or uncertainty to our result. Taking our five-fold data42 generic Monte Carlo dataset and splitting it into five independent datasets, we find the background impurities shown in Table 5.5.

For each of the five independent generic MC impurity backgrounds, we perform an ensemble of 31 trials without the impurity background events present and with the impurity backgrounds present. We then compare the results of each of the trials with and without impurities present and find that the inclusion of impurity shifts each trial (with the same signal events) almost exactly the same amount. That is, for the exact same signal events selected, we perform one fit without impurity events included and one fit with impurity events included and subtract the difference on a trial by trial basis. We then average these biases over the five Monte Carlo samples to find a consistent systematic bias of $(0.15 \pm 0.03) \times 10^{-2}$ for $a_2^{J=1}$ and $(0.05 \pm 0.03) \times 10^{-2}$ for $b_2^{J=1}$. This systematic bias is corrected for in the final result, which we also assign as a systematic uncertainty.

The results are shown in Table 5.6. We also show the result if all five impurity backgrounds are added to a standard sized data set, and the impurity bias that results is almost exactly five times larger than the impurity bias from including only one set of impure events. This demonstrates how the bias from impure events for the $J_\chi = 1$ selection criteria tends to scale linearly with the number of impure

events present in the data.

Table 5.5: Investigation of impurities present in each of the five Generic MC data samples, after applying the $J_\chi = 1$ selection criteria. Our selection criteria give us a purity of 99.77% and an efficiency of selecting 39.6% of the original signal events. The main sources of impurity background modes are $\psi' \to \pi^0\pi^0 J/\psi$ and $\psi' \to \gamma'\chi_{c1}$ (where the χ_{c1} didn't radiatively decay to a J/ψ that decayed into two leptons).

Event type	GenMC A	GenMC B	GenMC C	GenMC D	GenMC E	Total
Signal Events Sel.	39701	40207	39460	39662	39429	198459
Impure Events	93	82	105	95	87	462
Signal Efficiency	39.6%	39.7%	39.4%	39.6%	39.6%	39.6%
Purity	99.76%	99.80%	99.73%	99.76%	99.78%	99.77%
$\pi^0\pi^0 J/\psi$	50	47	64	53	50	264
$\pi^0 J/\psi$	0	0	0	0	0	0
$\eta J/\psi$	2	0	2	1	0	5
$\gamma'\chi_{c0}$	10	5	7	5	8	35
$\gamma'\chi_{c1}$ (non-signal)	26	28	26	31	25	136
$\gamma'\chi_{c2}$	2	2	4	2	2	12
$\mu^+\mu^-$	0	0	1	2	1	4
e^+e^-	2	0	0	0	1	3
Others	1	0	1	1	0	3

Table 5.6: Generic MC impurity systematic tests for a systematic bias for $J_\chi = 1$. We find that the impurities add a negligible systematic uncertainty when compared with the statistical uncertainty.

Type	$\langle a_2 \rangle$ 10^{-2}	$\sigma_{a_2}^{\rm ens}$ 10^{-2}	$\langle \sigma_{a_2}^{\rm fit} \rangle$ 10^{-2}	$\Delta_{\langle a_2 \rangle}$ $\sigma_{\langle a_2 \rangle}$	$\langle b_2 \rangle$ 10^{-2}	$\sigma_{b_2}^{\rm ens}$ 10^{-2}	$\langle \sigma_{b_2}^{\rm fit} \rangle$ 10^{-2}	$\Delta_{\langle b_2 \rangle}$ $\sigma_{\langle b_2 \rangle}$
Pure	-6.54	0.5	0.63	-0.32	2.97	0.71	0.73	0.52
Diff. (A)	-0.15	0.002			-0.058	0.003		
Diff. (B)	-0.12	0.002			-0.053	0.003		
Diff. (C)	-0.14	0.003			-0.06	0.005		
Diff. (D)	-0.216	0.004			-0.095	0.005		
Diff. (E)	-0.109	0.002			0.031	0.003		
Diff. (A-E)	-0.73	0.011			-0.241	0.019		
Input	-6.5				2.9			
$\langle$Imp. Bias$\rangle$	0.15	0.03			0.05	0.03		

5.4.2 $J_\chi = 2$

For the $J_\chi = 2$ selection criteria, we find in the Generic Monte Carlo that 0.29% of the selected events are not signal events. The dominant background modes are $\psi' \to \gamma\chi_{c1}$ and $\psi' \to \pi^0\pi^0 J/\psi$. The background modes selected are shown in Table 5.7 for each of our five generic Monte Carlo datasets. For each of the five independent generic MC impurity backgrounds, we perform an ensemble of 37 trials with and without the impurity background events present. Unlike in the $J_\chi = 1$ case where we found an appreciable impurity bias, in all the $J_\chi = 2$ fit types studied here, the impurity bias is negligible ($\sim 0.01 \times 10^{-2}$) when compared with the statistical uncertainty ($\sim 1.5 \times 10^{-2}$). We do not assign a systematic bias that we correct for, but do assign the standard deviation of the various impurity biases as a systematic uncertainty.

Table 5.7: Investigation of impurities present in each of the five Generic MC data samples, after applying the $J_\chi = 2$ selection criteria. Our selection criteria give us a purity of 99.71% and an efficiency of selecting 36.0% of the original signal events. The main sources of impurity background modes are $\psi' \to \gamma'\chi_{c1}$ and $\psi' \to \pi^0\pi^0 J/\psi$.

Event type	GenMC A	GenMC B	GenMC C	GenMC D	GenMC E	Total
Signal Events Sel.	19805	19531	19508	20054	19731	98629
Impure Events	57	48	59	47	66	277
Signal Efficiency	35.9%	35.8%	36.0%	36.4%	35.9%	36.0%
Purity	99.71%	99.75%	99.70%	99.77%	99.65%	99.71%
$\pi^0\pi^0 J/\psi$	8	13	11	7	11	50
$\pi^0 J/\psi$	0	0	1	0	1	2
$\eta J/\psi$	0	0	0	0	0	0
$\gamma'\chi_{c0}$	2	1	2	1	3	9
$\gamma'\chi_{c1}$	30	14	23	24	26	117
$\gamma'\chi_{c2}$ (non-signal)	14	18	19	15	20	86
$\mu^+\mu^-$	2	2	2	0	3	9
e^+e^-	1	0	1	0	2	4
Others	0	0	0	0	0	0

Table 5.8: Generic MC impurity systematic tests for a systematic bias for $J_\chi = 2$ two-parameter (a_2, b_2) fit. We find that the impurities add a negligible systematic uncertainty when compared with the statistical uncertainty.

Type	$\langle a_2 \rangle$ 10^{-2}	$\sigma_{a_2}^{\text{ens}}$ 10^{-2}	$\langle \sigma_{a_2}^{\text{fit}} \rangle$ 10^{-2}	$\Delta_{\langle a_2 \rangle}$ $\sigma_{\langle a_2 \rangle}$	$\langle b_2 \rangle$ 10^{-2}	$\sigma_{b_2}^{\text{ens}}$ 10^{-2}	$\langle \sigma_{b_2}^{\text{fit}} \rangle$ 10^{-2}	$\Delta_{\langle b_2 \rangle}$ $\sigma_{\langle b_2 \rangle}$
Pure	-9.8	1.4	1.6	-0.6	3.0	1.3	1.2	0.6
Diff. (A)	-0.005	0.006			0.078	0.003		
Diff. (B)	0.08	0.004			-0.011	0.005		
Diff. (C)	-0.008	0.011			0.149	0.004		
Diff. (D)	0.022	0.003			-0.05	0.003		
Diff. (E)	-0.041	0.002			0.027	0.003		
Diff. (A-E)	0.047	0.019			0.19	0.011		
Input	-9.6				2.9			
$\langle$Imp. Bias$\rangle$	0.009	0.040			0.038	0.070		

5.5 Final State Radiation

Another possible source of systematic uncertainty is the effect of Final State Radiation (FSR), which can alter the angles describing the signal decay. Generation of Monte Carlo has been done using EvtGen, which models final state radiation in the decay sequences $J/\psi \to \ell^+\ell^-$ with PHOTOS. We estimate the effect of final state radiation by performing signal fits on the angles Ω from generator level four-vectors, both before and after final state radiation has been added. We use the rejection method (described in section 3.4.3) to select events, so that the pre-FSR generator level four-vectors follow the PDF $W(\Omega; \mathbb{A}_0)$ for an input value of the multipole amplitudes $\mathbb{A}_0$. Again, we are careful to use the pre-FSR four-vectors when selecting the phase space events to be used as 'signal' described by the PDF $W(\Omega; \mathbb{A}_0)$ with a given $\mathbb{A}_0 \equiv (a_2, b_2) = (-0.065, 0.029)$ (for $J_\chi = 2$, $\mathbb{A}_0 \equiv (a_2, b_2, a_3, b_3) = (-0.096, 0.029, 0.0, 0.0)$). We then compare the fit on the selected events using the pre-FSR and post-FSR generator level to check for a systematic uncertainty from final state radiation.

For the final state radiation test with $J_\chi = 1$, we performed 53 trials with 40000 pre-FSR generator events, and 46 trials with 40000 post-FSR generator value events. We also performed tests, where we used the E/p cut to perform muon-only (where $J/\psi \to \mu^-\mu^-$) or electron-only ($J/\psi \to e^+e^-$) fits where we still kept the number of events selected at 40000. We required the pre-FSR and post-FSR events to pass all selection criteria (except the kinematic fit requirement as no kinematic fit is performed on generator values), so we had slightly fewer post-FSR events as sometimes the effects of FSR would cause signal events to fail the selection criteria. Looking at Table 5.9, we compare the ensemble standard deviation using the pre-FSR fit and the post-FSR fit to check for a systematic uncertainty due to final state radiation and find no systematic uncertainties for any of the cases considered.

For the final state radiation test for the $J_\chi = 2$ two-parameter (a_2, b_2) fit shown in Table 5.10, we do not see a bias or a significant increase in the ensemble standard deviation between the pre-FSR and post-FSR values.

Table 5.9: Final state radiation for $J_\chi = 1$. All the types of fits involved exactly 40000 data events selected so the pre-FSR generator values followed the $W(\Omega; \mathbb{A}_0)$ with $\mathbb{A}_0 = (-0.065, 0.029)$.

Type	$\langle a_2 \rangle$ 10^{-2}	$\sigma^{\text{ens}}_{a_2}$ 10^{-2}	$\langle \sigma^{\text{fit}}_{a_2} \rangle$ 10^{-2}	$\Delta_{\langle a_2 \rangle}$ $\sigma_{\langle a_2 \rangle}$	$\langle b_2 \rangle$ 10^{-2}	$\sigma^{\text{ens}}_{b_2}$ 10^{-2}	$\langle \sigma^{\text{fit}}_{b_2} \rangle$ 10^{-2}	$\Delta_{\langle b_2 \rangle}$ $\sigma_{\langle b_2 \rangle}$	N
Pre-FSR	-6.52	0.58	0.57	-0.22	2.89	0.59	0.6	-0.08	53
Pre-FSR ($\mu^+\mu^-$ only)	-6.58	0.58	0.57	-0.72	2.86	0.52	0.59	-0.33	29
Pre-FSR (e^+e^- only)	-6.43	0.49	0.57	0.57	2.97	0.52	0.6	0.52	23
Post-FSR	-6.55	0.49	0.57	-0.56	2.87	0.46	0.6	-0.35	46
Post-FSR ($\mu^+\mu^-$ only)	-6.61	0.49	0.57	-1.03	2.86	0.59	0.6	-0.35	27
Post-FSR (e^+e^- only)	-6.44	0.9	0.57	0.46	2.92	0.53	0.61	0.15	18
Input	-6.5				2.9				

Table 5.10: Final state radiation for $J_\chi = 2$ two-parameter (a_2, b_2) fit. We performed $N = 32$ pre-FSR and $N = 33$ post-FSR trials with exactly 20000 data events in each fit. Each trial had a five angle two-parameter fit performed with $W(\Omega; \mathbb{A}_0)$ with $\mathbb{A}_0 = (-0.096, 0.029, 0, 0)$.

Type	$\langle a_2 \rangle$ 10^{-2}	$\sigma^{\text{ens}}_{a_2}$ 10^{-2}	$\langle \sigma^{\text{fit}}_{a_2} \rangle$ 10^{-2}	$\Delta_{\langle a_2 \rangle}$ $\sigma_{\langle a_2 \rangle}$	$\langle b_2 \rangle$ 10^{-2}	$\sigma^{\text{ens}}_{b_2}$ 10^{-2}	$\langle \sigma^{\text{fit}}_{b_2} \rangle$ 10^{-2}	$\Delta_{\langle b_2 \rangle}$ $\sigma_{\langle b_2 \rangle}$	N
Pre-FSR	-9.6	1.5	1.4	0.3	3.0	1.0	1.1	0.9	68
Pre-FSR ($\mu^+\mu^-$ only)	-9.5	1.1	1.3	0.4	3.0	0.9	1.1	0.6	38
Pre-FSR (e^+e^- only)	-9.6	1.3	1.4	0.2	3.0	1.3	1.2	0.5	30
Post-FSR	-9.6	1.6	1.4	0.3	3.0	1.0	1.1	0.9	59
Post-FSR ($\mu^+\mu^-$ only)	-9.6	1.4	1.3	0.2	3.0	1.2	1.1	0.6	35
Post-FSR (e^+e^- only)	-9.5	1.4	1.4	0.3	3.1	1.2	1.2	0.6	23
Input	-9.6				2.9				

5.6 Choice of Kinematic Fits Performed

For our analysis, we perform a 1C kinematic fit to the J/ψ mass and a 4C kinematic fit to the ψ' four momentum of the lab frame and we also perform bremsstrahlung reconstruction on each track if any showers were tagged as brems belonging to the track. To test for possible systematic effects, we perform an ensemble of tests on phase space MC shaped to have $\mathbb{A}_0 = (-0.065, 0.029)$ for $J_\chi = 1$ and $\mathbb{A}_0 = (-0.096, 0.029, 0, 0)$ for $J_\chi = 2$ with four vectors selected to have the pre-FSR generator photons follow $W(\Omega; \mathbb{A}_0)$. We construct the four vectors for the variables in three different ways:

- Post-FSR generator level four-vectors
- 1C and 4C kinematic fits without bremsstrahlung recovery
- 1C and 4C kinematic fits with bremsstrahlung recovery

For each type of four-vectors, we perform as many fits as possible using data size (after selection criteria) of 40000 $J_\chi = 1$ (20000 $J_\chi = 2$) events in each fit. The results for $J_\chi = 1$ are summarized in Table 5.11, and the $J_\chi = 2$ (two-parameter a_2, b_2) results are summarized in Table 5.12. We see that for nearly all variables as $\sigma^{\text{ens}} \cong \langle \sigma^{\text{fit}} \rangle$ when we perform the 1C and 4C kinematic fits with bremsstrahlung recovery, so we assign no systematic uncertainty to the choice of kinematic fit. Without performing brem recovery there would be a small systematic uncertainty for many of these types of fits.

Table 5.11: Kinematic fit table for $J_\chi = 1$. We see no systematic uncertainty introduced by the type of kinematic fit performed when we perform the 1C and 4C fit with bremsstrahlung recovery.

Type	$\langle a_2 \rangle$ 10^{-2}	$\sigma^{\text{ens}}_{a_2}$ 10^{-2}	$\langle \sigma^{\text{fit}}_{a_2} \rangle$ 10^{-2}	$\Delta_{\langle a_2 \rangle}$ $\sigma_{\langle a_2 \rangle}$	$\langle b_2 \rangle$ 10^{-2}	$\sigma^{\text{ens}}_{b_2}$ 10^{-2}	$\langle \sigma^{\text{fit}}_{b_2} \rangle$ 10^{-2}	$\Delta_{\langle b_2 \rangle}$ $\sigma_{\langle b_2 \rangle}$	N
Post-FSR	-6.55	0.49	0.57	-0.56	2.87	0.46	0.6	-0.35	46
4C, 1C (no b.r.)	-6.49	0.6	0.63	0.1	2.98	0.74	0.72	0.62	33
4C, 1C (brem. rec.)	-6.42	0.66	0.62	0.77	2.97	0.65	0.71	0.6	36
Input	-6.5				2.9				

Table 5.12: Kinematic fit table for $J_\chi = 2$ two-parameter (a_2, b_2) fit. We see no systematic uncertainty introduced by the type of kinematic fit performed when we perform the 1C and 4C fit with bremsstrahlung recovery.

Type	$\langle a_2 \rangle$ 10^{-2}	$\sigma^{\text{ens}}_{a_2}$ 10^{-2}	$\langle \sigma^{\text{fit}}_{a_2} \rangle$ 10^{-2}	$\Delta_{\langle a_2 \rangle}$ $\sigma_{\langle a_2 \rangle}$	$\langle b_2 \rangle$ 10^{-2}	$\sigma^{\text{ens}}_{b_2}$ 10^{-2}	$\langle \sigma^{\text{fit}}_{b_2} \rangle$ 10^{-2}	$\Delta_{\langle b_2 \rangle}$ $\sigma_{\langle b_2 \rangle}$	N
Post-FSR	-9.6	1.6	1.4	0.3	3.0	1.0	1.1	0.9	59
4C, 1C (no b.r.)	-9.7	1.6	1.5	-0.3	3.2	1.3	1.2	1.5	40
4C, 1C (brem. rec.)	-9.7	1.6	1.5	-0.5	3.1	1.2	1.2	1.2	43
Input	-9.6				2.9				

5.7 Cut Variation

To look for an additional systematic uncertainty from possible cut variations, we looked at the following cut variations for the statistical uncertainty and systematic impurity uncertainty:

- Default Cuts
- Maximum 3rd Shower Energy: 30 MeV $\rightarrow$ 18 MeV
- Maximum 3rd Shower Energy: 30 MeV $\rightarrow$ 50 MeV
- Maximum Reduced χ^2: 16 $\rightarrow$ 10
- Maximum Reduced χ^2: 16 $\rightarrow$ 30
- χ_c mass window $\pm$15 MeV $\rightarrow$ $\pm$10 MeV
- χ_c mass window $\pm$15 MeV $\rightarrow$ $\pm$20 MeV

These cuts were chosen, as they loosen and tighten all of the cuts that we perform. As shown in Tables 5.13 and 5.14 for $J_\chi = 1$, we found that the default cuts (defined in Section 4.1.6) had the smallest quadrature sum of the statistical uncertainty with impurity systematic uncertainty. We further found that over the ensemble of tests at various cut criteria, the mean from the ensemble of tests for a_2 and b_2 (when no impurities were present) varied only slightly. For the $J_\chi = 2$ two-parameter (a_2, b_2) fit case shown in Tables 5.15 and 5.16, we found that while we were quite near the minimal total quadrature sum at the default cuts, we could have achieved a $\sim 3\%$ improvement if we loosened the cuts. However, to achieve that $\sim 3\%$ improvement requires increasing the number of impure events by a factor of approximately five as shown in Fig. 4.9, so it was not performed.

Table 5.13: Cut variations for $J_\chi = 1$. Using the default cut values for the parameters not being changed, we tighten and then loosen each of the cut parameters as described in the text, to find the statistical uncertainty and impurity bias for each set of cut values. We summarize the results of these fits in Table 5.14.

Type	$\langle a_2 \rangle$ 10^{-2}	$\sigma_{a_2}^{\text{ens}}$ 10^{-2}	$\langle \sigma_{a_2}^{\text{fit}} \rangle$ 10^{-2}	$\frac{\Delta_{\langle a_2 \rangle}}{\sigma_{\langle a_2 \rangle}}$	$\langle b_2 \rangle$ 10^{-2}	$\sigma_{b_2}^{\text{ens}}$ 10^{-2}	$\langle \sigma_{b_2}^{\text{fit}} \rangle$ 10^{-2}	$\frac{\Delta_{\langle b_2 \rangle}}{\sigma_{\langle b_2 \rangle}}$
Default Cuts Signal	-6.54	0.5	0.63	-0.32	2.97	0.71	0.73	0.52
Default Cuts Diff.	-0.15	0.002			-0.058	0.003		
$E^{\text{3rd Shwr}} < 18\,\text{MeV}$ Signal	-6.53	0.54	0.66	-0.26	2.98	0.73	0.76	0.56
$E^{\text{3rd Shwr}} < 18\,\text{MeV}$ Diff.	-0.075	0.001			-0.064	0.002		
$E^{\text{3rd Shwr}} < 50\,\text{MeV}$ Signal	-6.51	0.48	0.62	-0.11	2.95	0.71	0.71	0.42
$E^{\text{3rd Shwr}} < 50\,\text{MeV}$ Diff.	-0.304	0.005			-0.129	0.007		
$\chi^2 < 10$ Signal	-6.55	0.54	0.65	-0.46	2.95	0.76	0.75	0.35
$\chi^2 < 10$ Diff.	-0.053	0.001			-0.031	0.001		
$\chi^2 < 30$ Signal	-6.54	0.51	0.62	-0.39	2.96	0.73	0.71	0.45
$\chi^2 < 30$ Diff.	-0.308	0.004			-0.041	0.007		
χ_c mass $\pm 10\,\text{MeV}$ Signal	-6.54	0.51	0.64	-0.35	2.98	0.72	0.74	0.59
χ_c mass $\pm 10\,\text{MeV}$ Diff.	-0.112	0.002			-0.04	0.002		
χ_c mass $\pm 20\,\text{MeV}$ Signal	-6.54	0.5	0.63	-0.31	2.98	0.71	0.72	0.61
χ_c mass $\pm 20\,\text{MeV}$ Diff.	-0.178	0.003			-0.092	0.004		
$\lvert\cos\theta_{\text{lab,ph}}^{\text{barrel}}\rvert < 0.77$ Signal	-6.5	0.52	0.65	-0.01	2.97	0.72	0.75	0.49
3.04	0.72	0.75	1.02					
$\lvert\cos\theta_{\text{lab,ph}}^{\text{barrel}}\rvert < 0.77$ Diff.	-0.156	0.002			-0.07	0.004		
$\lvert\cos\theta_{\text{lab,ph}}^{\text{barrel}}\rvert < 0.80$ Signal	-6.52	0.48	0.62	-0.21	2.97	0.72	0.72	0.57
$\lvert\cos\theta_{\text{lab,ph}}^{\text{barrel}}\rvert < 0.80$ Diff.	-0.156	0.002			-0.065	0.004		

Table 5.14: Cut variation summary table for $J_\chi = 1$. We compare the statistical uncertainty, impurity bias (assigned as a systematic uncertainty) and their quadrature sum found in Table 5.13. We find that the default cuts have the minimum total quadrature uncertainty.

Cuts	$\sigma_{a_2}^{\text{stat}}$ 10^{-2}	$\sigma_{a_2}^{\text{sys imp}}$ 10^{-2}	$\sigma_{a_2}^{\text{total quad sum}}$ 10^{-2}	$\sigma_{b_2}^{\text{stat}}$ 10^{-2}	$\sigma_{b_2}^{\text{sys imp}}$ 10^{-2}	$\sigma_{b_2}^{\text{total quad sum}}$ 10^{-2}
Default Cuts	0.631	0.150	0.648	0.726	0.058	0.728
$E^{\text{3rd Shwr}} < 18\,\text{MeV}$	0.657	0.075	0.661	0.757	0.064	0.76
$E^{\text{3rd Shwr}} < 50\,\text{MeV}$	0.621	0.304	0.691	0.714	0.129	0.725
$\chi^2_{\text{k.f.}} < 10$	0.650	0.053	0.652	0.749	0.031	0.750
$\chi^2_{\text{k.f.}} < 30$	0.618	0.308	0.690	0.711	0.041	0.712
χ_c mass $\pm 10\,\text{MeV}$	0.643	0.112	0.652	0.740	0.040	0.741
χ_c mass $\pm 20\,\text{MeV}$	0.628	0.178	0.652	0.722	0.092	0.728
$\lvert\cos\theta_{\text{lab,ph}}^{\text{barrel}}\rvert < 0.77$	0.647	0.156	0.666	0.747	0.07	0.751
$\lvert\cos\theta_{\text{lab,ph}}^{\text{barrel}}\rvert < 0.80$	0.625	0.156	0.644	0.718	0.065	0.721

Table 5.15: Cut variations for $J_\chi = 2$ two-parameter (a_2, b_2) fit. Using the default cut values for the parameters not being changed, we tighten and then loosen each of the cut parameters as described in the text, to find the statistical uncertainty and impurity bias for each set of cut values. We summarize the results of these fits in Table 5.16.

Type	$\langle a_2 \rangle$ 10^{-2}	$\sigma_{a_2}^{\text{ens}}$ 10^{-2}	$\langle \sigma_{a_2}^{\text{fit}} \rangle$ 10^{-2}	$\frac{\Delta_{\langle a_2 \rangle}}{\sigma_{\langle a_2 \rangle}}$	$\langle b_2 \rangle$ 10^{-2}	$\sigma_{b_2}^{\text{ens}}$ 10^{-2}	$\langle \sigma_{b_2}^{\text{fit}} \rangle$ 10^{-2}	$\frac{\Delta_{\langle b_2 \rangle}}{\sigma_{\langle b_2 \rangle}}$
Default Cuts Signal	-9.8	1.4	1.6	-0.6	3.0	1.3	1.2	0.6
Default Cuts Diff.	-0.005	0.006			0.078	0.003		
$E^{\text{3rd Shwr}} < 18\,\text{MeV}$ Signal	-9.8	1.5	1.6	-0.7	3.1	1.3	1.3	1.0
$E^{\text{3rd Shwr}} < 18\,\text{MeV}$ Diff.	0.034	0.006			0.089	0.003		
$E^{\text{3rd Shwr}} < 50\,\text{MeV}$ Signal	-9.8	1.3	1.5	-0.7	3.0	1.2	1.2	0.6
$E^{\text{3rd Shwr}} < 50\,\text{MeV}$ Diff.	0.128	0.013			0.224	0.008		
$\chi^2_{\text{k.f.}} < 10$ Signal	-9.8	1.5	1.6	-0.9	3.1	1.3	1.3	0.8
$\chi^2_{\text{k.f.}} < 10$ Diff.	-0.023	0.003			0.052	0.002		
$\chi^2_{\text{k.f.}} < 30$ Signal	-9.7	1.4	1.5	-0.4	3.0	1.2	1.2	0.7
$\chi^2_{\text{k.f.}} < 30$ Diff.	-0.119	0.008			0.096	0.008		
χ_c mass $\pm 10\,\text{MeV}$ Signal	-9.8	1.4	1.6	-0.6	3.0	1.2	1.3	0.4
χ_c mass $\pm 10\,\text{MeV}$ Diff.	0.033	0.003			0.023	0.002		
χ_c mass $\pm 20\,\text{MeV}$ Signal	-9.7	1.3	1.5	-0.5	3.0	1.2	1.2	0.6
χ_c mass $\pm 20\,\text{MeV}$ Diff.	0.068	0.01			0.125	0.006		
$\lvert\cos\theta_{\text{lab,ph}}^{\text{barrel}}\rvert < 0.77$ Signal	-9.8	1.4	1.6	-0.8	3.0	1.2	1.3	0.6
$\lvert\cos\theta_{\text{lab,ph}}^{\text{barrel}}\rvert < 0.77$ Diff.	-0.013	0.006			0.067	0.003		
$\lvert\cos\theta_{\text{lab,ph}}^{\text{barrel}}\rvert < 0.80$ Signal	-9.8	1.4	1.5	-0.7	3.0	1.3	1.2	0.5
$\lvert\cos\theta_{\text{lab,ph}}^{\text{barrel}}\rvert < 0.80$ Diff.	-0.017	0.006			0.076	0.003		

Table 5.16: Cut variation summary for $J_\chi = 2$ two-parameter (a_2, b_2) fit. We compare the statistical uncertainty, impurity bias (assigned as a systematic uncertainty) and their quadrature sum found in Table 5.15. We find that while the default cuts are not at the optimal total quadrature uncertainty, they are only about 2% different, and the ideal value has includes a nearly five-fold increase in the number of impure events included (see Fig. 4.9).

Cuts	$\sigma_{a_2}^{\text{stat}}$ 10^{-2}	$\sigma_{a_2}^{\text{sys imp}}$ 10^{-2}	$\sigma_{a_2}^{\text{total quad sum}}$ 10^{-2}	$\sigma_{b_2}^{\text{stat}}$ 10^{-2}	$\sigma_{b_2}^{\text{sys imp}}$ 10^{-2}	$\sigma_{b_2}^{\text{total quad sum}}$ 10^{-2}
Default Cuts	1.563	0.005	1.563	1.227	0.078	1.230
$E^{\text{3rd Shwr}} < 18\,\text{MeV}$	1.630	0.034	1.631	1.277	0.089	1.28
$E^{\text{3rd Shwr}} < 50\,\text{MeV}$	1.537	0.128	1.543	1.208	0.224	1.228
$\chi^2_{\text{k.f.}} < 10$	1.616	0.023	1.616	1.265	0.052	1.266
$\chi^2_{\text{k.f.}} < 30$	1.528	0.119	1.533	1.201	0.096	1.205
χ_c mass $\pm 10\,\text{MeV}$	1.605	0.033	1.606	1.261	0.023	1.261
χ_c mass $\pm 20\,\text{MeV}$	1.548	0.068	1.55	1.216	0.125	1.223
$\lvert\cos\theta_{\text{lab,ph}}^{\text{barrel}}\rvert < 0.77$	1.608	0.013	1.608	1.26	0.067	1.262
$\lvert\cos\theta_{\text{lab,ph}}^{\text{barrel}}\rvert < 0.80$	1.547	0.017	1.547	1.215	0.076	1.218

5.8 Cut Variations with `data42`

After looking at the effect of variations of cuts on an ensemble of tests using the "signal" data selected from phase space MC via the rejection method, we looked at the actual effect of performing fits to `data42` after making various selection criteria. These results show how sensitive the actual data were to the underlying cuts we chose. For the $J_\chi = 1$ case shown in Table 5.17, we perform the fits using the various selection criteria, and then correct for the impurity bias (found in Table 5.13 in the result of the difference column). We then use look at the ensemble of bias corrected data fits and assign a systematic uncertainty using the standard deviation of the fitted results over the 7 different types of selection criteria investigated. We find that there is a systematic uncertainty of $(0.10, 0.30) \times 10^{-2}$ for $(a_2^{J=1}, b_2^{J=1})$ in performing fits to data.

For the $J_\chi = 2$ case, we follow the same procedure except that we do not correct for impurity biases before calculating the systematic uncertainty. The reason we do not correct for the impurity bias is that the impurity bias in all cases less than 1/10 the statistical uncertainty, so any correction would be of very little significance. We find in this case that we have systematic uncertainties of $(0.4, 0.3) \times 10^{-2}$ for (a_2, b_2) when performing the two-parameter fit with $(a_3 \equiv b_3 \equiv 0)$. Values from other fits are given in the appropriate appendices.

Table 5.17: Systematic uncertainties from selection criteria variations for $J_\chi = 1$ two-parameter (a_2, b_2) fit performed on data. We find for all sets of selection criteria considered that there's a systematic uncertainty of $(0.19, 0.22) \times 10^{-2}$ for (a_2, b_2) respectively over the variation of the criteria considered.

Cuts	$a_2^{\text{bias cor}}$	$b_2^{\text{bias cor}}$
	10^{-2}	10^{-2}
Default Cuts	$-6.26 \pm 0.63 \pm 0.08$	$2.76 \pm 0.73 \pm 0.03$
$E^{\text{3rd Shwr}} < 18\,\text{MeV}$	$-6.43 \pm 0.64 \pm 0.04$	$2.67 \pm 0.73 \pm 0.03$
$E^{\text{3rd Shwr}} < 50\,\text{MeV}$	$-5.73 \pm 0.60 \pm 0.16$	$2.45 \pm 0.72 \pm 0.07$
$\chi^2_{\text{k.f.}} < 10$	$-6.23 \pm 0.65 \pm 0.03$	$2.33 \pm 0.75 \pm 0.02$
$\chi^2_{\text{k.f.}} < 30$	$-6.30 \pm 0.61 \pm 0.15$	$3.10 \pm 0.71 \pm 0.03$
χ_c mass $\pm 10\,\text{MeV}$	$-6.36 \pm 0.65 \pm 0.06$	$2.85 \pm 0.75 \pm 0.02$
χ_c mass $\pm 20\,\text{MeV}$	$-6.10 \pm 0.62 \pm 0.09$	$2.78 \pm 0.69 \pm 0.05$
$\lvert\cos\theta^{\text{barrel}}_{\text{lab,ph}}\rvert < 0.77$	$-6.18 \pm 0.65 \pm 0.08$	$2.97 \pm 0.75 \pm 0.04$
$\lvert\cos\theta^{\text{barrel}}_{\text{lab,ph}}\rvert < 0.80$	$-6.17 \pm 0.62 \pm 0.08$	$2.73 \pm 0.72 \pm 0.04$
Ensemble	-6.20 ± 0.19	2.74 ± 0.22

Table 5.18: Systematic uncertainties from selection criteria variations for $J_\chi = 2$ two-parameter (a_2, b_2) fit performed on data. We find for all sets of selection criteria considered that there's a systematic uncertainty of $(0.4, 0.3) \times 10^{-2}$ for (a_2, b_2) respectively over the variation of the criteria considered.

Cuts	a_2	b_2
	10^{-2}	10^{-2}
Default Cuts	-9.3 ± 1.6	1.0 ± 1.3
$E^{\text{3rd Shwr}} < 18\,\text{MeV}$	-9.4 ± 1.6	0.6 ± 1.3
$E^{\text{3rd Shwr}} < 50\,\text{MeV}$	-9.8 ± 1.6	0.5 ± 1.3
$\chi^2_{\text{k.f.}} < 10$	-9.1 ± 1.6	1.3 ± 1.3
$\chi^2_{\text{k.f.}} < 30$	-9.5 ± 1.5	0.4 ± 1.2
χ_c mass $\pm 10\,\text{MeV}$	-8.7 ± 1.6	1.0 ± 1.3
χ_c mass $\pm 20\,\text{MeV}$	-9.8 ± 1.5	0.8 ± 1.3
$\lvert\cos\theta^{\text{barrel}}_{\text{lab,ph}}\rvert < 0.77$	-9.6 ± 1.6	1.2 ± 1.3
$\lvert\cos\theta^{\text{barrel}}_{\text{lab,ph}}\rvert < 0.80$	-9.5 ± 1.5	1.3 ± 1.3
Ensemble	-9.4 ± 0.3	0.9 ± 0.3

5.9 Summary of Systematic Uncertainties and Biases

5.9.1 $J_\chi = 1$

The systematic uncertainties and biases for $J_\chi = 1$ are summarized in Table 5.19. We find that the total systematic uncertainty is $(0.38, 0.31) \times 10^{-2}$ for $(a_2^{J=1}, b_2^{J=1})$ respectively.

Table 5.19: Table of systematic uncertainties and biases for $J_\chi = 1$ two-parameter fit. The total systematic uncertainty is the quadrature sum of systematic uncertainties. The statistical uncertainty from the data fits is given for comparison.

	$a_2^{J_\chi=1}$		$b_2^{J=1}$	
Source of systematic	Uncertainty $\times 10^{-2}$	Bias $\times 10^{-2}$	Uncertainty $\times 10^{-2}$	Bias $\times 10^{-2}$
Generic MC impurities	0.15	0.15	0.05	0.05
Selection criteria	0.19	-	0.22	-
Total systematic uncertainty	0.24	0.15	0.23	0.05
Statistical Uncertainty	0.63	-	0.73	-

5.9.2 $J_\chi = 2$

The systematic uncertainties for the $J_\chi = 2$ two-parameter fit (a_2, b_2) are summarized in Table 5.20. We do not find any systematic biases for the $J_\chi = 2$ case.

Table 5.20: Table of systematic uncertainties for $J_\chi = 2$ two-parameter (a_2, b_2) fit. The total systematic uncertainty is the quadrature sum of systematic uncertainties. The statistical uncertainty from the data fits is given for comparison.

Systematic uncertainty	$a_2^{J=2}$ $\times 10^{-2}$	$b_2^{J=2}$ $\times 10^{-2}$
Generic MC impurities	0.04	0.07
Selection criteria	0.33	0.33
Total systematic uncertainty	0.3	0.3
Statistical uncertainty	1.6	1.3

Table 5.21: Table of systematic uncertainties for $J_\chi = 2$ three-parameter (a_2, b_2, b_3) fit. The total systematic is the quadrature sum of systematic uncertainties. The statistical uncertainty from the data fits is given for comparison.

Systematic uncertainty	$a_2^{J=2}$ $\times 10^{-2}$	$b_2^{J=2}$ $\times 10^{-2}$	$b_3^{J=2}$ $\times 10^{-2}$
Generic MC impurities	0.04	0.07	0.03
Selection criteria	0.33	0.34	0.20
Total systematic uncertainty	0.3	0.3	0.2
Statistical uncertainty	1.6	1.4	1.2

Table 5.22: Table of systematic uncertainties for $J_\chi = 2$ two-parameter (a_2, b_3) fixed-a_2/b_2-ratio fit. The total systematic is the quadrature sum of systematic uncertainties. The statistical uncertainty from the data fits is given for comparison.

Systematic uncertainty	$a_2^{J=2}$ $\times 10^{-2}$	$b_3^{J=2}$ $\times 10^{-2}$
Generic MC impurities	0.04	0.04
Selection criteria	0.34	0.23
Total systematic	0.3	0.2
Statistical uncertainty	1.6	1.1

Table 5.23: Table of systematic uncertainties for $J_\chi = 2$ four-parameter (a_2, b_2, a_3, b_3) fit. The total systematic uncertainty is the quadrature sum of systematic uncertainties. The statistical uncertainty from the data fits is given for comparison.

Systematic uncertainty	$a_2^{J=2}$ $\times 10^{-2}$	$b_2^{J=2}$ $\times 10^{-2}$	$a_3^{J=2}$ $\times 10^{-2}$	$b_3^{J=2}$ $\times 10^{-2}$
Generic MC impurities	0.06	0.08	0.08	0.03
Selection criteria	0.24	0.39	0.28	0.20
Total systematic	0.3	0.4	0.3	0.2
Statistical uncertainty	1.9	1.5	1.4	1.2

5.10 Check $J_\chi = 0$ decays are pure E1 (Not Performed)

By conservation of angular momentum, the transitions $\psi' \to \gamma' \chi_{c0}$ and $\chi_{c0} \to \gamma J/\psi$ must be pure E1. In principle, this could be an excellent test for any overall biases in our analysis as we know that the M2 and E3 amplitudes are zero. However this was not performed for several reasons.

First, all tests for $J_\chi = 0$ will suffer due to poor statistics and difficult-to-identify signal decays. Due to the significantly lower branching fraction of $\chi_{c0} \to \gamma J/\psi$ ($\mathcal{B}[\chi_{c0} \to \gamma J/\psi] = (1.28 \pm 0.11) \times 10^{-2}$) compared with the branching fractions for $\chi_{(c1,c2)} \to \gamma J/\psi$ ($\mathcal{B}[\chi_{c1} \to \gamma J/\psi] = (36.0 \pm 1.9) \times 10^{-2}$ and $\mathcal{B}[\chi_{c2} \to \gamma J/\psi] = (20.0 \pm 1.0) \times 10^{-2}$), we expect significantly smaller numbers of signal decays through $J_\chi = 0$ than we do for $J_\chi = 1, 2$. The overall signal branching fraction for $J_\chi = 0$ signal decays is 26.3 ± 3.1 and 13.8 ± 1.6 times smaller than the $J_\chi = 1$ and $J_\chi = 2$ signal decays, respectively, so it is less sensitive due to the considerably smaller signal size [3]. While the energy difference between the photons for $J_\chi = 1$ and $J_\chi = 2$ signal decays are well separated ($E_\gamma^{J_\chi=1} = 389\,\text{MeV}, E_{\gamma'}^{J_\chi=1} = 171\,\text{MeV}; E_\gamma^{J_\chi=2} = 430\,\text{MeV}, E_{\gamma'}^{J_\chi=2} = 128\,\text{MeV}$), the energy difference between the two photons in $J_\chi = 0$ signal decays is much smaller ($E_\gamma^{J_\chi=0} = 303\,\text{MeV}, E_{\gamma'}^{J_\chi=0} = 261\,\text{MeV}$). The

photons are identified as being γ or γ' based on γ having a greater shower energy than γ', so the smaller energy difference will result in misidentified signal events. The kinematic fits to the J/ψ mass and ψ' four-vector and cuts on the χ_{c0} mass should reduce this misidentification rate, but the efficiency may be lowered.

The PDF for $J_\chi = 0$, Eq. (2.6) simplifies to

$$W(\theta', \phi', \theta_{\gamma\gamma'}, \theta, \phi) \quad \propto \quad B_0 B_0 A_0 A_0 (1 + \cos^2\theta')(1 + \cos^2\theta)$$

which does not have any amplitudes (parameters) to fit for (the only amplitudes are contained in the normalization). This is expected as M2 and E3 amplitudes are forbidden by conservation of angular momentum.

We could perform a two-parameter fit for unphysical variables (α, β) in a generalized PDF:

$$W(\theta', \phi', \theta_{\gamma\gamma'}, \theta, \phi) \quad \propto \quad (1 + \alpha\cos^2\theta')(1 + \beta\cos^2\theta)$$

to ensure that we find $\alpha = \beta = 1$ to recover the true PDF. However, this is a poor comparison to the actual analysis as the PDF only depends on two angles (θ', θ), so it is less sensitive than the full five-angle fit. Toy MC fits find $\alpha = 0.98 \pm 0.16$ and $\beta = 1.02 \pm 0.17$ after an ensemble of 100 trials with data samples of the expected size (3400 events at 40% efficiency).

We could also potentially use a mixed form of the $J_\chi = 0$ and $J_\chi = 1$ or $J_\chi = 2$ PDFs to fit for a more realistic angular distribution. This would involve fitting for (a_2, b_2) in a distribution like:

$$W \quad \equiv \quad W_{J_\chi=0} + W_{J_\chi=1}(a_2, b_2) - W_{J_\chi=1}(a_2 = 0, b_2 = 0) \tag{5.1}$$

This would be more sensitive than the (α, β) fit described above; however, tests of this sort have not been performed either. As the definition for the PDFs $W(\Omega; \mathbb{A})$

in Eq. (2.6) are not normalized, problems potentially could arise from the addition of PDFs with different normalizations.

CHAPTER 6

CONCLUSIONS

6.1 $J_\chi = 1$

The results of our bias-corrected fits with systematic uncertainties for $J_\chi = 1$ are with the two-parameter fit is:

$$a_2^{J=1} = (-6.26 \pm 0.63 \pm 0.24) \times 10^{-2}$$
$$b_2^{J=1} = (2.76 \pm 0.73 \pm 0.23) \times 10^{-2}.$$

6.2 $J_\chi = 2$

The results with statistical uncertainty for our fits the $J_\chi = 2$ fits are, for the $J_\chi = 2$ two-parameter (a_2, b_2) fit:

$$a_2^{J=2} = (-9.3 \pm 1.6 \pm 0.3) \times 10^{-2}$$
$$b_2^{J=2} = (1.0 \pm 1.3 \pm 0.3) \times 10^{-2}$$
$$a_3^{J=2} \equiv 0$$
$$b_3^{J=2} \equiv 0,$$

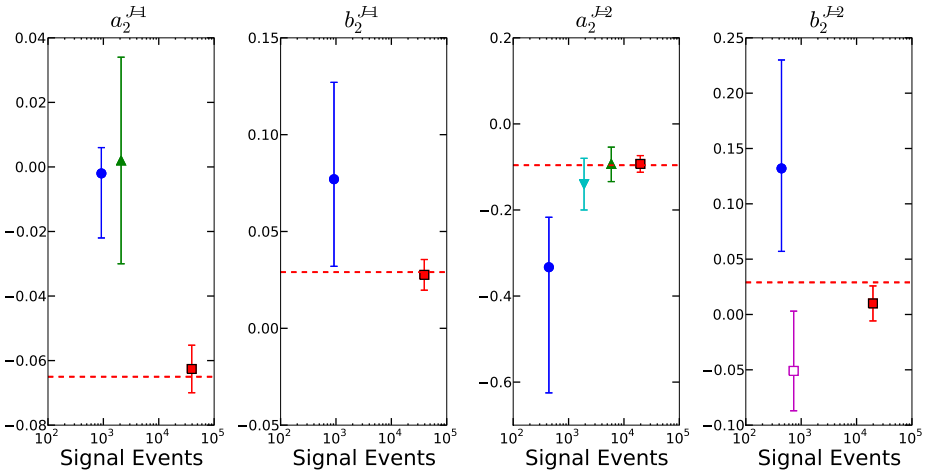

Figure 6.1: Experimental values of the magnetic quadrupole amplitudes from this analysis compared with previous experimental values and theoretical expectations. CLEO-c results from this analysis are solid red squares (■), Crystal Ball results are blue circles (●) [29], the E760 result is a cyan inverted triangle (▼) [4], the E835 results are green triangles (▲) [2], the BESII result is a purple open square (□) [1], and the theoretical expectation given by Eqs. (2.15-2.18) with $m_c = 1.5\,\mathrm{GeV}$ and $\kappa_c = 0$ is a dashed red line (- - -).

for the $J_\chi = 2$ three-parameter (a_2, b_2, b_3) fit:

$$a_2^{J=2} = (-9.3 \pm 1.6 \pm 0.3) \times 10^{-2}$$

$$b_2^{J=2} = (0.7 \pm 1.4 \pm 0.3) \times 10^{-2}$$

$$a_3^{J=2} \equiv 0$$

$$b_3^{J=2} = (-0.8 \pm 1.2 \pm 0.2) \times 10^{-2},$$

for the $J_\chi = 2$ two-parameter (a_2, b_3) fixed-a_2/b_2-ratio fit:

$$\begin{aligned} a_2^{J=2} &= (-9.2 \pm 1.6 \pm 0.3) \times 10^{-2} \\ b_2^{J=2} &\equiv -\frac{a_2^{J=2}}{3.367} = (2.7 \pm 0.5 \pm 0.1) \times 10^{-2} \\ a_3^{J=2} &\equiv 0 \\ b_3^{J=2} &= (-0.1 \pm 1.1 \pm 0.2) \times 10^{-2}, \end{aligned}$$

and for the $J_\chi = 2$ four-parameter (a_2, b_2, a_3, b_3) fit:

$$\begin{aligned} a_2^{J=2} &= (-7.9 \pm 1.9 \pm 0.3) \times 10^{-2} \\ b_2^{J=2} &= (0.2 \pm 1.5 \pm 0.4) \times 10^{-2} \\ a_3^{J=2} &= (1.7 \pm 1.4 \pm 0.3) \times 10^{-2} \\ b_3^{J=2} &= (-0.8 \pm 1.2 \pm 0.2) \times 10^{-2}, \end{aligned}$$

6.3 m_c and κ_c Independent Ratios

Using the results from the $J_\chi = 2$ two-parameter (a_2, b_2) fit and the results from the $J_\chi = 1$ fits, we find the following ratios that compare very well with the theoretical predictions:

$$\begin{aligned} \left(\frac{a_2^{J=1}}{a_2^{J=2}}\right)_{\rm CLEO} &= 0.67^{+0.16}_{-0.12} \stackrel{?}{=} \left(\frac{a_2^{J=1}}{a_2^{J=2}}\right)_{\rm th} = 0.676 \pm 0.071 \\ \left(\frac{a_2^{J=1}}{b_2^{J=1}}\right)_{\rm CLEO} &= -2.27^{+0.54}_{-0.92} \stackrel{?}{=} \left(\frac{a_2^{J=1}}{b_2^{J=1}}\right)_{\rm th} = -2.27 \pm 0.16 \\ \left(\frac{b_2^{J=1}}{b_2^{J=2}}\right)_{\rm CLEO} &= 1.5^{+3.0}_{-4.0} \stackrel{?}{=} \left(\frac{b_2^{J=1}}{b_2^{J=2}}\right)_{\rm th} = 1.000 \pm 0.015 \\ \left(\frac{a_2^{J=2}}{b_2^{J=2}}\right)_{\rm CLEO} &= -5.2^{+14}_{-10} \stackrel{?}{=} \left(\frac{b_2^{J=1}}{b_2^{J=2}}\right)_{\rm th} = -3.37 \pm 0.28 \ . \end{aligned}$$

Table 6.1: Split dataset results for two parameter fits. Each dataset is of equal size and contains independent events that are randomly selected from the full dataset. For $J_\chi = 1$ we perform only the two-parameter fit (a_2, b_2). For $J_\chi = 2$, we perform the two-parameter fit $(a_2, b_2, a_3 \equiv 0, b_3 \equiv 0)$, three-parameter fit $(a_2, b_2, b_3, a_3 \equiv 0)$, two-parameter fixed-ratio fit $(a_2, b_3, b_2 \equiv -a_2/3.367, a_3 \equiv 0)$, and four-parameter fit (a_2, b_2, a_3, b_3), respectively. The uncertainties listed are only statistical, though the systematic uncertainties should also be the same as the full dataset case.

Fit Result	a_2 $\times 10^{-2}$	b_2 $\times 10^{-2}$	a_3 $\times 10^{-2}$	b_3 $\times 10^{-2}$
$J_\chi = 1$ A	-7.00 ± 0.89	2.99 ± 1.03	-	-
$J_\chi = 1$ B	-5.25 ± 0.89	2.63 ± 1.03	-	-
$J_\chi = 2$ A (a_2, b_2)	-9.2 ± 2.2	-0.7 ± 1.8	0	0
$J_\chi = 2$ B (a_2, b_2)	-9.5 ± 2.2	2.7 ± 1.8	0	0
$J_\chi = 2$ A (a_2, b_2, b_3)	-9.2 ± 2.2	-0.7 ± 2.0	0	-0.1 ± 1.7
$J_\chi = 2$ B (a_2, b_2, b_3)	-9.4 ± 2.2	2.1 ± 1.9	0	-1.4 ± 1.7
$J_\chi = 2$ A (a_2, b_3)	-8.9 ± 2.2	2.7 ± 0.6	0	1.0 ± 1.6
$J_\chi = 2$ B (a_2, b_3)	-9.4 ± 2.2	2.8 ± 0.7	0	-1.2 ± 1.6
$J_\chi = 2$ A (a_2, b_2, a_3, b_3)	-7.0 ± 2.5	-1.5 ± 2.0	2.7 ± 1.9	-0.0 ± 1.7
$J_\chi = 2$ B (a_2, b_2, a_3, b_3)	-8.9 ± 2.8	1.9 ± 2.0	0.6 ± 2.9	-1.4 ± 1.7

6.4 Split Dataset Check

The ratios $a_2^{J=1}/a_2^{J=2}$ and $a_2^{J=1}/b_2^{J=1}$ agree with the theory value almost exactly, despite having significant uncertainties. To test that this is a random statistical occurrence as opposed to some undetected bias of our method, we split the dataset into two equally sized datasets of half-size labeled A and B. The results of these split dataset test are shown in Table 6.1.

These lead to the ratios using the values from the two-parameter fits as before

(and only the statistical uncertainty):

$$\left(\frac{a_2^{J=1}}{a_2^{J=2}}\right)_{\mathrm{A}} = 0.78^{+0.27}_{-0.17} \stackrel{?}{=} \left(\frac{a_2^{J=1}}{a_2^{J=2}}\right)_{\mathrm{th}} = 0.676 \pm 0.071$$
$$\left(\frac{a_2^{J=1}}{a_2^{J=2}}\right)_{\mathrm{B}} = 0.57^{+0.20}_{-0.14} \stackrel{?}{=} \left(\frac{a_2^{J=1}}{a_2^{J=2}}\right)_{\mathrm{th}} = 0.676 \pm 0.071$$
$$\left(\frac{a_2^{J=1}}{b_2^{J=1}}\right)_{\mathrm{A}} = -2.42^{+0.68}_{-1.35} \stackrel{?}{=} \left(\frac{a_2^{J=1}}{b_2^{J=1}}\right)_{\mathrm{th}} = -2.27 \pm 0.16$$
$$\left(\frac{a_2^{J=1}}{b_2^{J=1}}\right)_{\mathrm{B}} = -2.08^{+0.66}_{-1.41} \stackrel{?}{=} \left(\frac{a_2^{J=1}}{b_2^{J=1}}\right)_{\mathrm{th}} = -2.27 \pm 0.16 \ .$$

These ratios still agree very well with theory, though show the expected statistical fluctuation from the central value. In calculating these ratios, we applied the correction for the same systematic biases that were found using generic MC for the $J_\chi = 1$ case. The results of all the fits from the split-dataset samples in Table 6.1 are consistent with each other to the degree expected from the statistical uncertainties.

6.5 κ_c Calculation

Our most sensitive measurement of a magnetic quadrupole amplitude is our measurement of $a_2^{J=1}$. From theory, we know that

$$a_2^{J=1} = -\frac{E_\gamma}{4m_c}(1+\kappa_c) = (1+\kappa_c)/\xi$$

where we defined $1/\xi$ to be the proportionality between $1+\kappa_c$ and $a_2^{J=1}$, where κ_c is the anomalous magnetic moment of the charm quark. If we use $m_c = 1.5 \pm 0.3$, we find that ξ is

$$\xi \equiv -\frac{4m_c}{E_\gamma} = -14.0 \pm 2.8 \pm 0.9 \tag{6.1}$$

where the two uncertainties for ξ are the theoretical uncertainty due to m_c and the second is the theoretical uncertainty due to second order corrections of size

$(E_\gamma/m_c)^2$.

$$1 + \kappa_c = \xi a_2^{J=1} = 0.877 \pm 0.088 \pm 0.034 \pm 0.175 \pm 0.059 \ , \qquad \text{or} \tag{6.2}$$

$$\kappa_c = -0.123 \pm 0.088 \pm 0.034 \pm 0.175 \pm 0.059 \tag{6.3}$$

where we list the result, the statistical uncertainty, the systematic uncertainty, the theoretical uncertainty from the uncertainty in the charm quark mass (using $m_c = 1.5 \pm 0.3$) and the theoretical uncertainty from second order correction (where we assigned a fractional uncertainty of order $(E_\gamma/m_c)^2$ to ξ). Due to the large theoretical uncertainty, our result is consistent with a vanishing anomalous magnetic moment of the charm quark, $\kappa_c \approx 0$.

6.6 Summary

In this analysis we measure a significantly non-zero magnetic quadrupole amplitude for the transitions $\chi_{c1} \to \gamma J/\psi$, $\chi_{c2} \to \gamma J/\psi$, and $\psi' \to \gamma' \chi_{c1}$. The results of our fits to these three amplitudes all agree with the first order $\kappa_c = 0$, $m_c = 1.5\,\text{GeV}$ theoretical prediction given by Eqs. (2.15 - 2.18) to better than 1σ. For the last transition $\psi' \to \gamma' \chi_{c2}$, we initially expected that we will have the lowest sensitivity for measuring an M2 amplitude due to $E'_\gamma < E_\gamma$ and the small number of $J_\chi = 2$ events observed. We found a result for an M2 amplitude for $\psi' \to \gamma' \chi_{c2}$ that is approximately 1 σ away from both the pure E1 result and the theoretical expectation if $\kappa_c = 0$ when we perform a fit that fixes $a_3 = 0$ (as theory strongly suggests) and do not fix the ratio between a_2/b_2 (in which case we observe a find a significant M2 amplitude even for this case). The non-zero M2 amplitude can be easily observed in the transitions $\chi_{(c1,c2)} \to \gamma J/\psi$ by looking at $\cos\theta$ histograms for the data and one angle projections of a pure E1 distribution and the distribution

selected with the fitted values as shown in Figures 4.18 and 4.22, the variable that was *a priori* predicted to be the angle most sensitive to M2 amplitudes [34]. We found that for the $J_\chi = 1$ and $J_\chi = 2$ transitions that our fitted results differed from the pure E1 value by more than 11σ and 6σ, respectively. We found no significant evidence for a non-zero electric octupole transition amplitude in the $J_\chi = 2$ as theory predicts in the absence of a large D admixture in the ψ states (or a large F admixture in the χ_{c2} state).

APPENDIX A

THREE-PARAMETER FIT (a_2, b_2, b_3) WITH $a_3 = 0$

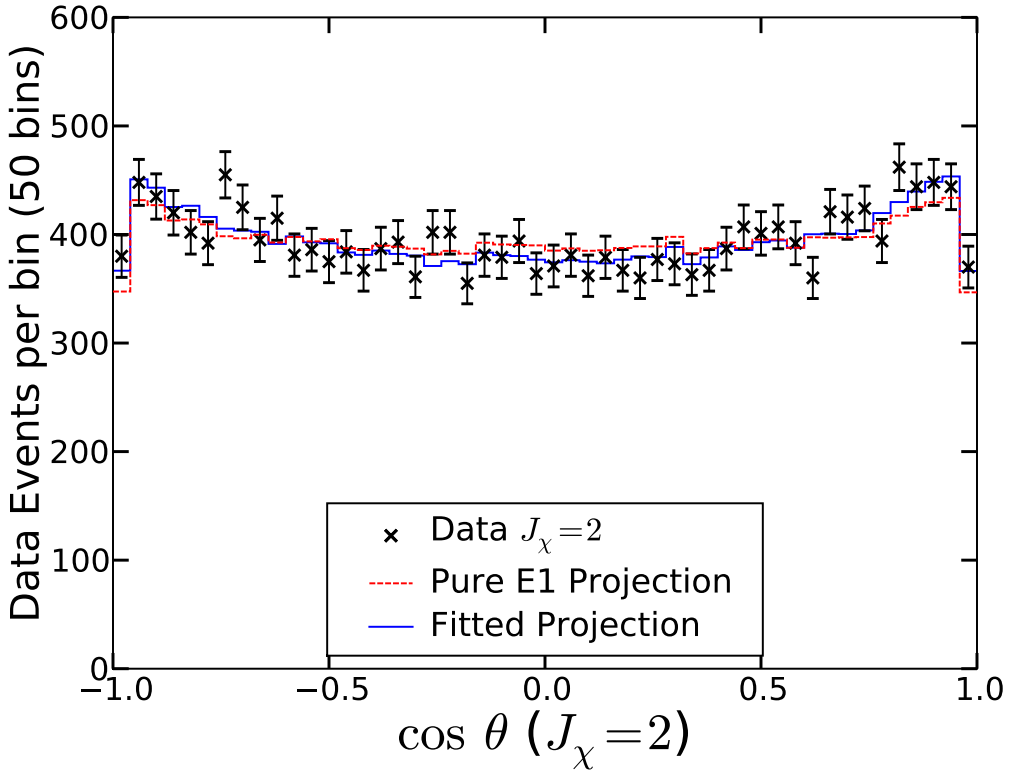

Figure A.1: $J_\chi = 2$ data vs projections for $\cos\theta$. The reduced chi square ($\chi^2/N_{\text{d.o.f.}}$) for the 50 bin histogram of the data to come from the same distribution as the fitted projection (holding $a_3 \equiv b_3 \equiv 0$) is $36.9/46 = 0.80$, and the reduced chi square for data to come from pure E1 is $53.1/49 = 1.08$. The fitted projection corresponds to the three-parameter fit $(a_2, b_2, b_3) = (-0.093, 0.007, -0.008)$ with $a_3 \equiv 0$, which is 6.3σ from pure E1.

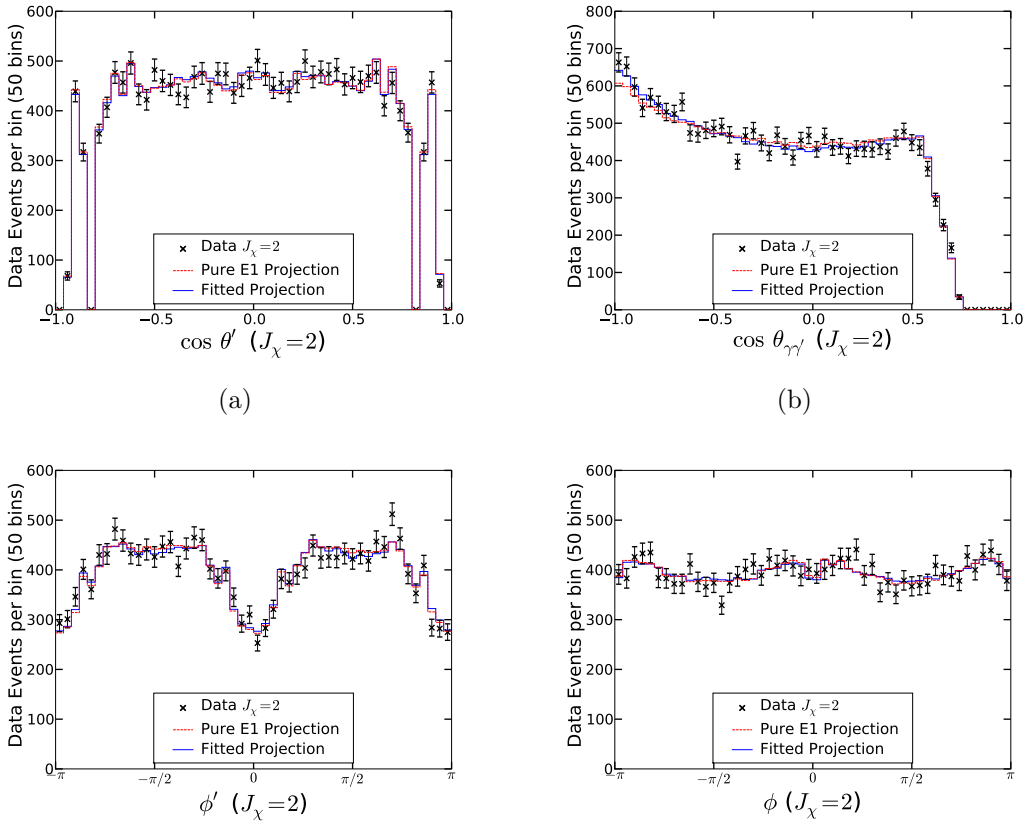

Figure A.2: $J_\chi = 2$ data vs projections for $\cos\theta', \cos\theta_{\gamma\gamma'}, \phi', \phi$. The reduced $\chi^2/N_{\text{d.o.f.}}$ comparing the 50 bin histogram of the data to the fitted projection are $36.5/46 = 0.79$, $50.3/46 = 1.09$, $47.6/46 = 1.04$, and $45.76/46 = 1.00$, while the $\chi^2/N_{\text{d.o.f.}}$ comparing data to the pure E1 projection are $38.89/49 = 0.79$, $59.8/49 = 1.22$, $50.6/49 = 1.03$, and $45.0/49 = 0.92$ for $\cos\theta', \cos\theta_{\gamma\gamma'}, \phi'$, and ϕ, respectively. The fitted projection corresponds to the three-parameter fit $(a_2, b_2, b_3) = (-0.093, 0.007, -0.008)$ with $a_3 \equiv 0$, which is 6.3σ from pure E1.

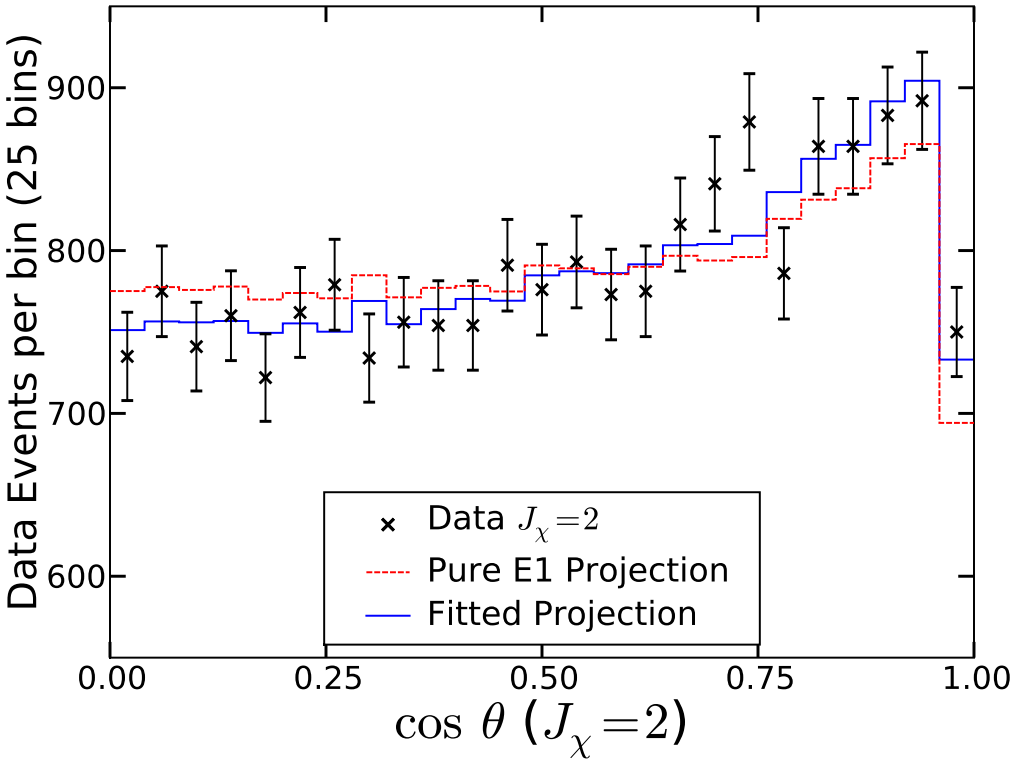

Figure A.3: $J_\chi = 2$ projection of $\cos\theta$ after using parity transformations to fold dataset into positive $\cos\theta', \phi', \cos\theta_{\gamma\gamma'}, \cos\theta$. The reduced χ^2 for the 25 bin histogram describing the data to correspond with the fitted projection and the pure E1 projection are $20.1/21 = 0.96$ and $35.5/24 = 1.48$, respectively. The fitted projection corresponds to the three-parameter fit $(a_2, b_2, b_3) = (-0.093, 0.007, -0.008)$ with $a_3 \equiv 0$, which is 6.3σ from pure E1.

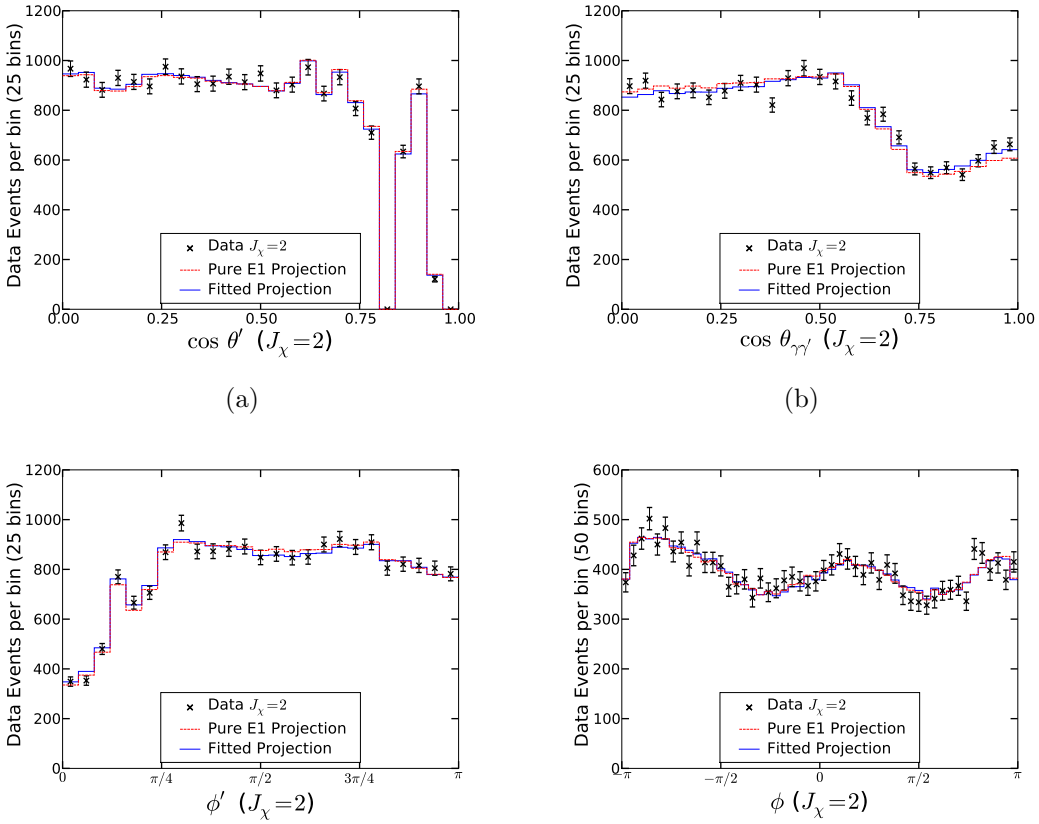

Figure A.4: $J_\chi=2$ projections for $\cos\theta', \cos\theta_{\gamma\gamma'}, \phi', \phi$ after using parity transformation to fold the dataset into positive $\cos\theta', \phi', \cos\theta_{\gamma\gamma'}, \cos\theta$. The $\chi^2/N_{\text{d.o.f.}}$ comparing the 25 bin (50 bins for ϕ) histogram of the data to the fitted projection are $15.8/21 = 0.75$, $33.6/21 = 1.60$, $18.1/21 = 0.86$, and $56.1/46 = 1.22$, while the reduced χ^2 comparing data to the pure E1 projection are $17.7/24 = 0.74$, $43.2/24 = 1.80$, $21.3/24 = 0.89$, and $53.3/49 = 1.09$ for $\cos\theta', \cos\theta_{\gamma\gamma'}, \phi'$, and ϕ, respectively. The fitted projection corresponds to the three-parameter fit $(a_2, b_2, b_3) = (-0.093, 0.007, -0.008)$ with $a_3 \equiv 0$, which is 6.3σ from pure E1.

Table A.1: Systematic tests varying the number of phase space Monte Carlo events used in calculating the efficiency integrals for $J_\chi = 2$ three-parameter fit. The quoted phase space data size are after applying all the selection criteria. There are no impurity events present in the data sample being fit.

PHSP size (After cuts)	$\langle a_2 \rangle$ 10^{-2}	$\sigma^{\rm ens}_{a_2}$ 10^{-2}	$\langle \sigma^{\rm fit}_{a_2} \rangle$ 10^{-2}	$\Delta_{\langle a_2 \rangle}$ $\sigma_{\langle a_2 \rangle}$	$\langle b_2 \rangle$ 10^{-2}	$\sigma^{\rm ens}_{b_2}$ 10^{-2}	$\langle \sigma^{\rm fit}_{b_2} \rangle$ 10^{-2}	$\Delta_{\langle b_2 \rangle}$ $\sigma_{\langle b_2 \rangle}$
3000	-10.3	3.9	1.5	-3.0	2.2	3.6	1.3	-3.3
10000	-9.5	2.4	1.5	0.3	3.0	2.3	1.3	0.5
30000	-9.5	1.6	1.5	0.3	3.0	1.7	1.3	0.4
100000	-9.5	1.5	1.5	0.4	3.0	1.4	1.3	0.6
300000	-9.5	1.4	1.5	0.4	3.1	1.3	1.3	0.8
1759617	-9.7	1.4	1.5	-0.6	3.0	1.4	1.3	0.7
Input	-9.6				2.9			
PHSP size (After cuts)	$\langle a_3 \rangle$ 10^{-2}	$\sigma^{\rm ens}_{a_3}$ 10^{-2}	$\langle \sigma^{\rm fit}_{a_3} \rangle$ 10^{-2}	$\Delta_{\langle a_3 \rangle}$ $\sigma_{\langle a_3 \rangle}$	$\langle b_3 \rangle$ 10^{-2}	$\sigma^{\rm ens}_{b_3}$ 10^{-2}	$\langle \sigma^{\rm fit}_{b_3} \rangle$ 10^{-2}	$\Delta_{\langle b_3 \rangle}$ $\sigma_{\langle b_3 \rangle}$
3000	0				1.1	2.5	1.1	5.8
10000	0				0.1	1.8	1.1	0.8
30000	0				0.1	1.4	1.1	0.7
100000	0				0.1	1.1	1.1	0.4
300000	0				0.1	1.0	1.1	0.4
1759617	0				0.1	1.0	1.1	0.4
Input	0				0			

Table A.2: Systematic tests from including non-signal generic Monte Carlo events selected by the selection criteria for $J_\chi = 2$ three-parameter fit. We find that the impurities add a negligible systematic uncertainty when compared to the statistical uncertainty. Refer to Section 5.4.

Type	$\langle a_2 \rangle$ 10^{-2}	$\sigma^{\rm ens}_{a_2}$ 10^{-2}	$\langle \sigma^{\rm fit}_{a_2} \rangle$ 10^{-2}	$\Delta_{\langle a_2 \rangle}$ $\sigma_{\langle a_2 \rangle}$	$\langle b_2 \rangle$ 10^{-2}	$\sigma^{\rm ens}_{b_2}$ 10^{-2}	$\langle \sigma^{\rm fit}_{b_2} \rangle$ 10^{-2}	$\Delta_{\langle b_2 \rangle}$ $\sigma_{\langle b_2 \rangle}$
Pure	-9.8	1.4	1.6	-0.6	3.0	1.3	1.3	0.7
Diff. (A)	-0.001	0.007			0.055	0.005		
Diff. (B)	0.081	0.004			-0.017	0.005		
Diff. (C)	-0.008	0.011			0.151	0.005		
Diff. (D)	0.025	0.004			-0.068	0.005		
Diff. (E)	-0.039	0.002			0.015	0.005		
Diff. (A-E)	0.057	0.021			0.134	0.018		
Input	-9.6				2.9			
$\langle$Imp. Bias$\rangle$	0.01	0.04			0.03	0.07		

Type	$\langle a_3 \rangle$ 10^{-2}	$\sigma^{\rm ens}_{a_3}$ 10^{-2}	$\langle \sigma^{\rm fit}_{a_3} \rangle$ 10^{-2}	$\Delta_{\langle a_3 \rangle}$ $\sigma_{\langle a_3 \rangle}$	$\langle b_3 \rangle$ 10^{-2}	$\sigma^{\rm ens}_{b_3}$ 10^{-2}	$\langle \sigma^{\rm fit}_{b_3} \rangle$ 10^{-2}	$\Delta_{\langle b_3 \rangle}$ $\sigma_{\langle b_3 \rangle}$
Pure	0				0.1	1.0	1.2	0.3
Diff. (A)	0				-0.061	0.004		
Diff. (B)	0				-0.013	0.004		
Diff. (C)	0				0.006	0.003		
Diff. (D)	0				-0.068	0.005		
Diff. (E)	0				-0.031	0.005		
Diff. (A-E)	0				-0.145	0.016		
Input	0				0			
$\langle$Imp. Bias$\rangle$	0				-0.03	0.02		

Table A.3: Systematic uncertainties from final state radiation (FSR) for $J_\chi = 2$ three-parameter fit. We performed $N = 32$ pre-FSR and $N = 28$ post-FSR trials with exactly 20000 data events in each fit. Each trial had a five-angle two-parameter fit performed with $W(\Omega; \mathbb{A}_0)$ with $\mathbb{A} = (-0.096, 0.029, 0, 0)$.

Type	$\langle a_2 \rangle$ 10^{-2}	$\sigma^{\text{ens}}_{a_2}$ 10^{-2}	$\langle \sigma^{\text{fit}}_{a_2} \rangle$ 10^{-2}	$\Delta_{\langle a_2 \rangle}$ $\sigma_{\langle a_2 \rangle}$	$\langle b_2 \rangle$ 10^{-2}	$\sigma^{\text{ens}}_{b_2}$ 10^{-2}	$\langle \sigma^{\text{fit}}_{b_2} \rangle$ 10^{-2}	$\Delta_{\langle b_2 \rangle}$ $\sigma_{\langle b_2 \rangle}$	N
Pre-FSR	-9.6	1.5	1.4	0.1	3.1	1.2	1.2	1.1	68
Pre-FSR ($\mu^+\mu^-$)	-9.5	1.1	1.3	0.4	3.0	1.1	1.2	0.4	38
Pre-FSR (e^+e^-)	-9.6	1.3	1.4	-0.0	3.1	1.3	1.3	1.0	30
Post-FSR	-9.6	1.7	1.4	0.2	3.1	1.1	1.2	1.0	59
Post-FSR ($\mu^+\mu^-$)	-9.6	1.5	1.3	0.2	3.0	1.3	1.2	0.3	35
Post-FSR (e^+e^-)	-9.6	1.5	1.4	0.1	3.1	1.2	1.3	0.9	23
Input	-9.6				2.9				
Type	$\langle a_3 \rangle$ 10^{-2}	$\sigma^{\text{ens}}_{a_3}$ 10^{-2}	$\langle \sigma^{\text{fit}}_{a_3} \rangle$ 10^{-2}	$\Delta_{\langle a_3 \rangle}$ $\sigma_{\langle a_3 \rangle}$	$\langle b_3 \rangle$ 10^{-2}	$\sigma^{\text{ens}}_{b_3}$ 10^{-2}	$\langle \sigma^{\text{fit}}_{b_3} \rangle$ 10^{-2}	$\Delta_{\langle b_3 \rangle}$ $\sigma_{\langle b_3 \rangle}$	N
Pre-FSR	0				0.1	1.2	1.1	0.8	68
Pre-FSR ($\mu^+\mu^-$)	0				-0.0	1.1	1.2	-0.2	38
Pre-FSR (e^+e^-)	0				0.3	0.9	1.1	1.3	30
Post-FSR	0				0.1	1.2	1.1	0.5	59
Post-FSR ($\mu^+\mu^-$)	0				-0.0	1.3	1.2	-0.2	35
Post-FSR (e^+e^-)	0				0.2	1.5	1.1	1.0	30
Input	0				0				

Table A.4: Systematic uncertainties from kinematic fit type for $J_\chi = 2$ three-parameter fit. We compared fits to data from post-FSR (generator level), a kinematic fit to the ψ' four-vector and J/ψ mass without bremsstrahlung recovery, the same kinematic fit with bremsstrahlung recovery. We found no significant systematic uncertainties using the kinematic fits with bremsstrahlung recovery.

Type	$\langle a_2 \rangle$ 10^{-2}	$\sigma^{\text{ens}}_{a_2}$ 10^{-2}	$\langle \sigma^{\text{fit}}_{a_2} \rangle$ 10^{-2}	$\Delta_{\langle a_2 \rangle}$ $\sigma_{\langle a_2 \rangle}$	$\langle b_2 \rangle$ 10^{-2}	$\sigma^{\text{ens}}_{b_2}$ 10^{-2}	$\langle \sigma^{\text{fit}}_{b_2} \rangle$ 10^{-2}	$\Delta_{\langle b_2 \rangle}$ $\sigma_{\langle b_2 \rangle}$	N
Post-FSR	-9.6	1.7	1.4	0.2	3.1	1.1	1.2	1.0	59
4C, 1C (no b.r.)	-9.7	1.6	1.6	-0.4	3.2	1.3	1.3	1.5	40
4C, 1C (brem. rec.)	-9.7	1.6	1.5	-0.6	3.2	1.2	1.3	1.3	43
Input	-9.6				2.9				
Type	$\langle a_3 \rangle$ 10^{-2}	$\sigma^{\text{ens}}_{a_3}$ 10^{-2}	$\langle \sigma^{\text{fit}}_{a_3} \rangle$ 10^{-2}	$\Delta_{\langle a_3 \rangle}$ $\sigma_{\langle a_3 \rangle}$	$\langle b_3 \rangle$ 10^{-2}	$\sigma^{\text{ens}}_{b_3}$ 10^{-2}	$\langle \sigma^{\text{fit}}_{b_3} \rangle$ 10^{-2}	$\Delta_{\langle b_3 \rangle}$ $\sigma_{\langle b_3 \rangle}$	N
Post-FSR	0				0.1	1.2	1.1	0.5	59
4C, 1C (no b.r.)	0				0.1	1.2	1.2	0.4	40
4C, 1C (brem. rec.)	0				0.1	1.2	1.2	0.8	43
Input	0				0				

Table A.5: Selection criteria variations for $J_\chi = 2$ three-parameter fit listing a_2, b_2 performed on Monte Carlo events. For each set of selection criteria listed, we list an ensemble of fits with only signal events present (Signal) and the difference each fit is shifted if the impurity background is also included (Diff.).

Type	$\langle a_2 \rangle$ 10^{-2}	$\sigma_{a_2}^{\text{ens}}$ 10^{-2}	$\langle \sigma_{a_2}^{\text{fit}} \rangle$ 10^{-2}	$\Delta_{\langle a_2 \rangle}$ $\sigma_{\langle a_2 \rangle}$	$\langle b_2 \rangle$ 10^{-2}	$\sigma_{b_2}^{\text{ens}}$ 10^{-2}	$\langle \sigma_{b_2}^{\text{fit}} \rangle$ 10^{-2}	$\Delta_{\langle b_2 \rangle}$ $\sigma_{\langle b_2 \rangle}$
Default Cuts Signal	-9.8	1.4	1.6	-0.6	3.0	1.3	1.3	0.7
Default Cuts Diff.	-0.001	0.007			0.055	0.005		
$E^{\text{3rd Shwr}} < 18\,\text{MeV}$ Signal	-9.8	1.5	1.6	-0.8	3.2	1.4	1.4	1.2
$E^{\text{3rd Shwr}} < 18\,\text{MeV}$ Diff.	0.036	0.008			0.078	0.005		
$E^{\text{3rd Shwr}} < 50\,\text{MeV}$ Signal	-9.8	1.4	1.5	-0.7	3.0	1.3	1.3	0.7
$E^{\text{3rd Shwr}} < 50\,\text{MeV}$ Diff.	0.137	0.015			0.174	0.011		
$\chi^2_{\text{k.f.}} < 10$ Signal	-9.8	1.5	1.6	-0.9	3.1	1.4	1.3	1.0
$\chi^2_{\text{k.f.}} < 10$ Diff.	0				0.2	1.0	1.2	0.9
$\chi^2_{\text{k.f.}} < 30$ Signal	-9.7	1.4	1.5	-0.4	3.0	1.3	1.3	0.7
$\chi^2_{\text{k.f.}} < 30$ Diff.	-0.114	0.01			0.068	0.007		
χ_c mass $\pm 10\,\text{MeV}$ Signal	-9.8	1.4	1.6	-0.6	3.0	1.2	1.3	0.6
χ_c mass $\pm 10\,\text{MeV}$ Diff.	0.036	0.004			0.009	0.004		
χ_c mass $\pm 20\,\text{MeV}$ Signal	-9.7	1.3	1.6	-0.5	3.0	1.3	1.3	0.7
χ_c mass $\pm 20\,\text{MeV}$ Diff.	0.067	0.013			0.125	0.007		
$\lvert\cos\theta_{\text{lab,ph}}^{\text{barrel}}\rvert < 0.77$ Signal	-9.8	1.4	1.6	-0.8	3.0	1.3	1.3	0.6
$\lvert\cos\theta_{\text{lab,ph}}^{\text{barrel}}\rvert < 0.77$ Diff.	-0.008	0.007			0.039	0.005		
$\lvert\cos\theta_{\text{lab,ph}}^{\text{barrel}}\rvert < 0.80$ Signal	-9.8	1.4	1.5	-0.7	3.0	1.3	1.3	0.6
$\lvert\cos\theta_{\text{lab,ph}}^{\text{barrel}}\rvert < 0.80$ Diff.	-0.012	0.008			0.05	0.005		

Table A.6: Selection criteria variations for $J_\chi = 2$ three-parameter fit listing a_3, b_3 performed on Monte Carlo events. For each set of selection criteria listed, we list an ensemble of fits with only signal events present (Signal) and the difference each fit is shifted if the impurity background is also included (Diff.).

Type	$\langle a_3 \rangle$ 10^{-2}	$\sigma^{\text{ens}}_{a_3}$ 10^{-2}	$\langle \sigma^{\text{fit}}_{a_3} \rangle$ 10^{-2}	$\Delta_{\langle a_3 \rangle}$ $\sigma_{\langle a_3 \rangle}$	$\langle b_3 \rangle$ 10^{-2}	$\sigma^{\text{ens}}_{b_3}$ 10^{-2}	$\langle \sigma^{\text{fit}}_{b_3} \rangle$ 10^{-2}	$\Delta_{\langle b_3 \rangle}$ $\sigma_{\langle b_3 \rangle}$
Default Cuts Signal	0				0.1	1.0	1.2	0.3
Default Cuts Diff.	0				-0.061	0.004		
$E^{\text{3rd Shwr}} < 18\,\text{MeV}$ Signal	0				0.2	1.0	1.2	0.8
$E^{\text{3rd Shwr}} < 18\,\text{MeV}$ Diff.	0				-0.028	0.004		
$E^{\text{3rd Shwr}} < 50\,\text{MeV}$ Signal	0				0.1	0.9	1.2	0.3
$E^{\text{3rd Shwr}} < 50\,\text{MeV}$ Diff.	0				-0.128	0.008		
$\chi^2_{\text{k.f.}} < 10$ Signal	0				0.1	1.0	1.2	0.6
$\chi^2_{\text{k.f.}} < 10$ Diff.	0				-0.044	0.003		
$\chi^2_{\text{k.f.}} < 30$ Signal	0				0.0	0.9	1.1	0.2
$\chi^2_{\text{k.f.}} < 30$ Diff.	0				-0.071	0.007		
χ_c mass $\pm 10\,\text{MeV}$ Signal	0				0.1	1.0	1.2	0.6
χ_c mass $\pm 10\,\text{MeV}$ Diff.	0				-0.037	0.003		
χ_c mass $\pm 20\,\text{MeV}$ Signal	0				0.1	1.0	1.2	0.4
χ_c mass $\pm 20\,\text{MeV}$ Diff.	0				-0.0	0.006		
$\lvert\cos\theta^{\text{barrel}}_{\text{lab,ph}}\rvert < 0.77$ Signal	0				0.1	1.0	1.2	0.3
$\lvert\cos\theta^{\text{barrel}}_{\text{lab,ph}}\rvert < 0.77$ Diff.	0				-0.073	0.005		
$\lvert\cos\theta^{\text{barrel}}_{\text{lab,ph}}\rvert < 0.80$ Signal	0				0.1	1.0	1.2	0.4
$\lvert\cos\theta^{\text{barrel}}_{\text{lab,ph}}\rvert < 0.80$ Diff.	0				-0.067	0.005		

Table A.7: Summary of uncertainties from selection criteria variations for $J_\chi = 2$ three-parameter fit performed on Monte Carlo events. We compare the statistical uncertainty, impurity bias (assigned as a systematic uncertainty) and their quadrature sum from the previous two tables.

Cuts	$\sigma^{\text{stat}}_{a_2}$ 10^{-2}	$\sigma^{\text{sys imp}}_{a_2}$ 10^{-2}	$\sigma^{\text{total quad sum}}_{a_2}$ 10^{-2}	$\sigma^{\text{stat}}_{b_2}$ 10^{-2}	$\sigma^{\text{sys imp}}_{b_2}$ 10^{-2}	$\sigma^{\text{total quad sum}}_{b_2}$ 10^{-2}
Default Cuts	1.565	0.001	1.565	1.308	0.055	1.309
$E^{\text{3rd Shwr}} < 18\,\text{MeV}$	1.632	0.036	1.632	1.359	0.078	1.361
$E^{\text{3rd Shwr}} < 50\,\text{MeV}$	1.539	0.137	1.545	1.287	0.174	1.299
$\chi^2_{\text{k.f.}} < 10$	1.617	0.02	1.617	1.346	0.035	1.347
$\chi^2_{\text{k.f.}} < 30$	1.53	0.114	1.534	1.282	0.068	1.284
χ_c mass $\pm 10\,\text{MeV}$	1.607	0.036	1.607	1.344	0.009	1.344
χ_c mass $\pm 20\,\text{MeV}$	1.55	0.067	1.552	1.296	0.125	1.302
$\lvert\cos\theta^{\text{barrel}}_{\text{lab,ph}}\rvert < 0.77$	1.609	0.008	1.609	1.343	0.039	1.343
$\lvert\cos\theta^{\text{barrel}}_{\text{lab,ph}}\rvert < 0.80$	1.549	0.012	1.549	1.296	0.05	1.297

Cuts	$\sigma^{\text{stat}}_{a_3}$ 10^{-2}	$\sigma^{\text{sys imp}}_{a_3}$ 10^{-2}	$\sigma^{\text{total quad sum}}_{a_3}$ 10^{-2}	$\sigma^{\text{stat}}_{b_3}$ 10^{-2}	$\sigma^{\text{sys imp}}_{b_3}$ 10^{-2}	$\sigma^{\text{total quad sum}}_{b_3}$ 10^{-2}
Default Cuts				1.172	0.061	1.173
$E^{\text{3rd Shwr}} < 18\,\text{MeV}$				1.219	0.028	1.22
$E^{\text{3rd Shwr}} < 50\,\text{MeV}$				1.154	0.128	1.161
$\chi^2_{\text{k.f.}} < 10$				1.206	0.044	1.207
$\chi^2_{\text{k.f.}} < 30$				1.15	0.071	1.152
χ_c mass $\pm 10\,\text{MeV}$				1.206	0.037	1.207
χ_c mass $\pm 20\,\text{MeV}$				1.16	0.0	1.16
$\lvert\cos\theta^{\text{barrel}}_{\text{lab,ph}}\rvert < 0.77$				1.199	0.073	1.202
$\lvert\cos\theta^{\text{barrel}}_{\text{lab,ph}}\rvert < 0.80$				1.163	0.067	1.165

Table A.8: Systematic uncertainties from selection criteria variations for $J_\chi = 2$ three-parameter fit performed on data. We find for all sets of selection criteria considered that there's a systematic uncertainty of $(0.4, 0.2, 0.4) \times 10^{-2}$ for (a_2, b_2, b_3) respectively over the variation of the criteria considered.

Cuts	a_2 10^{-2}	b_2 10^{-2}	b_3 10^{-2}
Default Cuts	-9.3 ± 1.6	0.7 ± 1.4	-0.8 ± 1.2
$E^{\text{3rd Shwr}} < 18\,\text{MeV}$	-9.3 ± 1.6	0.3 ± 1.4	-0.7 ± 1.2
$E^{\text{3rd Shwr}} < 50\,\text{MeV}$	-9.7 ± 1.6	0.1 ± 1.4	-1.0 ± 1.2
$\chi^2_{\text{k.f.}} < 10$	-9.1 ± 1.6	1.0 ± 1.4	-0.8 ± 1.2
$\chi^2_{\text{k.f.}} < 30$	-9.5 ± 1.5	0.2 ± 1.3	-0.3 ± 1.2
χ_c mass $\pm 10\,\text{MeV}$	-8.6 ± 1.6	0.6 ± 1.4	-0.9 ± 1.2
χ_c mass $\pm 20\,\text{MeV}$	-9.7 ± 1.5	0.5 ± 1.4	-0.7 ± 1.2
$\lvert\cos\theta^{\text{barrel}}_{\text{lab,ph}}\rvert < 0.77$	-9.6 ± 1.6	1.0 ± 1.4	-0.6 ± 1.2
$\lvert\cos\theta^{\text{barrel}}_{\text{lab,ph}}\rvert < 0.80$	-9.5 ± 1.5	1.1 ± 1.4	-0.5 ± 1.2
Ensemble	-9.4 ± 0.3	0.6 ± 0.3	-0.7 ± 0.2

APPENDIX B

TWO-PARAMETER FIT (a_2, b_3) WITH $b_2/b_1 \equiv -a_2/(3.367a_1)$ AND $a_3 \equiv 0$

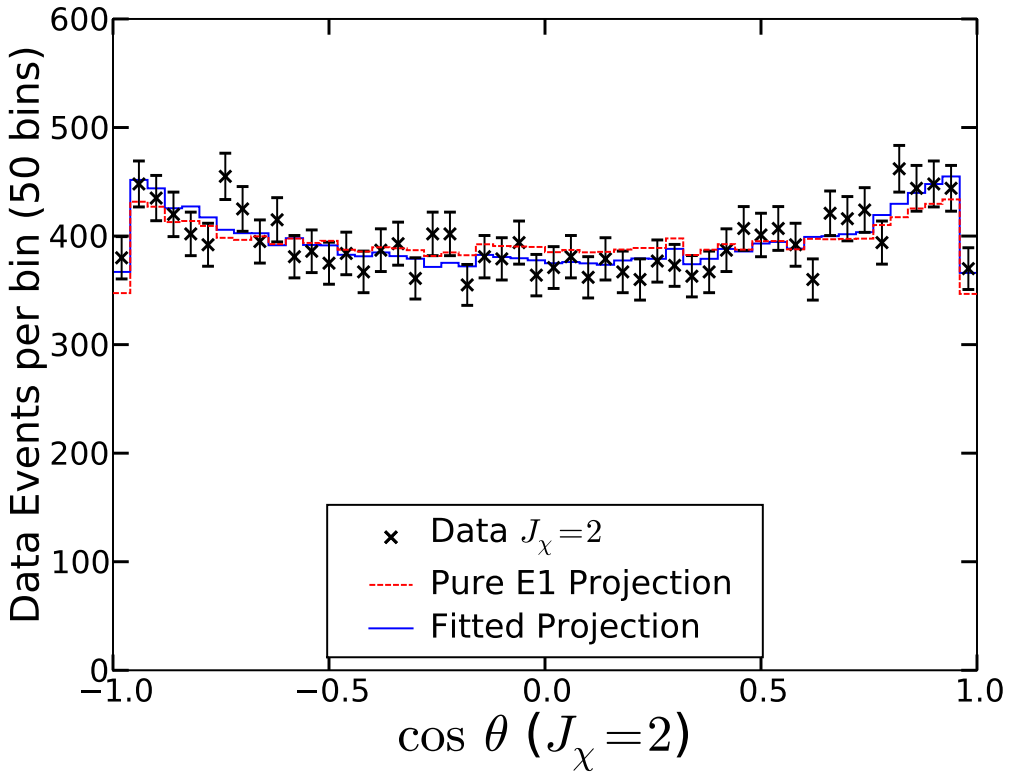

Figure B.1: $J_\chi = 2$ data vs projections for $\cos\theta$. The reduced chi square ($\chi^2/N_{\text{d.o.f.}}$) for the 50 bin histogram of the data to come from the same distribution as the fitted projection (holding $a_3 \equiv b_3 \equiv 0$) is $37.1/47 = 0.79$, and the reduced chi square for data to come from pure E1 is $53.1/49 = 1.08$. The fitted projection corresponds to the two-parameter fit $(a_2, b_3) = (-0.092, -0.001)$ with $b_2 \equiv -a_2/3.367 = 0.027$ and $a_3 \equiv 0$, which is 6.1σ from pure E1.

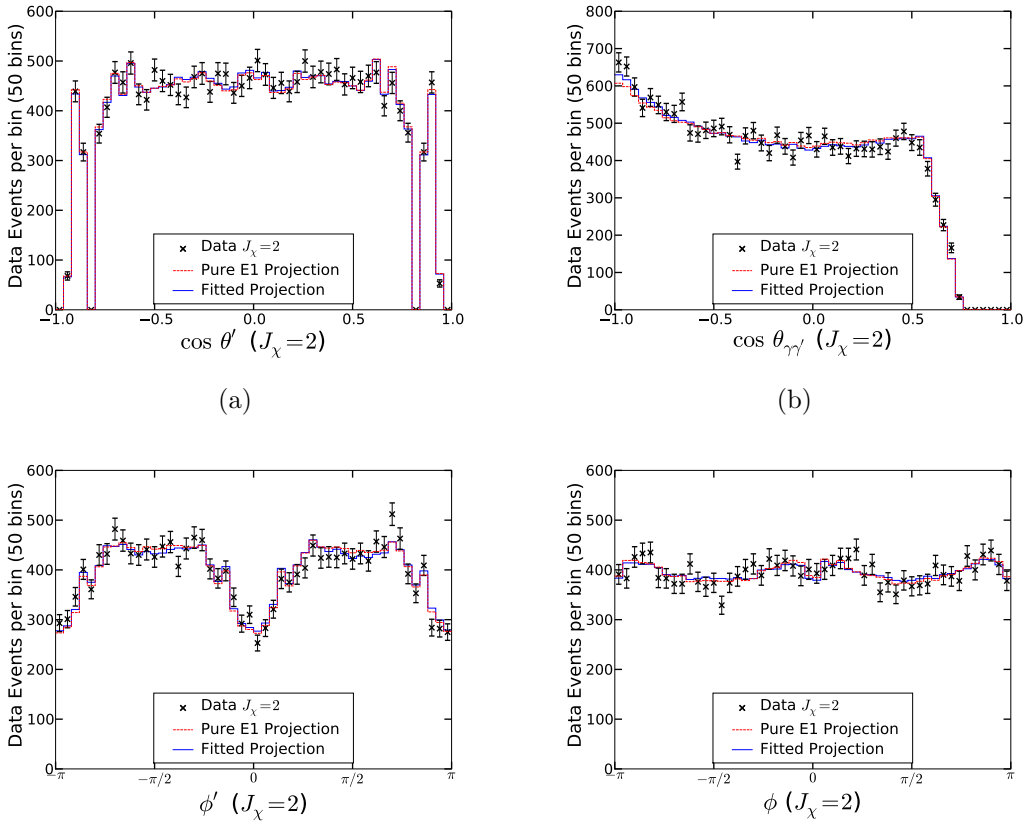

Figure B.2: $J_\chi = 2$ data vs projections for $\cos\theta', \cos\theta_{\gamma\gamma'}, \phi', \phi$. The reduced χ^2 comparing the 50 bin histogram of the data to the fitted projection are $36.4/47 = 0.78$, $51.3/47 = 1.09$, $47.3/47 = 1.01$, and $47.2/47 = 1.00$, while the $\chi^2/N_{\text{d.o.f.}}$ comparing data to the pure E1 projection are $38.9/49 = 0.79$, $59.8/49 = 1.22$, $50.6/49 = 1.03$, and $45.0/49 = 0.92$ for $\cos\theta', \cos\theta_{\gamma\gamma'}, \phi'$, and ϕ, respectively. The fitted projection corresponds to the two-parameter fit $(a_2, b_3) = (-0.092, -0.001)$ with $b_2 \equiv -a_2/3.367 = 0.027$ and $a_3 \equiv 0$, which is 6.1σ from pure E1.

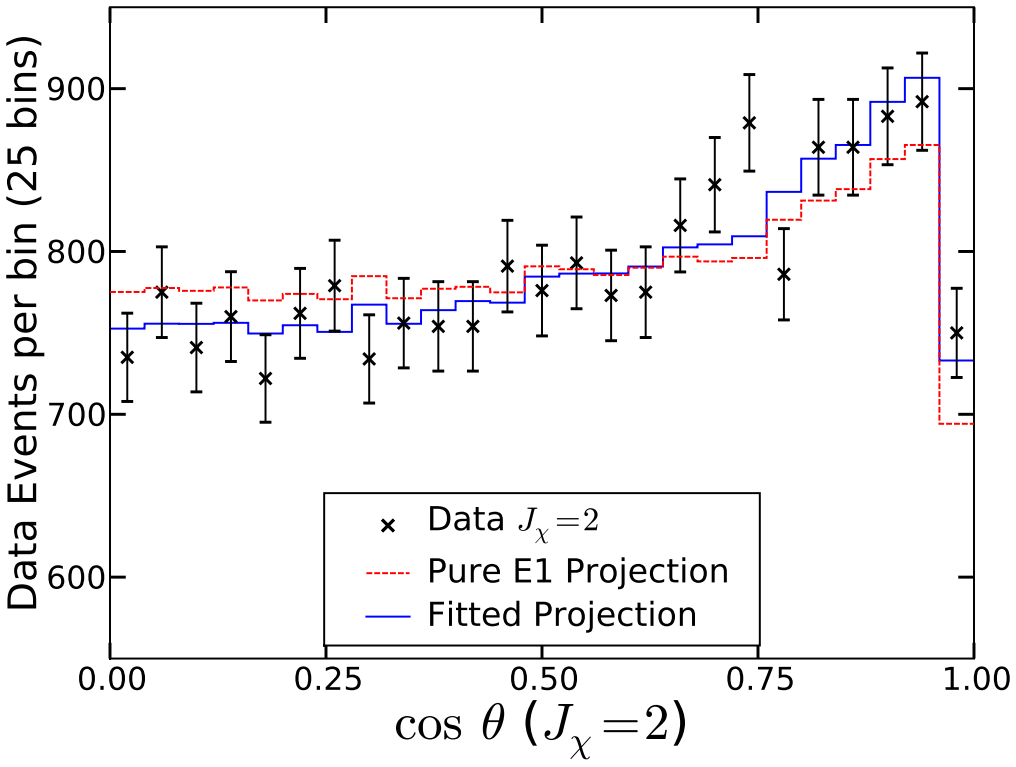

Figure B.3: $J_\chi = 2$ projection of $\cos\theta$ after using parity transformations to fold dataset into positive $\cos\theta', \phi', \cos\theta_{\gamma\gamma'}, \cos\theta$. The reduced χ^2 for the 25 bin histogram describing the data to correspond with the fitted projection and the pure E1 projection are $20.0/22 = 0.91$ and $35.5/24 = 1.48$, respectively. The fitted projection corresponds to the two-parameter fit $(a_2, b_3) = (-0.092, -0.001)$ with $b_2 \equiv -a_2/3.367 = 0.027$ and $a_3 \equiv 0$, which is 6.1σ from pure E1.

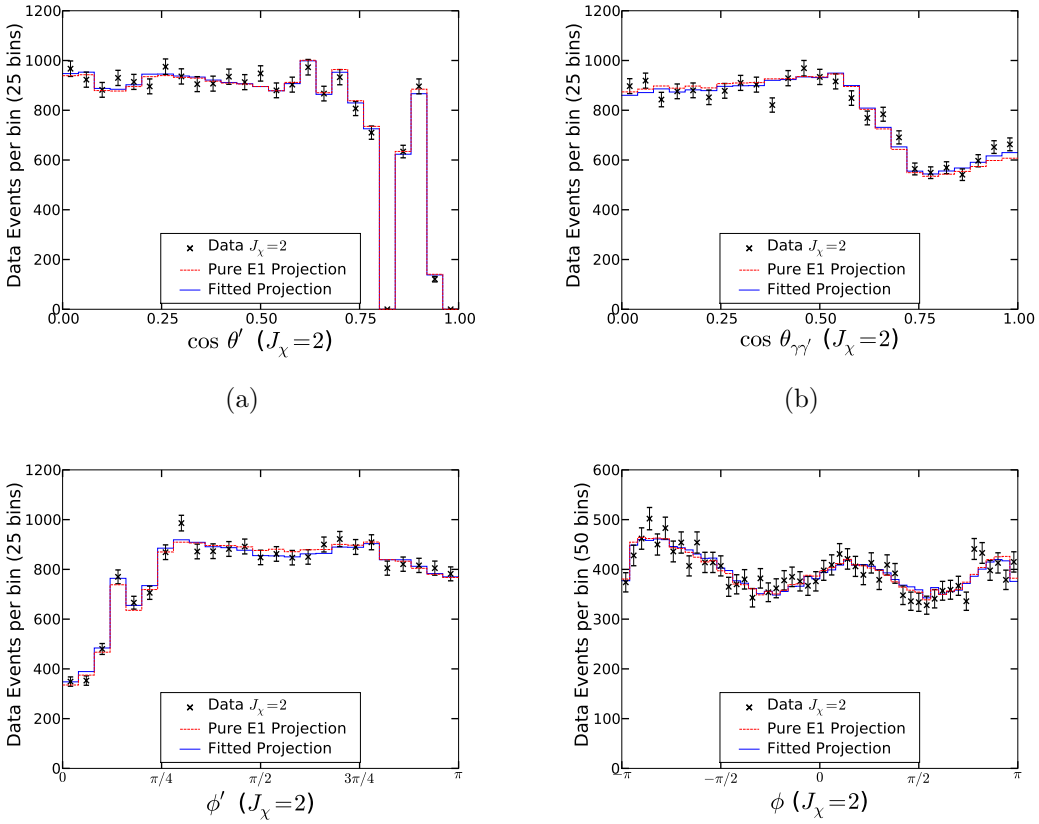

Figure B.4: $J_\chi=2$ projections for $\cos\theta'$, $\cos\theta_{\gamma\gamma'}$, ϕ', ϕ after using parity transformation to fold the dataset into positive $\cos\theta'$, ϕ', $\cos\theta_{\gamma\gamma'}$, $\cos\theta$. The reduced χ^2 comparing the 25 bin (50 bins for ϕ) histogram of the data to the fitted projection are $15.7/22 = 0.71$, $34.6/22 = 1.57$, $17.8/22 = 0.81$, and $56.0/47 = 1.19$, while the reduced χ^2 comparing data to the pure E1 projection are $17.7/24 = 0.74$, $43.2/24 = 1.80$, $21.3/24 = 0.89$, and $53.3/49 = 1.09$ for $\cos\theta'$, $\cos\theta_{\gamma\gamma'}$, ϕ', and ϕ, respectively. The fitted projection corresponds to the two-parameter fit $(a_2, b_3) = (-0.092, -0.001)$ with $b_2 \equiv -a_2/3.367 = 0.027$ and $a_3 \equiv 0$, which is 6.1σ from pure E1.

Table B.1: Systematic tests varying the number of phase space Monte Carlo events used in calculating the efficiency integrals for $J_\chi = 2$ two-parameter fixed-a_2/b_2-ratio fit. The quoted phase space data size are after applying all the selection criteria. There are no impurity events present in the data sample being fit.

PHSP size (After cuts)	$\langle a_2 \rangle$ 10^{-2}	$\sigma^{\rm ens}_{a_2}$ 10^{-2}	$\langle \sigma^{\rm fit}_{a_2} \rangle$ 10^{-2}	$\Delta_{\langle a_2 \rangle}$ $\sigma_{\langle a_2 \rangle}$	$\langle b_2 \rangle$ 10^{-2}	$\sigma^{\rm ens}_{b_2}$ 10^{-2}	$\langle \sigma^{\rm fit}_{b_2} \rangle$ 10^{-2}	$\Delta_{\langle b_2 \rangle}$ $\sigma_{\langle b_2 \rangle}$
3000	-10.2	4.1	1.5	-2.6	3.1	1.2	0.5	2.1
10000	-9.6	2.5	1.5	0.2	2.9	0.7	0.5	-0.6
30000	-9.5	1.6	1.5	0.2	2.8	0.5	0.5	-0.7
100000	-9.5	1.5	1.5	0.3	2.8	0.4	0.5	-0.8
300000	-9.5	1.4	1.5	0.3	2.8	0.4	0.5	-0.8
1759617	-9.7	1.4	1.5	-0.6	2.9	0.4	0.5	0.1
Input	-9.6				2.9			
PHSP size (After cuts)	$\langle a_3 \rangle$ 10^{-2}	$\sigma^{\rm ens}_{a_3}$ 10^{-2}	$\langle \sigma^{\rm fit}_{a_3} \rangle$ 10^{-2}	$\Delta_{\langle a_3 \rangle}$ $\sigma_{\langle a_3 \rangle}$	$\langle b_3 \rangle$ 10^{-2}	$\sigma^{\rm ens}_{b_3}$ 10^{-2}	$\langle \sigma^{\rm fit}_{b_3} \rangle$ 10^{-2}	$\Delta_{\langle b_3 \rangle}$ $\sigma_{\langle b_3 \rangle}$
3000	0				1.3	2.6	1.1	7.5
10000	0				0.1	1.8	1.1	0.5
30000	0				0.1	1.4	1.1	0.5
100000	0				0.0	1.1	1.1	0.0
300000	0				0.0	1.0	1.1	0.0
1759617	0				0.0	1.0	1.1	0.2
Input	0				0			

Table B.2: Systematic tests from including non-signal generic Monte Carlo events selected by the selection criteria for $J_\chi = 2$ two-parameter fixed-a_2/b_2-ratio fit. We find that the impurities add a negligible systematic uncertainty when compared to the statistical uncertainty. Refer to Section 5.4.

Type	$\langle a_2 \rangle$ 10^{-2}	$\sigma_{a_2}^{\text{ens}}$ 10^{-2}	$\langle \sigma_{a_2}^{\text{fit}} \rangle$ 10^{-2}	$\Delta_{\langle a_2 \rangle}$ $\sigma_{\langle a_2 \rangle}$	$\langle b_2 \rangle$ 10^{-2}	$\sigma_{b_2}^{\text{ens}}$ 10^{-2}	$\langle \sigma_{b_2}^{\text{fit}} \rangle$ 10^{-2}	$\Delta_{\langle b_2 \rangle}$ $\sigma_{\langle b_2 \rangle}$
Pure	-9.8	1.4	1.6	-0.7	2.9	0.4	0.5	0.2
Diff. (A)	-0.005	0.008			0.002	0.002		
Diff. (B)	0.081	0.005			-0.024	0.001		
Diff. (C)	-0.021	0.015			0.006	0.005		
Diff. (D)	0.03	0.002			-0.009	0.001		
Diff. (E)	-0.039	0.003			0.012	0.001		
Diff. (A-E)	0.045	0.023			-0.013	0.007		
Input	-9.6				2.9			
⟨Imp. Bias⟩	0.009	0.043						

Type	$\langle a_3 \rangle$ 10^{-2}	$\sigma_{a_3}^{\text{ens}}$ 10^{-2}	$\langle \sigma_{a_3}^{\text{fit}} \rangle$ 10^{-2}	$\Delta_{\langle a_3 \rangle}$ $\sigma_{\langle a_3 \rangle}$	$\langle b_3 \rangle$ 10^{-2}	$\sigma_{b_3}^{\text{ens}}$ 10^{-2}	$\langle \sigma_{b_3}^{\text{fit}} \rangle$ 10^{-2}	$\Delta_{\langle b_3 \rangle}$ $\sigma_{\langle b_3 \rangle}$
Pure	0				0.0	1.0	1.1	0.1
Diff. (A)	0				-0.078	0.005		
Diff. (B)	0				-0.016	0.003		
Diff. (C)	0				-0.041	0.004		
Diff. (D)	0				-0.028	0.001		
Diff. (E)	0				-0.032	0.003		
Diff. (A-E)	0				-0.193	0.014		
Input	0				0			
⟨Imp. Bias⟩	0.	0.			-0.039	0.021		

Table B.3: Systematic uncertainties from final state radiation (FSR) for $J_\chi = 2$ two-parameter fixed-a_2/b_2-ratio fit. We performed $N = 32$ pre-FSR and $N = 28$ post-FSR trials with exactly 20000 data events in each fit. Each trial had a five-angle two-parameter fit performed with $W(\Omega; \mathbb{A}_0)$ with $\mathbb{A} = (-0.096, 0.029, 0, 0)$.

Type	$\langle a_2 \rangle$ 10^{-2}	$\sigma^{\text{ens}}_{a_2}$ 10^{-2}	$\langle \sigma^{\text{fit}}_{a_2} \rangle$ 10^{-2}	$\Delta_{\langle a_2 \rangle}$ $\sigma_{\langle a_2 \rangle}$	$\langle b_2 \rangle$ 10^{-2}	$\sigma^{\text{ens}}_{b_2}$ 10^{-2}	$\langle \sigma^{\text{fit}}_{b_2} \rangle$ 10^{-2}	$\Delta_{\langle b_2 \rangle}$ $\sigma_{\langle b_2 \rangle}$	N
Pre-FSR	-9.6	1.4	1.4	0.1	2.9	0.4	0.4	-0.8	68
Pre-FSR ($\mu^+\mu^-$)	-9.5	1.1	1.3	0.3	2.8	0.3	0.4	-0.9	38
Pre-FSR (e^+e^-)	-9.6	1.3	1.4	-0.0	2.9	0.4	0.4	-0.4	30
Post-FSR	-9.6	1.7	1.4	0.2	2.9	0.5	0.4	-0.8	59
Post-FSR ($\mu^+\mu^-$)	-9.6	1.5	1.3	0.1	2.9	0.4	0.4	-0.6	35
Post-FSR (e^+e^-)	-9.6	1.6	1.4	0.1	2.9	0.5	0.4	-0.5	23
Input	-9.6				2.9				
Type	$\langle a_3 \rangle$ 10^{-2}	$\sigma^{\text{ens}}_{a_3}$ 10^{-2}	$\langle \sigma^{\text{fit}}_{a_3} \rangle$ 10^{-2}	$\Delta_{\langle a_3 \rangle}$ $\sigma_{\langle a_3 \rangle}$	$\langle b_3 \rangle$ 10^{-2}	$\sigma^{\text{ens}}_{b_3}$ 10^{-2}	$\langle \sigma^{\text{fit}}_{b_3} \rangle$ 10^{-2}	$\Delta_{\langle b_3 \rangle}$ $\sigma_{\langle b_3 \rangle}$	N
Pre-FSR	0				0.0	1.0	1.1	0.2	68
Pre-FSR ($\mu^+\mu^-$)	0				-0.1	0.9	1.1	-0.5	38
Pre-FSR (e^+e^-)	0				0.2	1.0	1.0	0.9	30
Post-FSR	0				0.0	1.0	1.1	0.0	59
Post-FSR ($\mu^+\mu^-$)	0				-0.1	1.2	1.1	-0.5	35
Post-FSR (e^+e^-)	0				0.1	1.4	1.0	0.6	23
Input	0				0				

Table B.4: Systematic uncertainties from kinematic fit type for $J_\chi = 2$ two-parameter fixed-a_2/b_2-ratio fit. We compared fits to data from post-FSR (generator level), a kinematic fit to the ψ' four-vector and J/ψ mass without bremsstrahlung recovery, the same kinematic fit with bremsstrahlung recovery. We found no significant systematic uncertainties using the kinematic fits with bremsstrahlung recovery.

Type	$\langle a_2 \rangle$ 10^{-2}	$\sigma^{\text{ens}}_{a_2}$ 10^{-2}	$\langle \sigma^{\text{fit}}_{a_2} \rangle$ 10^{-2}	$\Delta_{\langle a_2 \rangle}$ $\sigma_{\langle a_2 \rangle}$	$\langle b_2 \rangle$ 10^{-2}	$\sigma^{\text{ens}}_{b_2}$ 10^{-2}	$\langle \sigma^{\text{fit}}_{b_2} \rangle$ 10^{-2}	$\Delta_{\langle b_2 \rangle}$ $\sigma_{\langle b_2 \rangle}$	N
Post-FSR	-9.6	1.7	1.4	0.2	2.9	0.5	0.4	-0.8	59
4C, 1C (no b.r.)	-9.7	1.6	1.5	-0.4	2.9	0.5	0.5	-0.0	40
4C, 1C (brem. rec.)	-9.8	1.6	1.5	-0.7	2.9	0.5	0.5	0.2	43
Input	-9.6				2.9				
Type	$\langle a_3 \rangle$ 10^{-2}	$\sigma^{\text{ens}}_{a_3}$ 10^{-2}	$\langle \sigma^{\text{fit}}_{a_3} \rangle$ 10^{-2}	$\Delta_{\langle a_3 \rangle}$ $\sigma_{\langle a_3 \rangle}$	$\langle b_3 \rangle$ 10^{-2}	$\sigma^{\text{ens}}_{b_3}$ 10^{-2}	$\langle \sigma^{\text{fit}}_{b_3} \rangle$ 10^{-2}	$\Delta_{\langle b_3 \rangle}$ $\sigma_{\langle b_3 \rangle}$	N
Post-FSR	0				0.0	1.0	1.1	0.0	59
4C, 1C (no b.r.)	0				-0.0	1.2	1.1	-0.1	40
4C, 1C (brem. rec.)	0				0.1	1.1	1.1	0.3	43
Input	0				0				

Table B.5: Selection criteria variations for $J_\chi = 2$ two-parameter fixed-a_2/b_2-ratio fit listing a_2, b_2 performed on Monte Carlo events. For each set of selection criteria listed, we list an ensemble of fits with only signal events present (Signal) and the difference each fit is shifted if the impurity background is also included (Diff.).

Type	$\langle a_2 \rangle$ 10^{-2}	$\sigma^{\rm ens}_{a_2}$ 10^{-2}	$\langle \sigma^{\rm fit}_{a_2} \rangle$ 10^{-2}	$\Delta_{\langle a_2 \rangle}$ $\sigma_{\langle a_2 \rangle}$	$\langle b_2 \rangle$ 10^{-2}	$\sigma^{\rm ens}_{b_2}$ 10^{-2}	$\langle \sigma^{\rm fit}_{b_2} \rangle$ 10^{-2}	$\Delta_{\langle b_2 \rangle}$ $\sigma_{\langle b_2 \rangle}$
Default Cuts Signal	-9.8	1.4	1.6	-0.7	2.9	0.4	0.5	0.2
Default Cuts Diff.	-0.005	0.008			0.002	0.002		
$E^{\rm 3rd\ Shwr} < 18$ MeV Signal	-9.8	1.5	1.6	-0.8	2.9	0.4	0.5	0.4
$E^{\rm 3rd\ Shwr} < 18$ MeV Diff.	0.028	0.009			-0.009	0.003		
$E^{\rm 3rd\ Shwr} < 50$ MeV Signal	-9.8	1.3	1.5	-0.7	2.9	0.4	0.5	0.3
$E^{\rm 3rd\ Shwr} < 50$ MeV Diff.	0.119	0.02			-0.036	0.006		
$\chi^2_{\rm k.f.} < 10$ Signal	-9.8	1.4	1.6	-0.9	2.9	0.4	0.5	0.5
$\chi^2_{\rm k.f.} < 10$ Diff.	-0.022	0.005			0.007	0.002		
$\chi^2_{\rm k.f.} < 30$ Signal	-9.7	1.4	1.5	-0.4	2.9	0.4	0.5	-0.1
$\chi^2_{\rm k.f.} < 30$ Diff.	-0.118	0.01			0.035	0.003		
χ_c mass ± 10 MeV Signal	-9.8	1.4	1.6	-0.6	2.9	0.4	0.5	0.2
χ_c mass ± 10 MeV Diff.	0.034	0.005			-0.01	0.002		
χ_c mass ± 20 MeV Signal	-9.7	1.3	1.5	-0.6	2.9	0.4	0.5	0.1
χ_c mass ± 20 MeV Diff.	0.055	0.015			-0.017	0.005		
$\lvert\cos\theta^{\rm barrel}_{\rm lab,ph}\rvert < 0.77$ Signal	-9.8	1.4	1.6	-0.9	2.9	0.4	0.5	0.4
$\lvert\cos\theta^{\rm barrel}_{\rm lab,ph}\rvert < 0.77$ Diff.	-0.011	0.008			0.003	0.002		
$\lvert\cos\theta^{\rm barrel}_{\rm lab,ph}\rvert < 0.80$ Signal	-9.8	1.4	1.5	-0.7	2.9	0.4	0.5	0.2
$\lvert\cos\theta^{\rm barrel}_{\rm lab,ph}\rvert < 0.80$ Diff.	-0.016	0.008			0.005	0.003		

Table B.6: Selection criteria variations for $J_\chi = 2$ two-parameter fixed-a_2/b_2-ratio fit listing a_3, b_3 performed on Monte Carlo events. For each set of selection criteria listed, we list an ensemble of fits with only signal events present (Signal) and the difference each fit is shifted if the impurity background is also included (Diff.).

Type	$\langle a_3 \rangle$ 10^{-2}	$\sigma^{\rm ens}_{a_3}$ 10^{-2}	$\langle \sigma^{\rm fit}_{a_3} \rangle$ 10^{-2}	$\Delta_{\langle a_3 \rangle}$ $\sigma_{\langle a_3 \rangle}$	$\langle b_3 \rangle$ 10^{-2}	$\sigma^{\rm ens}_{b_3}$ 10^{-2}	$\langle \sigma^{\rm fit}_{b_3} \rangle$ 10^{-2}	$\Delta_{\langle b_3 \rangle}$ $\sigma_{\langle b_3 \rangle}$
Default Cuts Signal	0				0.0	1.0	1.1	0.1
Default Cuts Diff.	0				-0.078	0.005		
$E^{\text{3rd Shwr}} < 18\,\text{MeV}$ Signal	0				0.1	1.0	1.1	0.5
$E^{\text{3rd Shwr}} < 18\,\text{MeV}$ Diff.	0				-0.057	0.004		
$E^{\text{3rd Shwr}} < 50\,\text{MeV}$ Signal	0				0.0	0.9	1.1	0.1
$E^{\text{3rd Shwr}} < 50\,\text{MeV}$ Diff.	0				-0.197	0.009		
$\chi^2_{\text{k.f.}} < 10$ Signal	0				0.1	1.0	1.1	0.4
$\chi^2_{\text{k.f.}} < 10$ Diff.	0				-0.053	0.003		
$\chi^2_{\text{k.f.}} < 30$ Signal	0				-0.0	1.0	1.1	-0.1
$\chi^2_{\text{k.f.}} < 30$ Diff.	0				-0.082	0.008		
χ_c mass $\pm 10\,\text{MeV}$ Signal	0				0.1	1.0	1.1	0.5
χ_c mass $\pm 10\,\text{MeV}$ Diff.	0				-0.043	0.003		
χ_c mass $\pm 20\,\text{MeV}$ Signal	0				0.0	1.0	1.1	0.1
χ_c mass $\pm 20\,\text{MeV}$ Diff.	0				-0.047	0.008		
$\lvert\cos\theta^{\text{barrel}}_{\text{lab,ph}}\rvert < 0.77$ Signal	0				0.0	1.0	1.1	0.2
$\lvert\cos\theta^{\text{barrel}}_{\text{lab,ph}}\rvert < 0.77$ Diff.	0				-0.085	0.005		
$\lvert\cos\theta^{\text{barrel}}_{\text{lab,ph}}\rvert < 0.80$ Signal	0				0.0	1.0	1.1	0.3
$\lvert\cos\theta^{\text{barrel}}_{\text{lab,ph}}\rvert < 0.80$ Diff.	0				-0.082	0.005		

Table B.7: Summary of uncertainties from selection criteria variations for $J_\chi = 2$ two-parameter fixed-a_2/b_2-ratio fit performed on Monte Carlo events. We compare the statistical uncertainty, impurity bias (assigned as a systematic uncertainty) and their quadrature sum from the previous two tables.

Cuts	$\sigma_{a_2}^{\text{stat}}$ 10^{-2}	$\sigma_{a_2}^{\text{sys imp}}$ 10^{-2}	$\sigma_{a_2}^{\text{total quad sum}}$ 10^{-2}	$\sigma_{b_2}^{\text{stat}}$ 10^{-2}	$\sigma_{b_2}^{\text{sys imp}}$ 10^{-2}	$\sigma_{b_2}^{\text{total quad sum}}$ 10^{-2}
Default Cuts	1.562	0.005	1.562	0.47	0.002	0.47
$E^{\text{3rd Shwr}} < 18\,\text{MeV}$	1.629	0.028	1.629	0.49	0.009	0.491
$E^{\text{3rd Shwr}} < 50\,\text{MeV}$	1.537	0.119	1.541	0.463	0.036	0.464
$\chi^2_{\text{k.f.}} < 10$	1.615	0.022	1.615	0.486	0.007	0.486
$\chi^2_{\text{k.f.}} < 30$	1.527	0.118	1.532	0.46	0.035	0.461
χ_c mass $\pm 10\,\text{MeV}$	1.604	0.034	1.604	0.483	0.01	0.483
χ_c mass $\pm 20\,\text{MeV}$	1.547	0.055	1.548	0.466	0.017	0.466
$\lvert\cos\theta^{\text{barrel}}_{\text{lab,ph}}\rvert < 0.77$	1.606	0.011	1.606	0.483	0.003	0.483
$\lvert\cos\theta^{\text{barrel}}_{\text{lab,ph}}\rvert < 0.80$	1.546	0.016	1.546	0.465	0.005	0.465

Cuts	$\sigma_{a_3}^{\text{stat}}$ 10^{-2}	$\sigma_{a_3}^{\text{sys imp}}$ 10^{-2}	$\sigma_{a_3}^{\text{total quad sum}}$ 10^{-2}	$\sigma_{b_3}^{\text{stat}}$ 10^{-2}	$\sigma_{b_3}^{\text{sys imp}}$ 10^{-2}	$\sigma_{b_3}^{\text{total quad sum}}$ 10^{-2}
Default Cuts	-			1.102	0.078	1.104
$E^{\text{3rd Shwr}} < 18\,\text{MeV}$	-			1.148	0.057	1.149
$E^{\text{3rd Shwr}} < 50\,\text{MeV}$	-			1.085	0.197	1.102
$\chi^2_{\text{k.f.}} < 10$	-			1.135	0.053	1.136
$\chi^2_{\text{k.f.}} < 30$	-			1.081	0.082	1.084
χ_c mass $\pm 10\,\text{MeV}$	-			1.134	0.043	1.134
χ_c mass $\pm 20\,\text{MeV}$	-			1.091	0.047	1.092
$\lvert\cos\theta^{\text{barrel}}_{\text{lab,ph}}\rvert < 0.77$	-			1.126	0.085	1.13
$\lvert\cos\theta^{\text{barrel}}_{\text{lab,ph}}\rvert < 0.80$	-			1.093	0.082	1.096

Table B.8: Systematic uncertainties from selection criteria variations for $J_\chi = 2$ two-parameter fixed-a_2/b_2-ratio fit performed on data. We find for all sets of selection criteria considered that there's a systematic uncertainty of $(0.4, 0.5) \times 10^{-2}$ for (a_2, b_3) respectively over the variation of the criteria considered.

Cuts	a_2 10^{-2}	b_2 10^{-2}	b_3 10^{-2}
Default Cuts	-9.2 ± 1.6	2.7 ± 0.5	-0.1 ± 1.1
$E^{\text{3rd Shwr}} < 18\,\text{MeV}$	-9.2 ± 1.6	2.7 ± 0.5	0.1 ± 1.1
$E^{\text{3rd Shwr}} < 50\,\text{MeV}$	-9.6 ± 1.6	2.9 ± 0.5	-0.1 ± 1.1
$\chi^2_{\text{k.f.}} < 10$	-9.0 ± 1.6	2.7 ± 0.5	-0.2 ± 1.1
$\chi^2_{\text{k.f.}} < 30$	-9.4 ± 1.5	2.8 ± 0.5	0.5 ± 1.1
χ_c mass $\pm 10\,\text{MeV}$	-8.5 ± 1.6	2.5 ± 0.5	-0.3 ± 1.1
χ_c mass $\pm 20\,\text{MeV}$	-9.6 ± 1.5	2.9 ± 0.5	0.1 ± 1.1
$\lvert\cos\theta^{\text{barrel}}_{\text{lab,ph}}\rvert < 0.77$	-9.5 ± 1.6	2.8 ± 0.5	0.0 ± 1.1
$\lvert\cos\theta^{\text{barrel}}_{\text{lab,ph}}\rvert < 0.80$	-9.4 ± 1.5	2.8 ± 0.5	0.1 ± 1.1
Ensemble	-9.3 ± 0.3	2.8 ± 0.1	0.0 ± 0.2

APPENDIX C

FOUR-PARAMETER FIT (a_2, b_2, a_3, b_3)

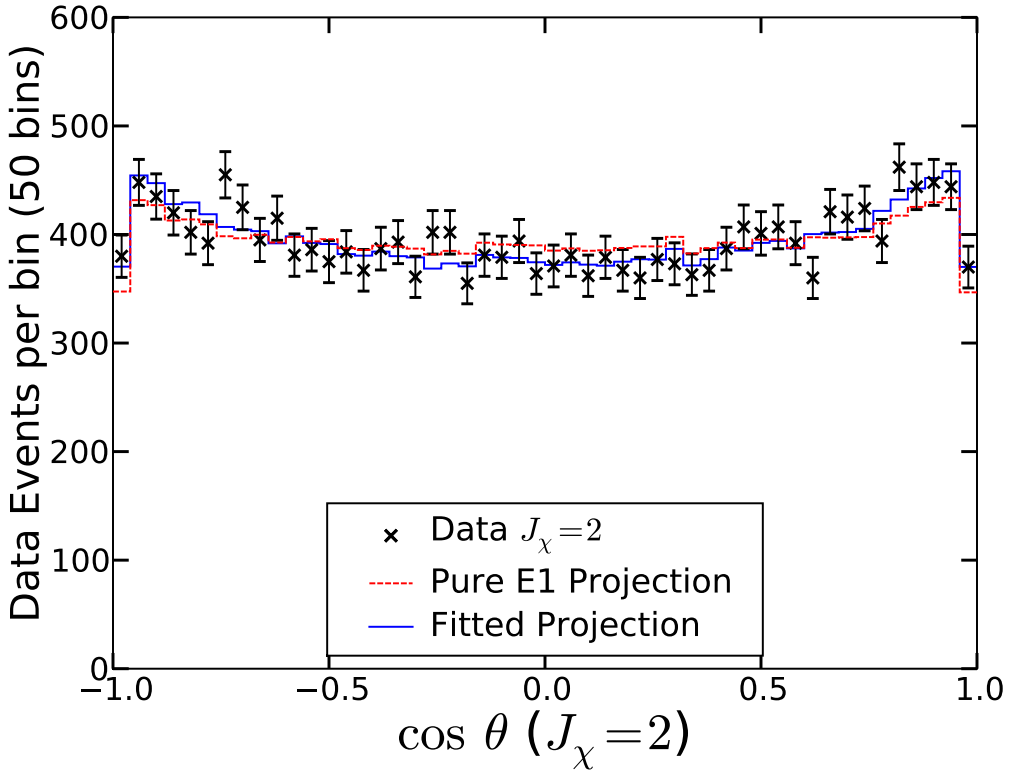

Figure C.1: $J_\chi = 2$ data vs projections for $\cos\theta$. The reduced chi square (χ^2) for the 50 bin histogram of the data to come from the same distribution as the fitted projection (holding $a_3 \equiv b_3 \equiv 0$) is $36.7/45 = 0.82$, and the reduced chi square for data to come from pure E1 is $53.1/49 = 1.08$. The fitted projection corresponds to the four-parameter fit $(a_2, b_2, a_3, b_3) = (-0.079, 0.002, 0.017, -0.008)$, which is 6.4σ from pure E1.

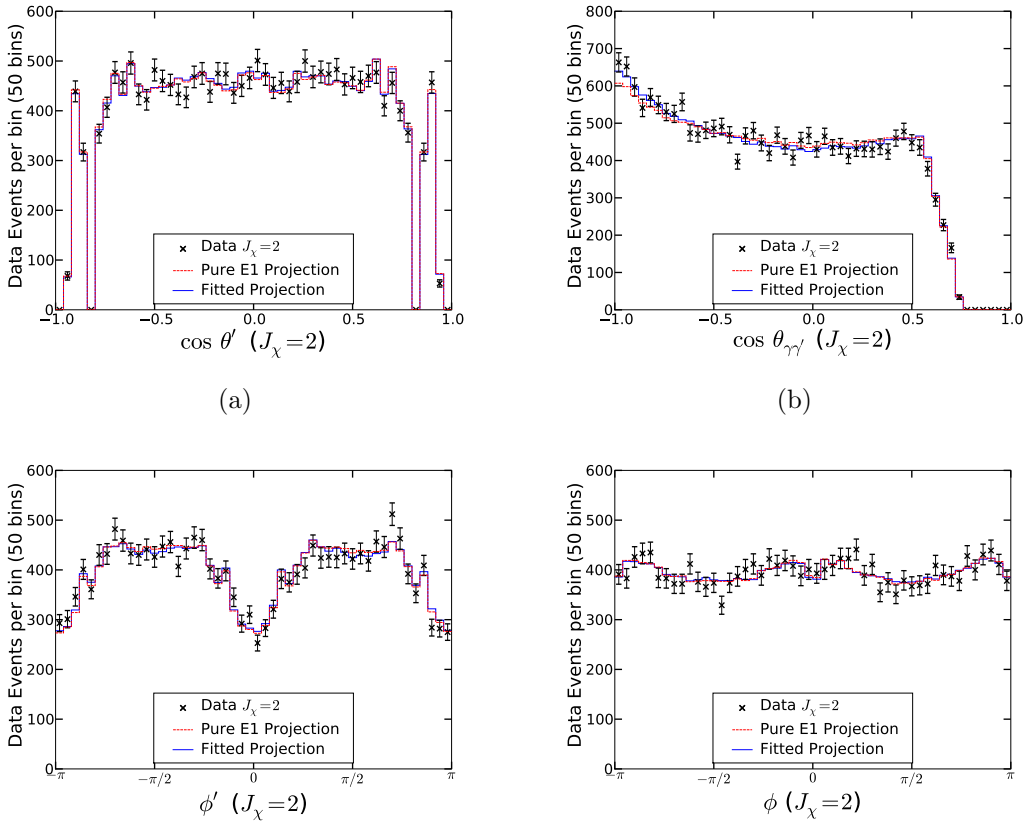

Figure C.2: $J_\chi = 2$ data vs projections for $\cos\theta', \cos\theta_{\gamma\gamma'}, \phi', \phi$. The reduced χ^2 comparing the 50 bin histogram of the data to the fitted projection are $32.3/45 = 0.81$, $50.2/45 = 1.12$, $47.9/45 = 1.06$, and $44.8/45 = 1.00$, while the reduced χ^2 comparing data to the pure E1 projection are $38.9/49 = 0.79$, $59.8/49 = 1.22$, $50.6/49 = 1.03$, and $45.0/49 = 0.92$ for $\cos\theta', \cos\theta_{\gamma\gamma'}, \phi'$, and ϕ, respectively. The fitted projection corresponds to the four-parameter fit $(a_2, b_2, a_3, b_3) = (-0.079, 0.002, 0.017, -0.008)$, which is 6.4σ from pure E1.

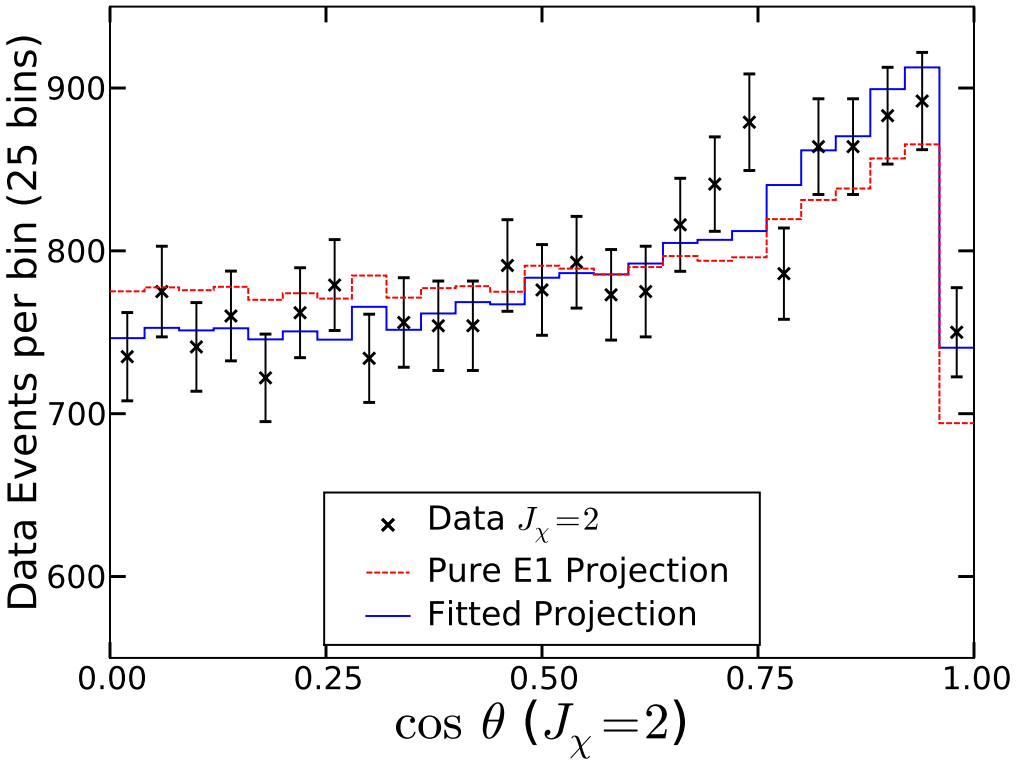

Figure C.3: $J_\chi = 2$ projection of $\cos\theta$ after using parity transformations to fold dataset into positive $\cos\theta', \phi', \cos\theta_{\gamma\gamma'}, \cos\theta$. The reduced χ^2 for the 25 bin histogram describing the data to correspond with the fitted projection and the pure E1 projection are $19.8/20 = 0.99$ and $35.5/24 = 1.48$, respectively. The fitted projection corresponds to the four-parameter fit $(a_2, b_2, a_3, b_3) = (-0.079, 0.002, 0.017, -0.008)$, which is 6.4σ from pure E1.

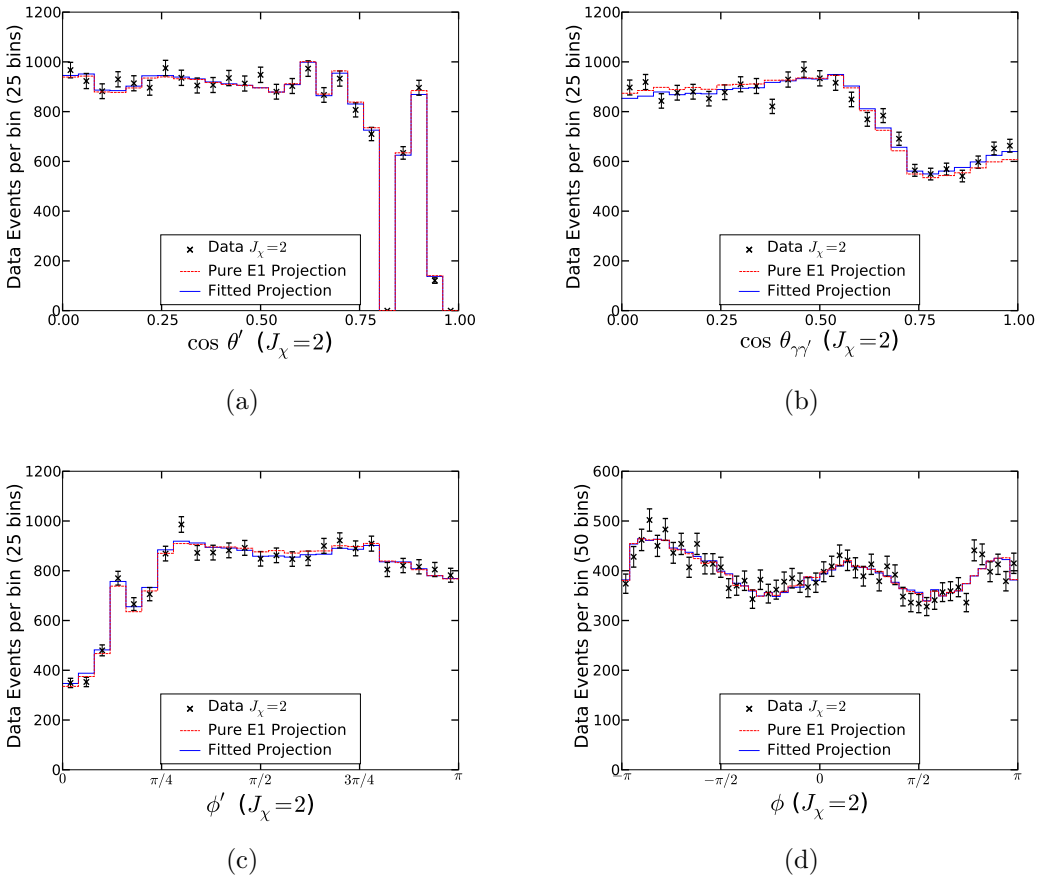

Figure C.4: $J_\chi = 2$ projections for $\cos\theta'$, $\cos\theta_{\gamma\gamma'}$, ϕ', ϕ after using parity transformation to fold the dataset into positive $\cos\theta'$, ϕ', $\cos\theta_{\gamma\gamma'}$, $\cos\theta$. The reduced χ^2 comparing the 25 bin (50 bins for ϕ) histogram of the data to the fitted projection are $15.6/20 = 0.78$, $33.7/20 = 1.68$, $18.1/20 = 0.91$, and $55.1/45 = 1.22$, while the reduced χ^2 comparing data to the pure E1 projection are $17.7/24 = 0.74$, $43.2/24 = 1.80$, $21.3/24 = 0.89$, and $53.1/49 = 1.08$ for $\cos\theta'$, $\cos\theta_{\gamma\gamma'}$, ϕ', and ϕ, respectively. The fitted projection corresponds to the four-parameter fit $(a_2, b_2, a_3, b_3) = (-0.079, 0.002, 0.017, -0.008)$, which is 6.4σ from pure E1.

Table C.1: Systematic tests varying the number of phase space Monte Carlo events used in calculating the efficiency integrals for $J_\chi = 2$ four-parameter fit. The quoted phase space data size are after applying all the selection criteria. There are no impurity events present in the data sample being fit.

PHSP size (After cuts)	$\langle a_2 \rangle$ 10^{-2}	$\sigma^{\rm ens}_{a_2}$ 10^{-2}	$\langle \sigma^{\rm fit}_{a_2} \rangle$ 10^{-2}	$\Delta_{\langle a_2 \rangle}$ $\sigma_{\langle a_2 \rangle}$	$\langle b_2 \rangle$ 10^{-2}	$\sigma^{\rm ens}_{b_2}$ 10^{-2}	$\langle \sigma^{\rm fit}_{b_2} \rangle$ 10^{-2}	$\Delta_{\langle b_2 \rangle}$ $\sigma_{\langle b_2 \rangle}$
3000	-10.0	6.0	1.9	-1.3	2.0	3.8	1.3	-4.4
10000	-9.4	3.3	1.9	0.5	2.9	2.4	1.3	0.1
30000	-9.4	2.3	1.9	0.7	2.9	1.9	1.3	0.1
100000	-9.3	2.2	1.9	0.9	2.9	1.5	1.3	0.2
300000	-9.4	2.2	1.9	0.6	3.0	1.4	1.3	0.5
1759617	-9.7	2.1	1.9	-0.3	3.0	1.5	1.3	0.5
Input	-9.6				2.9			
PHSP size (After cuts)	$\langle a_3 \rangle$ 10^{-2}	$\sigma^{\rm ens}_{a_3}$ 10^{-2}	$\langle \sigma^{\rm fit}_{a_3} \rangle$ 10^{-2}	$\Delta_{\langle a_3 \rangle}$ $\sigma_{\langle a_3 \rangle}$	$\langle b_3 \rangle$ 10^{-2}	$\sigma^{\rm ens}_{b_3}$ 10^{-2}	$\langle \sigma^{\rm fit}_{b_3} \rangle$ 10^{-2}	$\Delta_{\langle b_3 \rangle}$ $\sigma_{\langle b_3 \rangle}$
3000	0.6	4.4	1.4	2.6	1.1	2.5	1.1	5.6
10000	0.2	2.3	1.4	0.7	0.1	1.8	1.1	0.7
30000	0.2	1.7	1.4	1.0	0.1	1.4	1.1	0.7
100000	0.3	1.6	1.4	1.1	0.1	1.1	1.1	0.4
300000	0.1	1.6	1.4	0.6	0.1	1.0	1.1	0.4
1759617	0.1	1.6	1.4	0.3	0.1	1.0	1.1	0.4
Input	0				0			

Table C.2: Systematic tests from including non-signal generic Monte Carlo events selected by the selection criteria for $J_\chi = 2$ four-parameter fit. We find that the impurities add a negligible systematic uncertainty when compared to the statistical uncertainty. Refer to Section 5.4.

Type	$\langle a_2 \rangle$ 10^{-2}	$\sigma^{\rm ens}_{a_2}$ 10^{-2}	$\langle \sigma^{\rm fit}_{a_2} \rangle$ 10^{-2}	$\Delta_{\langle a_2 \rangle}$ $\sigma_{\langle a_2 \rangle}$	$\langle b_2 \rangle$ 10^{-2}	$\sigma^{\rm ens}_{b_2}$ 10^{-2}	$\langle \sigma^{\rm fit}_{b_2} \rangle$ 10^{-2}	$\Delta_{\langle b_2 \rangle}$ $\sigma_{\langle b_2 \rangle}$
Pure	-9.8	2.1	2.0	-0.5	3.0	1.4	1.4	0.5
Diff. (A)	-0.094	0.025			0.085	0.007		
Diff. (B)	0.053	0.008			-0.007	0.005		
Diff. (C)	-0.094	0.025			0.179	0.008		
Diff. (D)	-0.03	0.01			-0.048	0.009		
Diff. (E)	-0.124	0.009			0.043	0.009		
Diff. (A-E)	-0.287	0.054			0.254	0.028		
Input	-9.6				2.9			
⟨Imp. Bias⟩	-0.057	0.063			0.050	0.079		
Type	$\langle a_3 \rangle$ 10^{-2}	$\sigma^{\rm ens}_{a_3}$ 10^{-2}	$\langle \sigma^{\rm fit}_{a_3} \rangle$ 10^{-2}	$\Delta_{\langle a_3 \rangle}$ $\sigma_{\langle a_3 \rangle}$	$\langle b_3 \rangle$ 10^{-2}	$\sigma^{\rm ens}_{b_3}$ 10^{-2}	$\langle \sigma^{\rm fit}_{b_3} \rangle$ 10^{-2}	$\Delta_{\langle b_3 \rangle}$ $\sigma_{\langle b_3 \rangle}$
Pure	0.0	1.7	1.5	0.2	0.1	1.0	1.2	0.4
Diff. (A)	-0.113	0.016			-0.059	0.006		
Diff. (B)	-0.035	0.007			-0.013	0.003		
Diff. (C)	-0.103	0.015			0.007	0.003		
Diff. (D)	-0.067	0.009			-0.046	0.005		
Diff. (E)	-0.102	0.008			-0.03	0.005		
Diff. (A-E)	-0.417	0.04			-0.139	0.021		
Input	0				0			
⟨Imp. Bias⟩	-0.084	0.024			-0.028	0.024		

Table C.3: Systematic uncertainties from final state radiation (FSR) for $J_\chi = 2$ four-parameter fit. We performed $N = 32$ pre-FSR and $N = 28$ post-FSR trials with exactly 20000 data events in each fit. Each trial had a five-angle two-parameter fit performed with $W(\Omega; \mathbb{A}_0)$ with $\mathbb{A} = (-0.096, 0.029, 0, 0)$.

Type	$\langle a_2 \rangle$ 10^{-2}	$\sigma^{\text{ens}}_{a_2}$ 10^{-2}	$\langle \sigma^{\text{fit}}_{a_2} \rangle$ 10^{-2}	$\Delta_{\langle a_2 \rangle}$ $\sigma_{\langle a_2 \rangle}$	$\langle b_2 \rangle$ 10^{-2}	$\sigma^{\text{ens}}_{b_2}$ 10^{-2}	$\langle \sigma^{\text{fit}}_{b_2} \rangle$ 10^{-2}	$\Delta_{\langle b_2 \rangle}$ $\sigma_{\langle b_2 \rangle}$	N
Pre-FSR	-9.4	2.0	1.7	0.8	3.0	1.2	1.3	0.7	68
Pre-FSR ($\mu^+\mu^-$)	-9.3	1.3	1.6	1.0	2.9	1.0	1.3	0.2	38
Pre-FSR (e^+e^-)	-9.5	1.6	1.7	0.4	3.1	1.3	1.3	0.8	30
Post-FSR	-9.4	2.1	1.7	0.8	3.0	1.2	1.3	0.7	59
Post-FSR ($\mu^+\mu^-$)	-9.4	1.9	1.7	0.7	2.9	1.4	1.3	0.1	35
Post-FSR (e^+e^-)	-9.5	1.4	1.8	0.3	3.1	1.1	1.3	0.7	23
Input	-9.6				2.9				
Type	$\langle a_3 \rangle$ 10^{-2}	$\sigma^{\text{ens}}_{a_3}$ 10^{-2}	$\langle \sigma^{\text{fit}}_{a_3} \rangle$ 10^{-2}	$\Delta_{\langle a_3 \rangle}$ $\sigma_{\langle a_3 \rangle}$	$\langle b_3 \rangle$ 10^{-2}	$\sigma^{\text{ens}}_{b_3}$ 10^{-2}	$\langle \sigma^{\text{fit}}_{b_3} \rangle$ 10^{-2}	$\Delta_{\langle b_3 \rangle}$ $\sigma_{\langle b_3 \rangle}$	N
Pre-FSR	0.2	1.6	1.4	1.3	0.1	1.1	1.1	0.6	68
Pre-FSR ($\mu^+\mu^-$)	0.3	1.5	1.5	1.1	-0.1	1.0	1.2	-0.3	38
Pre-FSR (e^+e^-)	0.2	1.3	1.4	0.7	0.2	0.9	1.1	1.2	30
Post-FSR	0.2	1.4	1.4	1.2	0.1	1.2	1.2	0.4	59
Post-FSR ($\mu^+\mu^-$)	0.3	1.6	1.5	1.0	-0.1	1.3	1.2	-0.3	35
Post-FSR (e^+e^-)	0.1	1.4	1.4	0.3	0.2	1.5	1.1	0.9	23
Input	0				0				

Table C.4: Systematic uncertainties from kinematic fit type for $J_\chi = 2$ four-parameter fit. We compared fits to data from post-FSR (generator level), a kinematic fit to the ψ' four-vector and J/ψ mass without bremsstrahlung recovery, the same kinematic fit with bremsstrahlung recovery. We found no significant systematic uncertainties using the kinematic fits with bremsstrahlung recovery.

Type	$\langle a_2 \rangle$ 10^{-2}	$\sigma^{\text{ens}}_{a_2}$ 10^{-2}	$\langle \sigma^{\text{fit}}_{a_2} \rangle$ 10^{-2}	$\Delta_{\langle a_2 \rangle}$ $\sigma_{\langle a_2 \rangle}$	$\langle b_2 \rangle$ 10^{-2}	$\sigma^{\text{ens}}_{b_2}$ 10^{-2}	$\langle \sigma^{\text{fit}}_{b_2} \rangle$ 10^{-2}	$\Delta_{\langle b_2 \rangle}$ $\sigma_{\langle b_2 \rangle}$	N
Post-FSR	-9.4	2.1	1.7	0.8	3.0	1.2	1.3	0.7	59
4C, 1C (no b.r.)	-9.6	2.0	2.0	-0.0	3.2	1.2	1.4	1.3	
4C, 1C (brem. rec.)	-9.7	2.2	1.9	-0.3	3.1	1.3	1.3	1.1	
Input	-9.6				2.9				
Type	$\langle a_3 \rangle$ 10^{-2}	$\sigma^{\text{ens}}_{a_3}$ 10^{-2}	$\langle \sigma^{\text{fit}}_{a_3} \rangle$ 10^{-2}	$\Delta_{\langle a_3 \rangle}$ $\sigma_{\langle a_3 \rangle}$	$\langle b_3 \rangle$ 10^{-2}	$\sigma^{\text{ens}}_{b_3}$ 10^{-2}	$\langle \sigma^{\text{fit}}_{b_3} \rangle$ 10^{-2}	$\Delta_{\langle b_3 \rangle}$ $\sigma_{\langle b_3 \rangle}$	N
Post-FSR	0.2	1.4	1.4	1.2	0.1	1.2	1.2	0.4	59
4C, 1C (no b.r.)	0.1	1.1	1.5	0.4	0.1	1.2	1.2	0.5	
4C, 1C (brem. rec.)	0.1	1.3	1.5	0.4	0.1	1.1	1.2	0.7	
Input	0				0				

Table C.5: Selection criteria variations for $J_\chi = 2$ four-parameter fit listing a_2, b_2 performed on Monte Carlo events. For each set of selection criteria listed, we list an ensemble of fits with only signal events present (Signal) and the difference each fit is shifted if the impurity background is also included (Diff.).

Type	$\langle a_2 \rangle$ 10^{-2}	$\sigma_{a_2}^{\text{ens}}$ 10^{-2}	$\langle \sigma_{a_2}^{\text{fit}} \rangle$ 10^{-2}	$\Delta_{\langle a_2 \rangle}$ $\sigma_{\langle a_2 \rangle}$	$\langle b_2 \rangle$ 10^{-2}	$\sigma_{b_2}^{\text{ens}}$ 10^{-2}	$\langle \sigma_{b_2}^{\text{fit}} \rangle$ 10^{-2}	$\Delta_{\langle b_2 \rangle}$ $\sigma_{\langle b_2 \rangle}$
Default Cuts Signal	-9.8	2.1	2.0	-0.5	3.0	1.4	1.4	0.5
Default Cuts Diff.	-0.094	0.025			0.085	0.007		
$E^{\text{3rd Shwr}} < 18\,\text{MeV}$ Signal	-9.7	2.2	2.1	-0.4	3.1	1.4	1.4	1.0
$E^{\text{3rd Shwr}} < 18\,\text{MeV}$ Diff.	-0.052	0.024			0.107	0.007		
$E^{\text{3rd Shwr}} < 50\,\text{MeV}$ Signal	-9.8	2.1	1.9	-0.5	3.0	1.4	1.3	0.6
$E^{\text{3rd Shwr}} < 50\,\text{MeV}$ Diff.	0.025	0.04			0.211	0.012		
$\chi^2_{\text{k.f.}} < 10$ Signal	-9.8	2.2	2.0	-0.6	3.1	1.4	1.4	0.8
$\chi^2_{\text{k.f.}} < 10$ Diff.	-0.018	0.006			0.035	0.004		
$\chi^2_{\text{k.f.}} < 30$ Signal	-9.7	2.2	1.9	-0.3	3.0	1.4	1.3	0.6
$\chi^2_{\text{k.f.}} < 30$ Diff.	-0.267	0.024			0.12	0.02		
χ_c mass $\pm 10\,\text{MeV}$ Signal	-9.7	2.2	2.0	-0.4	3.0	1.4	1.4	0.4
χ_c mass $\pm 10\,\text{MeV}$ Diff.	0.001	0.008			0.02	0.004		
χ_c mass $\pm 20\,\text{MeV}$ Signal	-9.7	2.0	2.0	-0.4	3.0	1.4	1.4	0.6
χ_c mass $\pm 20\,\text{MeV}$ Diff.	-0.061	0.034			0.167	0.009		
$\lvert\cos\theta_{\text{lab,ph}}^{\text{barrel}}\rvert < 0.77$ Signal	-9.8	2.2	2.0	-0.6	3.0	1.4	1.4	0.5
$\lvert\cos\theta_{\text{lab,ph}}^{\text{barrel}}\rvert < 0.77$ Diff.	-0.1	0.026			0.07	0.007		
$\lvert\cos\theta_{\text{lab,ph}}^{\text{barrel}}\rvert < 0.80$ Signal	-9.7	2.2	2.0	-0.4	3.0	1.4	1.4	0.4
$\lvert\cos\theta_{\text{lab,ph}}^{\text{barrel}}\rvert < 0.80$ Diff.	-0.107	0.026			0.081	0.007		

Table C.6: Selection criteria variations for $J_\chi = 2$ four-parameter fit listing a_3, b_3 performed on Monte Carlo events. For each set of selection criteria listed, we list an ensemble of fits with only signal events present (Signal) and the difference each fit is shifted if the impurity background is also included (Diff.).

Type	$\langle a_3 \rangle$ 10^{-2}	$\sigma^{\rm ens}_{a_3}$ 10^{-2}	$\langle \sigma^{\rm fit}_{a_3} \rangle$ 10^{-2}	$\Delta_{\langle a_3 \rangle}$ $\sigma_{\langle a_3 \rangle}$	$\langle b_3 \rangle$ 10^{-2}	$\sigma^{\rm ens}_{b_3}$ 10^{-2}	$\langle \sigma^{\rm fit}_{b_3} \rangle$ 10^{-2}	$\Delta_{\langle b_3 \rangle}$ $\sigma_{\langle b_3 \rangle}$
Default Cuts Signal	0.0	1.7	1.5	0.2	0.1	1.0	1.2	0.4
Default Cuts Diff.	-0.113	0.016			-0.059	0.006		
$E^{\text{3rd Shwr}} < 18\,\text{MeV}$ Signal	0.1	1.7	1.5	0.4	0.2	1.0	1.2	0.8
$E^{\text{3rd Shwr}} < 18\,\text{MeV}$ Diff.	-0.106	0.015			-0.027	0.006		
$E^{\text{3rd Shwr}} < 50\,\text{MeV}$ Signal	0.0	1.7	1.4	0.1	0.1	0.9	1.2	0.3
$E^{\text{3rd Shwr}} < 50\,\text{MeV}$ Diff.	-0.137	0.024			-0.127	0.008		
$\chi^2_{\text{k.f.}} < 10$ Signal	0.1	1.8	1.5	0.2	0.1	1.0	1.2	0.6
$\chi^2_{\text{k.f.}} < 10$ Diff.	0.002	0.004			-0.044	0.003		
$\chi^2_{\text{k.f.}} < 30$ Signal	0.0	1.6	1.4	0.1	0.0	0.9	1.2	0.2
$\chi^2_{\text{k.f.}} < 30$ Diff.	-0.185	0.019			-0.068	0.011		
χ_c mass $\pm 10\,\text{MeV}$ Signal	0.0	1.7	1.5	0.2	0.1	1.0	1.2	0.6
χ_c mass $\pm 10\,\text{MeV}$ Diff.	-0.041	0.005			-0.036	0.003		
χ_c mass $\pm 20\,\text{MeV}$ Signal	0.0	1.7	1.4	0.0	0.1	1.0	1.2	0.4
χ_c mass $\pm 20\,\text{MeV}$ Diff.	-0.156	0.022			0.002	0.009		
$\lvert\cos\theta^{\text{barrel}}_{\text{lab,ph}}\rvert < 0.77$ Signal	0.1	1.7	1.5	0.2	0.1	1.0	1.2	0.3
$\lvert\cos\theta^{\text{barrel}}_{\text{lab,ph}}\rvert < 0.77$ Diff.	-0.11	0.017			-0.072	0.006		
$\lvert\cos\theta^{\text{barrel}}_{\text{lab,ph}}\rvert < 0.80$ Signal	0.1	1.7	1.4	0.3	0.1	1.0	1.2	0.5
$\lvert\cos\theta^{\text{barrel}}_{\text{lab,ph}}\rvert < 0.80$ Diff.	-0.115	0.017			-0.065	0.006		

Table C.7: Summary of uncertainties from selection criteria variations for $J_\chi = 2$ four-parameter fit performed on Monte Carlo events. We compare the statistical uncertainty, impurity bias (assigned as a systematic uncertainty) and their quadrature sum from the previous two tables.

Cuts	$\sigma^{\text{stat}}_{a_2}$ 10^{-2}	$\sigma^{\text{sys imp}}_{a_2}$ 10^{-2}	$\sigma^{\text{total quad sum}}_{a_2}$ 10^{-2}	$\sigma^{\text{stat}}_{b_2}$ 10^{-2}	$\sigma^{\text{sys imp}}_{b_2}$ 10^{-2}	$\sigma^{\text{total quad sum}}_{b_2}$ 10^{-2}
Default Cuts	1.981	0.094	1.984	1.367	0.085	1.37
$E^{\text{3rd Shwr}} < 18\,\text{MeV}$	2.066	0.052	2.067	1.421	0.107	1.425
$E^{\text{3rd Shwr}} < 50\,\text{MeV}$	1.948	0.025	1.948	1.345	0.211	1.361
$\chi^2_{\text{k.f.}} < 10$	2.048	0.018	2.048	1.407	0.035	1.408
$\chi^2_{\text{k.f.}} < 30$	1.936	0.267	1.955	1.339	0.12	1.344
χ_c mass $\pm 10\,\text{MeV}$	2.035	0.001	2.035	1.404	0.02	1.404
χ_c mass $\pm 20\,\text{MeV}$	1.964	0.061	1.965	1.355	0.167	1.365
$\lvert\cos\theta^{\text{barrel}}_{\text{lab,ph}}\rvert < 0.77$	2.043	0.1	2.046	1.407	0.07	1.408
$\lvert\cos\theta^{\text{barrel}}_{\text{lab,ph}}\rvert < 0.80$	1.957	0.107	1.96	1.353	0.081	1.356

Cuts	$\sigma^{\text{stat}}_{a_3}$ 10^{-2}	$\sigma^{\text{sys imp}}_{a_3}$ 10^{-2}	$\sigma^{\text{total quad sum}}_{a_3}$ 10^{-2}	$\sigma^{\text{stat}}_{b_3}$ 10^{-2}	$\sigma^{\text{sys imp}}_{b_3}$ 10^{-2}	$\sigma^{\text{total quad sum}}_{b_3}$ 10^{-2}
Default Cuts	1.463	0.113	1.467	1.173	0.059	1.174
$E^{\text{3rd Shwr}} < 18\,\text{MeV}$	1.524	0.106	1.528	1.221	0.027	1.221
$E^{\text{3rd Shwr}} < 50\,\text{MeV}$	1.44	0.137	1.446	1.155	0.127	1.161
$\chi^2_{\text{k.f.}} < 10$	1.508	0.002	1.508	1.207	0.044	1.208
$\chi^2_{\text{k.f.}} < 30$	1.434	0.185	1.445	1.151	0.068	1.153
χ_c mass $\pm 10\,\text{MeV}$	1.502	0.041	1.503	1.207	0.036	1.208
χ_c mass $\pm 20\,\text{MeV}$	1.449	0.156	1.458	1.161	0.002	1.161
$\lvert\cos\theta^{\text{barrel}}_{\text{lab,ph}}\rvert < 0.77$	1.504	0.11	1.508	1.2	0.072	1.202
$\lvert\cos\theta^{\text{barrel}}_{\text{lab,ph}}\rvert < 0.80$	1.449	0.115	1.453	1.164	0.065	1.166

Table C.8: Systematic uncertainties from selection criteria variations for $J_\chi = 2$ four-parameter fit performed on data. We find for all sets of selection criteria considered that there's a systematic uncertainty of $(0.4, 0.2, 0.3, 0.4) \times 10^{-2}$ for (a_2, b_2, a_3, b_3) respectively over the variation of the criteria considered.

Cuts	a_2 10^{-2}	b_2 10^{-2}	a_3 10^{-2}	b_3 10^{-2}
Default Cuts	-7.9 ± 1.9	0.2 ± 1.5	1.7 ± 1.4	-0.8 ± 1.2
$E^{\text{3rd Shwr}} < 18\,\text{MeV}$	-8.0 ± 1.9	-0.2 ± 1.5	1.6 ± 1.5	-0.7 ± 1.3
$E^{\text{3rd Shwr}} < 50\,\text{MeV}$	-7.9 ± 1.9	-0.7 ± 1.5	2.2 ± 1.3	-1.0 ± 1.2
$\chi^2_{\text{k.f.}} < 10$	-7.5 ± 1.9	0.4 ± 1.5	2.0 ± 1.4	-0.8 ± 1.2
$\chi^2_{\text{k.f.}} < 30$	-7.8 ± 1.8	-0.5 ± 1.4	2.2 ± 1.3	-0.3 ± 1.2
χ_c mass $\pm 10\,\text{MeV}$	-7.5 ± 1.9	0.1 ± 1.5	1.4 ± 1.4	-0.9 ± 1.2
χ_c mass $\pm 20\,\text{MeV}$	-7.9 ± 1.8	-0.3 ± 1.4	2.2 ± 1.4	-0.7 ± 1.2
$\lvert\cos\theta^{\text{barrel}}_{\text{lab,ph}}\rvert < 0.77$	-8.3 ± 2.0	0.4 ± 1.5	1.6 ± 1.4	-0.6 ± 1.2
$\lvert\cos\theta^{\text{barrel}}_{\text{lab,ph}}\rvert < 0.80$	-8.0 ± 1.9	0.5 ± 1.4	1.8 ± 1.4	-0.5 ± 1.2
Ensemble	-7.9 ± 0.2	0.0 ± 0.4	1.9 ± 0.2	-0.7 ± 0.2

BIBLIOGRAPHY

[1] M. Ablikim et al. Measurement of the χ_{c2} polarization in $\psi(2S) \to \gamma\chi_{c2}$. *Phys. Rev.*, D70:092004, 2004.

[2] M. Ambrogiani et al. Study of the angular distributions of the reactions $\overline{p}p \to \chi_{c1}, \chi_{c2} \to J/\psi\gamma \to e^+e^-\gamma$. *Phys. Rev.*, D65:052002, 2002.

[3] C. Amsler et al. Review of particle physics. *Phys. Lett.*, B667:1, 2008.

[4] T.A. Armstrong et al. Study of the angular distribution of the reaction $\overline{p}p \to \chi_{c2} \to J/\psi\gamma \to e^+e^-\gamma$. *Phys. Rev.*, D48:3037, 1993.

[5] M. Artuso et al. The CLEO RICH detector. *NIM*, A554:147–194, 2005.

[6] D. M. Asner et al. New measurement of exclusive decays of the χ_{c0} and χ_{c2} to two-meson final states. *Phys. Rev.*, D79:072007, 2009.

[7] C. Baglin et al. Angular distributions in the reactions $p\bar{p} \to \chi_{1,2} \to \gamma\psi \to \gamma e^+e^-$. *Physics Letters B*, 195(1):85–90, 1987.

[8] Elisabetta Barberio and Zbigniew Was. PHOTOS: A universal Monte Carlo for QED radiative corrections. version 2.0. *Comput. Phys. Commun.*, 79:291–308, 1994.

[9] N. Brambilla et al. Heavy quarkonium physics. *CERN-2005-005*, 2004.

[10] Stanley J. Brodsky and G. Peter Lepage. Helicity selection rules and tests of gluon spin in exclusive quantum-chromodynamic processes. *Phys. Rev. D*, 24(11):2848–2855, Dec 1981.

[11] Lowell S. Brown and Robert N. Cahn. Cartesian analysis of angular distributions in $e^+e^- \to \psi' \to \psi\gamma\gamma' \to \mu^+\mu^-\gamma\gamma'$. *Phys. Rev.*, D13:1195, 1976.

[12] R. Brun *et al.*, Geant 3.21, CERN Program Library Long Writeup W5013 (1993), unpublished.

[13] D.G. Cassel et al. Exclusive ρ^0, ω and ϕ electroproduction. *Phys. Rev.*, D24:2787, 1981.

[14] J Dudek, Robert Edwards, and David Richards. Radiative transitions in charmonium from lattice QCD. *Phys. Rev.*, D73:074507, 2006.

[15] Jozef Dudek, Robert Edwards, and Christopher Thomas. Exotic and excited-state radiative transitions in charmonium from lattice QCD. *Phys. Rev.*, D79:094504, 2009.

[16] B. Heltsley and H. Mahlke. $\psi(2S) \to h + J/\psi$ branching fractions. *CBX*, 019, 2008. CBX2008-019.

[17] John David Jackson. *Classical Electrodynamics*. Wiley, 3rd edition, 1998.

[18] F. James and M. Roos. Minuit: A system for function minimization and analysis of the parameter errors and correlations. *Comput. Phys. Commun.*, 10:343–367, 1975.

[19] Gabriel Karl, Sydney Meshkov, and Jonathan L. Rosner. Symmetries, angular distributions in $\psi' \to \gamma\chi \to \gamma\gamma\psi$ and the interpretation of the $\chi(3400) - \chi(3550)$ levels. *Phys. Rev.*, D13:1203, 1976.

[20] Gabriel Karl, Sydney Meshkov, and Jonathan L. Rosner. Quark magnetic moments and E1 radiative transitions in charmonium. *Phys. Rev. Lett.*, 45:215, 1980.

[21] Y. Kubota et al. The CLEO-II detector. *Nucl. Instrum. Meth.*, A320:66–113, 1992.

[22] D. J. Lange. The EvtGen particle decay simulation package. *Nucl. Instrum. Meth.*, A462:152–155, 2001.

[23] A. D. Martin, M. G. Olsson, and W. J. Stirling. Production and decay of p wave charmonium states in pp collisions. *Physics Letters B*, 147(1-3):203 – 206, 1984.

[24] Richard McClary and Nina Byers. Relativistic effects in heavy-quarkonium spectroscopy. *Phys. Rev.*, D28:1692, 1983.

[25] H. Mendez et al. Branching fractions for transitions of $\psi(2S)$ to J/ψ. *Phys. Rev.*, D78:011102, 2008.

[26] H. Muramatsu and H. Vogel. Re-counting number of ψ(2S) resonant decays. *CBX*, 07-4, 2007.

[27] M. G. Olsson, C. J. Suchyta, A. D. Martin, and W. J. Stirling. Testing the single-quark radiation hypothesis. *Phys. Rev.*, D31(7):1759–1761, Apr 1985.

[28] M. Oreglia. *A Study of the Reactions* $\psi' \to \gamma\gamma\psi$. PhD thesis, Stanford, 1980. SLAC-0236.

[29] M. Oreglia et al. A study of the reaction $\psi' \to \gamma\gamma J/\psi$. *Phys. Rev.*, D25:2259, 1982.

[30] D. Peterson et al. The CLEO III drift chamber. *Nucl. Instrum. Meth.*, A478:142–146, 2002.

[31] Jeffrey D. Richman. An experimenter's guide to the helicity formalism. 1984. CALT-68-1148.

[32] Jonathan L. Rosner. Charmless final states and S- and D-wave mixing in the ψ'' . *Phys. Rev. D*, 64(9):094002, Sep 2001.

[33] Jonathan L. Rosner. ψ'' decays to charmless final states. *Ann. Phys.*, 319:1–12, 2005.

[34] Jonathan L. Rosner. M2 signatures in $\psi(2S)$ radiative decays. *Phys. Rev.*, D78:114011, 2008.

[35] K. J. Sebastian, H. Grotch, and F. L. Ridener. Multipole amplitudes in parity-changing one-photon transitions of charmonium. *Phys. Rev.*, D45:3163, 1992.

[36] CESR-c Taskforce and CLEO-c Taskforce. CLEO-c and CESR-c: A new frontier of weak and strong interactions. *CLNS*, 01/1742, 2001.